EUROPEAN ORGANISATION FOR NUCLEAR RESEARCH

CERN-PPE/91-67
16 April 1991

Measurement of the Z^0 line shape parameters and the electroweak couplings of charged leptons.

The OPAL Collaboration

Abstract

We report on an improved measurement of the mass of the Z^0 boson, its total width and its partial decay widths into hadrons and leptons, as well as the effective axial vector and vector couplings to charged leptons. These measurements are based on a data set of approximately 166,000 hadronic Z^0 decays and 18,000 decays into electrons, muons and taus, recorded by the OPAL experiment at centre of mass energies near the mass of the Z^0.

The total width and the partial widths to visible final states, derived from the measured cross sections, are used to extract the invisible width. The effective couplings of the Z^0 to charged leptons are studied using measurements of the lepton pair cross sections and forward-backward asymmetries at the different centre of mass energy points of the Z^0 scan. The implications of our results in the context of the Standard Model are discussed.

Submitted to Z. Phys. C.

The OPAL Collaboration

G. Alexander[23], J. Allison[16], P.P. Allport[5], K.J. Anderson[9], S. Arcelli[2], J.C. Armitage[6], P. Ashton[16], A. Astbury[a], D. Axen[b], G. Azuelos[18,c], G.A. Bahan[16], J.T.M. Baines[16], A.H. Ball[17], J. Banks[16], G.J. Barker[13], R.J. Barlow[16], J.R. Batley[5], G. Beaudoin[18], A. Beck[23], J. Becker[10], T. Behnke[8], K.W. Bell[20], G. Bella[23], S. Bethke[11], O. Biebel[3], U. Binder[10], I.J. Bloodworth[1], P. Bock[11], H.M. Bosch[11], S. Bougerolle[b], B.B. Brabson[12], H. Breuker[8], R.M. Brown[20], R. Brun[8], A. Buijs[8], H.J. Burckhart[8], P. Capiluppi[2], R.K. Carnegie[6], A.A. Carter[13], J.R. Carter[5], C.Y. Chang[17], D.G. Charlton[8], J.T.M. Chrin[16], P.E.L. Clarke[25], I. Cohen[23], W.J. Collins[5], J.E. Conboy[15], M. Cooper[22], M. Couch[1], M. Coupland[14], M. Cuffiani[2], S. Dado[22], G.M. Dallavalle[2], S. De Jong[8], P. Debu[21], M.M. Deninno[2], A. Dieckmann[11], M. Dittmar[4], M.S. Dixit[7], E. Duchovni[26], G. Duckeck[11], I.P. Duerdoth[16], D.J.P. Dumas[6], G. Eckerlin[11], P.A. Elcombe[5], P.G. Estabrooks[6], E. Etzion[23], F. Fabbri[2], M. Fincke-Keeler[a], H.M. Fischer[3], D.G. Fong[17], C. Fukunaga[24], A. Gaidot[21], O. Ganel[26], J.W. Gary[11], J. Gascon[18], R.F. McGowan[16], N.I. Geddes[20], C. Geich-Gimbel[3], S.W. Gensler[9], F.X. Gentit[21], G. Giacomelli[2], V. Gibson[5], W.R. Gibson[13], J.D. Gillies[20], J. Goldberg[22], M.J. Goodrick[5], W. Gorn[4], C. Grandi[2], E. Gross[26], J. Hagemann[8], G.G. Hanson[12], M. Hansroul[8], C.K. Hargrove[7], P.F. Harrison[13], J. Hart[5], P.M. Hattersley[1], M. Hauschild[8], C.M. Hawkes[8], E. Heflin[4], R.J. Hemingway[6], R.D. Heuer[8], J.C. Hill[5], S.J. Hillier[1], D.A. Hinshaw[18], C. Ho[4], J.D. Hobbs[9], P.R. Hobson[25], D. Hochman[26], B. Holl[8], R.J. Homer[1], S.R. Hou[17], C.P. Howarth[15], R.E. Hughes-Jones[16], R. Humbert[10], P. Igo-Kemenes[11], H. Ihssen[11], D.C. Imrie[25], L. Janissen[6], A. Jawahery[17], P.W. Jeffreys[20], H. Jeremie[18], M. Jimack[2], M. Jobes[1], R.W.L. Jones[13], P. Jovanovic[1], D. Karlen[6], K. Kawagoe[24], T. Kawamoto[24], R.K. Keeler[a], R.G. Kellogg[17], B.W. Kennedy[15], C. Kleinwort[8], D.E. Klem[19], T. Kobayashi[24], T.P. Kokott[3], S. Komamiya[24], L. Köpke[8], R. Kowalewski[6], H. Kreutzmann[3], J. von Krogh[11], J. Kroll[9], M. Kuwano[24], P. Kyberd[13], G.D. Lafferty[16], F. Lamarche[18], W.J. Larson[4], J.G. Layter[4], P. Le Du[21], P. Leblanc[18], A.M. Lee[17], M.H. Lehto[15], D. Lellouch[8], P. Lennert[11], C. Leroy[18], L. Lessard[18], S. Levegrün[3], L. Levinson[26], S.L. Lloyd[13], F.K. Loebinger[16], J.M. Lorah[17], B. Lorazo[18], M.J. Losty[7], X.C. Lou[12], J. Ludwig[10], M. Mannelli[8], S. Marcellini[2], G. Maringer[3], A.J. Martin[13], J.P. Martin[18], T. Mashimo[24], P. Mättig[3], U. Maur[3], T.J. McMahon[1], J.R. McNutt[25], F. Meijers[8], D. Menszner[11], F.S. Merritt[9], H. Mes[7], A. Michelini[8], R.P. Middleton[20], G. Mikenberg[26], J. Mildenberger[6], D.J. Miller[15], C. Milstene[23], R. Mir[12], W. Mohr[10], C. Moisan[18], A. Montanari[2], T. Mori[24], M.W. Moss[16], T. Mouthuy[12], P.G. Murphy[16], B. Nellen[3], H.H. Nguyen[9], M. Nozaki[24], S.W. O'Neale[8,d], B.P. O'Neill[4], F.G. Oakham[7], F. Odorici[2], M. Ogg[6], H.O. Ogren[12], H. Oh[4], C.J. Oram[e], M.J. Oreglia[9], S. Orito[24], J.P. Pansart[21], B. Panzer-Steindel[8], P. Paschievici[26], G.N. Patrick[20], S.J. Pawley[16], P. Pfister[10], J.E. Pilcher[9], J.L. Pinfold[26], D.E. Plane[8], P. Poffenberger[a], B. Poli[2], A. Pouladdej[6], E. Prebys[8], T.W. Pritchard[13], H. Przysiezniak[18], G. Quast[8], M.W. Redmond[9], D.L. Rees[1], K. Riles[4], S.A. Robins[13], D. Robinson[8], A. Rollnik[3], J.M. Roney[9], S. Rossberg[10], A.M. Rossi[2,f], P. Routenburg[6], K. Runge[10], O. Runolfsson[8], D.R. Rust[12], S. Sanghera[6], M. Sasaki[24], A.D. Schaile[10], O. Schaile[10], W. Schappert[6], P. Scharff-Hansen[8], P. Schenk[a], H. von der Schmitt[11], S. Schreiber[3], J. Schwarz[10], W.G. Scott[20], M. Settles[12], B.C. Shen[4], P. Sherwood[15], R. Shypit[b], A. Simon[3], P. Singh[13], G.P. Siroli[2], A. Skuja[17], A.M. Smith[8], T.J. Smith[8], G.A. Snow[17], R. Sobie[g], R.W. Springer[17], M. Sproston[20], K. Stephens[16], H.E. Stier[10], D. Strom[9], H. Takeda[24], T. Takeshita[24], P. Taras[18], S. Tarem[26], P. Teixeira-Dias[11], N.J. Thackray[1], T. Tsukamoto[24], M.F. Turner[5], G. Tysarczyk-Niemeyer[11], D. Van den plas[18], R. Van Kooten[8], G.J. VanDalen[4], G. Vasseur[21], C.J. Virtue[19], A. Wagner[11], C. Wahl[10], J.P. Walker[1], C.P. Ward[5], D.R. Ward[5], P.M. Watkins[1], A.T. Watson[1], N.K. Watson[8], M. Weber[11], S. Weisz[8], P.S. Wells[8], N. Wermes[11], M. Weymann[8], M.A. Whalley[1], G.W. Wilson[21], J.A. Wilson[1], I. Wingerter[8], V-H. Winterer[10], N.C. Wood[16], S. Wotton[8], T.R. Wyatt[16], R. Yaari[26], Y. Yang[4,h], G. Yekutieli[26], I. Zacharov[8], W. Zeuner[8], G.T. Zorn[17].

[1]School of Physics and Space Research, University of Birmingham, Birmingham, B15 2TT, UK
[2]Dipartimento di Fisica dell' Università di Bologna and INFN, Bologna, 40126, Italy
[3]Physikalisches Institut, Universität Bonn, D-5300 Bonn 1, FRG
[4]Department of Physics, University of California, Riverside, CA 92521 USA
[5]Cavendish Laboratory, Cambridge, CB3 0HE, UK
[6]Carleton University, Dept of Physics, Colonel By Drive, Ottawa, Ontario K1S 5B6, Canada
[7]Centre for Research in Particle Physics, Carleton University, Ottawa, Ontario K1S 5B6, Canada
[8]CERN, European Organisation for Particle Physics, 1211 Geneva 23, Switzerland
[9]Enrico Fermi Institute and Department of Physics, University of Chicago, Chicago Illinois 60637, USA
[10]Fakultät für Physik, Albert Ludwigs Universität, D-7800 Freiburg, FRG
[11]Physikalisches Institut, Universität Heidelberg, Heidelberg, FRG
[12]Indiana University, Dept of Physics, Swain Hall West 117, Bloomington, Indiana 47405, USA
[13]Queen Mary and Westfield College, University of London, London, E1 4NS, UK
[14]Birkbeck College, London, WC1E 7HV, UK
[15]University College London, London, WC1E 6BT, UK
[16]Department of Physics, Schuster Laboratory, The University, Manchester, M13 9PL, UK
[17]Department of Physics and Astronomy, University of Maryland, College Park, Maryland 20742, USA
[18]Laboratoire de Physique Nucléaire, Université de Montréal, Montréal, Quebec, H3C 3J7, Canada
[19]National Research Council of Canada, Herzberg Institute of Astrophysics, Ottawa, Ontario K1A 0R6, Canada
[20]Rutherford Appleton Laboratory, Chilton, Didcot, Oxfordshire, OX11 0QX, UK
[21]DPhPE, CEN Saclay, F-91191 Gif-sur-Yvette, France
[22]Department of Physics, Technion-Israel Institute of Technology, Haifa 32000, Israel
[23]Department of Physics and Astronomy, Tel Aviv University, Tel Aviv 69978, Israel
[24]International Centre for Elementary Particle Physics and Dept of Physics, University of Tokyo, Tokyo 113, and Kobe University, Kobe 657, Japan
[25]Brunel University, Uxbridge, Middlesex, UB8 3PH UK
[26]Nuclear Physics Department, Weizmann Institute of Science, Rehovot, 76100, Israel
[§]University of British Columbia, Dept of Physics, 6224 Agriculture Road, Vancouver BC V6T 2A6, Canada
[§§]University of Victoria, Dept of Physics, P O Box 1700, Victoria BC V8W 2Y2, Canada

[a]Univ of Victoria, Victoria, Canada
[b]Univ of British Columbia, Vancouver, Canada
[c]and TRIUMF, Vancouver, Canada
[d]On leave from Birmingham University
[e]Univ of Victoria, and TRIUMF, Canada
[f]Present address: Dipartimento di Fisica, Università della Calabria and INFN, 87036 Rende, Italy
[g]Univ of British Columbia and IPP, Canada
[h]On leave from Research Institute for Computer Peripherals, Hangzhou, China

1 Introduction

After the first year of operation of the electron-positron collider LEP, experimental tests of the Standard Model and thereby of the unification of the weak and electromagnetic interactions have reached a new level of accuracy. The mass of the Z^0 boson, the massive neutral carrier of the electroweak field, is a fundamental parameter. Within the framework of the Standard Model, the precise determination of M_Z, in conjunction with the knowledge of the fine structure constant, α, and the Fermi coupling constant, G_F, leads to well defined predictions for the couplings of the Z^0 to all fermions. The predicted couplings are affected by the unknown masses of the top quark, M_t, and of the Higgs, M_H. Both the mass of the Z^0 and its couplings to fermions are measured to high precision at LEP: comparison of these measurements with the predictions of the Standard Model provide a stringent test of the model and place bounds on the allowed ranges of M_t and M_H.

Here we present measurements performed with the OPAL detector of the mass of the Z^0 boson, M_Z, its total width, Γ_Z, and partial decay widths into hadrons, charged leptons and invisible final states. The axial vector and vector couplings of the Z^0 to charged leptons are extracted from measurements of the leptonic partial widths and forward-backward asymmetries.

In previous publications [1,2] we presented a similar set of measurements using the data sample collected in 1989. The data added in 1990 correspond to an approximately five-fold increase in statistics with respect to the 1989 data set. The analysis presented here is based on a total of approximately 165,700 hadronic and 18,300 leptonic Z^0 decays. The cross sections and forward-backward asymmetries were measured at seven centre of mass energies, spanning an interval of approximately ± 3 GeV about the peak of the Z^0 resonance.

Compared with the previous measurements, several improvements were made in the analysis of the 1990 data set. The luminosity measurement underwent considerable evolution and as a result the systematic uncertainties on the absolute and point-to-point normalisation were much reduced. The hadronic event selection for the 1990 data included charged track information, so that the efficiency was increased, while the backgrounds were reduced with respect to the earlier analysis. For the e^+e^- channel, in order to facilitate the extraction of electroweak parameters from the data, an acceptance symmetric in $\cos\theta$ was defined, with somewhat different kinematic criteria than those used in [2]. For $\mu^+\mu^-$ and $\tau^+\tau^-$ events the geometrical acceptance was extended, and for $\tau^+\tau^-$ events the selection efficiency within the geometrical acceptance was increased. With the increased statistics available the understanding of systematic effects improved for all the event selections, resulting in significantly reduced systematic uncertainties on the calculated acceptances.

A description of the OPAL detector is given in section 2. The luminosity measurement and the hadronic and leptonic event selections are described in sections 3, 4 and 5 respectively. Section 6 discusses the treatment and analysis of the measured cross sections and forward-backward asymmetries. Finally, the results are summarised in section 7.

2 The OPAL detector

The OPAL detector is described in detail elsewhere [3]. Here we briefly mention those aspects of the detector which were relevant to this analysis. For the following we define a coordinate system where the z axis follows the electron beam direction, r is in the plane perpendicular to the z axis and θ and ϕ are the polar and azimuthal angles with respect to the z axis.

The measurements of the trajectories and momenta of charged particles were performed with a precision vertex chamber, a jet chamber and z-chambers. The vertex chamber is divided into 36 sectors with 12 axial and 6 stereo wires each. The jet chamber is a large volume drift chamber divided into 24 azimuthal sectors, each sense wire plane having 159 wires. Each of the wires provided true three-dimensional coordinates, from the wire position and from a drift-time measurement in the r-ϕ plane and from a charge-division measurement in the z direction. In the barrel region, the jet chamber is surrounded by a set of z-chambers, designed to provide an accurate z coordinate measurement where the tracks leave the jet chamber. The chambers are positioned inside a pressure vessel, surrounded by a solenoidal coil which provides a magnetic field of 0.435 Tesla. The pressure vessel and the coil have an effective thickness of about $2\,X_0/\sin\theta$ in the region of $|\cos\theta| < 0.7$, where X_0 is one radiation length. The coil is in turn surrounded by a barrel time-of-flight counter array consisting of 160 scintillator bars with photo-tube readout at both ends. A lead glass electromagnetic calorimeter with a presampler, corresponding to 24.6 radiation lengths and about two hadronic interaction lengths, measures the positions and energies of showering particles. The magnet return yoke serves as a hadron calorimeter and was instrumented with 9 layers of streamer tubes, read out via charge induction onto pads and onto 4 mm wide aluminium strips. The hadron calorimeter also aids in muon identification. The detector is surrounded by four layers of drift chambers for the detection of muons emerging from the hadron calorimeter. At both ends, end cap detectors provide similar calorimetry over nearly the full remaining solid angle. Four layers of muon chambers, consisting of streamer tubes, give good solid angle coverage of the end caps.

At the time of this analysis, the momentum resolution of the tracking detectors was $\Delta p/p \approx 10\%$, for $p \approx 45$ GeV. The electromagnetic energy resolution was typically $\Delta E/E \approx 3\%$ for $E \approx 45$ GeV, except in the region $0.73 < |\cos\theta| < 0.83$, where additional material in front of the calorimeter degraded the energy resolution. The end cap muon chambers provided a precise coordinate measurement for muons, which was used to define the acceptance with a resolution of better than 1 mrad.

The primary event selection was performed by the trigger system [4], which initiated the readout of data from the detector if sufficient activity occurred. The vertex chamber and the jet chamber, which together formed the "track trigger", the time-of-flight detector, the electromagnetic barrel and endcap calorimeters and the barrel and endcap muon chambers each provided independent trigger signals, where the electromagnetic calorimeter triggers with the lowest threshold were sensitive to particles depositing more than about 1 GeV, and the other triggers were sensitive also to minimum ionising charged particles. Therefore visible decays of a Z^0 into a fermion pair gave rise to at least 6 independent trigger signals in the barrel region and at least 4 in the endcap region. Typically two such signals per event were required in order to accept an event at the trigger level. In addition, events were accepted if the energy deposited in the electromagnetic calorimeter exceeded a threshold of approximately 7 GeV. This high redundancy allowed the efficiencies of individual triggers to be accurately measured from the data and led to a high overall efficiency of greater than 99.9% for each visible decay mode of the Z^0, within the acceptance of the analysis cuts. Small-angle Bhabha events were selected with an efficiency greater than 99.9% by triggers based on the total energy deposited in the forward detector calorimeter. On-line data reduction was achieved by a filter program which rejected cosmic ray and machine related backgrounds as well as events triggered by detector noise, based on a partial event reconstruction. The filter was found to have a negligible inefficiency for the analyses presented here.

For Monte Carlo studies the OPAL detector was simulated using a program [5] that treated in detail the detector geometry and material as well as effects of detector resolutions and efficiencies.

3 The luminosity measurement

The luminosity of the colliding beams was determined by the observation of small-angle Bhabha scattering events using two identical forward detectors mounted at each side of the interaction point [3]. Their acceptance covered angles from 40 to 150 mrad from the beam line and 2π in azimuth.

A schematic illustration of the forward detectors is shown in Figure 1. Four elements of each forward detector play a central role in this analysis. A lead-scintillator sandwich calorimeter accurately measures energy deposition ($\frac{\Delta E}{E} = 18\%/\sqrt{(E)}$ for E in GeV). The calorimeter also measures shower position by virtue of azimuthal segmentation and separate inner and outer edge readouts, and gives shower development information through longitudinal segmentation into presampler and main sections. Each forward detector also contains a set of proportional tube chambers [6]. Situated after the four radiation lengths of the presampler section of the calorimeter, the tube chambers provide measurements of the shower position in θ and ϕ. Two planes of drift chambers [7] are upstream of each forward calorimeter (i.e. closer to the interaction point). Drift chamber tracks from electrons which did not shower in the beam pipe or other upstream material were used to survey the position of the tube chambers. Also upstream of the calorimeters are precisely machined scintillators (the fine luminosity scintillators). In each quadrant in ϕ there is an acceptance defining "A" counter, which is a trapezium with an area of 92 cm^2. The inner edge of the "A" counters is at approximately 52 mrad from the beam line. Downstream of each "A" counter is a coincidence or "C" counter, which is 1 cm larger on all sides.

The analysis was carried out in three parts: an absolute luminosity determination using the forward proportional tube chambers, drift chambers, and calorimeters (method I); a second absolute luminosity calculation using the fine luminosity scintillators and calorimeters (method II); and a stable, high-statistics, relative luminosity counter using the calorimeters alone. Variants of method I and the relative luminosity counter analysis were used for the 1989 data; method II was completely new. The two absolute measures of the luminosity were largely independent and were therefore combined to provide a more accurate measurement. The main uncertainty common to the two methods stemmed from the theoretical calculation of the Bhabha cross section; this was taken as completely correlated in the error calculation.

For method I, tube chamber and calorimeter position information was used to select events in a well-defined acceptance region, and an energy cut was made to eliminate the off-momentum beam particle background. In order to reject spurious clusters, only the largest energy calorimeter cluster at each end and the tube chamber cluster nearest to it in ϕ were considered. The difference in ϕ between the tube chamber and calorimeter clusters was required to be less than 6°. The tube chamber clusters selected according to this procedure were used to define the coordinates of the event. When no tube chamber cluster satisfied this association, the calorimeter coordinate information was used. The calorimeter coordinates were also used in fiducial regions outside the main acceptance defining cuts where the tube chambers were known to be inaccurate ($\theta_{\text{calorimeter}}$ <53 mrad). No significant bias was introduced by the 5% of cluster coordinates which came from the calorimeter; when we repeated the method I analysis using only calorimeter information, the luminosity changed by less than 2%.

To eliminate any first-order dependence of the acceptance on a displacement of the interaction point with respect to the detectors, the essential cuts were made on the average of angles measured at the two ends, $\overline{\theta} = (\theta_L + \theta_R)/2$ and $\overline{\phi} = (\phi_L + \phi_R + 180°)/2$ (where θ_L and θ_R are the scattering angles of the positron and electron respectively, and ϕ is always reduced to the interval 0 to 360°).

The acceptance cuts were:

- 58 mrad $< \overline{\theta} <$ 110 mrad;
- $\overline{\phi} > 10°$ away from the vertical and horizontal axes;
- 48 mrad $< \theta_{L,R} <$ 120 mrad;
- acoplanarity ($|\Delta\phi - 180°|$) $< 20°$, where $\Delta\phi = |\phi_L - \phi_R|$.

The angular regions defined by these cuts excluded the beam pipe support web, ensuring that the final state particles in accepted events traversed less than $0.4X_0$ before entering the forward detectors. The cuts imposed on the polar angle at each end were 10 mrad outside the cut on the average polar angle, allowing sufficient tolerance to avoid significant first-order sensitivity to the beam position, while requiring even the particles in radiative events to lie within a well understood region of the detector. There was a small contamination from off-momentum beam particles which survived these cuts (<3%; see Figure 2). This was eliminated by requiring that the sum of the left and right cluster energy be greater than two thirds of the centre of mass energy:

- $E_L + E_R \geq 2/3 \cdot \sqrt{s}$

The remaining events observed within the accepted sample with low energy in both forward detectors (see Figure 2) were consistent in energy distribution and other kinematic variables with the radiation of two hard initial state photons. The cut on acoplanarity excluded only 0.6% of events passing all other cuts, and could have been dropped entirely without introducing significant additional backgrounds (see Figure 4).

Studies of events taken with a trigger demanding electron-positron coincidences delayed by one turn of the bunches in LEP confirmed that less than 1.0×10^{-5} of the events selected by method I were due to accidental backgrounds. The calculated contamination of $e^+e^- \rightarrow \gamma\gamma$ events was 0.15%, and was subtracted. Other physics backgrounds were shown to represent less than 6×10^{-4} of the accepted events.

The final sample of selected events was compared with events generated using the BABAMC $O(\alpha)$ Monte Carlo program [8] and gaussian smearing to model the detector response. The data and Monte Carlo showed only subtle deviations in the important kinematic variables, which we attribute to the omission of higher order terms in BABAMC. (see Figures 3, 4 and 5). The acceptance for events selected by method I was determined to be 21.9 nb at $\sqrt{s}$=91.1 GeV, including the corrections to the $O(\alpha)$ calculation which are discussed below. The energy dependence of the accepted BABAMC cross section, including the term due to $Z^0\gamma$ interference, displayed a maximum change of 1% with respect to the simple $1/s$ dependence expected from quantum electro-dynamics.

Two aspects of the forward detector geometry had irreducible importance in determining the absolute acceptance: the distance between the two forward detectors and the absolute scale of the radii they measured. We measured the distance between the detectors directly to a precision of 0.5 mm, resulting in a 0.1% uncertainty in the luminosity. The average radial position of the tube chambers (with respect to the beam axis) was crucial in determining the acceptance for method I. The mechanical survey of the tube chambers presented a significant source of systematic uncertainty in our previous measurements [1,2]. We were able to overcome these limitations by using single electron tracks reconstructed in the drift chambers, thus referencing the tube chamber coordinate system to the accurate mechanical survey of the drift chambers. To achieve the required level of precision, we used a method for comparing drift chamber and tube chamber coordinates which

relied only on the linearity of the relation between drift time and distance from the drift chamber wires.

The absolute radial positions of the tube chambers were determined by comparing the hit times of clean electron tracks in the second plane of drift chambers with the coordinates of showers reconstructed by the tube chambers. Each plane of drift chambers is azimuthally subdivided into 4 modules, one per quadrant. A schematic drawing is shown in the insert of Figure 6. The main part of Figure 6 shows the drift time for Bhabha electrons as measured in one drift chamber, as a function of the corresponding tube chamber coordinate. Most hits lie close to the longer of two straight bands, corresponding to the large number of Bhabha events at scattering angles smaller than the corresponding sense wire position (which is at approximately 100 mrad). Hits in the drift chamber at angles larger than the sense wire position lie close to the shorter straight band. The drift chambers had an intrinsic resolution of better than 300 μm. The scatter of points is due to the ± 2 mm resolution on the shower centroids measured by the tube chambers. The lines are a fit to the data, assuming that the drift speed is constant and the same above and below the sense wires. The intersection of the lines gives the position of the image of the drift chamber sense wires in the tube chamber coordinate system. This was compared with the surveyed values for the drift chamber position and was used to determine the tube chamber position. The separation of the wires in each pair of diametrically opposite drift chambers was measured with a precision of 93 μm, of which 45 μm was correlated between the four such pairs. The resulting uncertainty in the average radial wire position was 30 μm. The average tube chamber radius was determined with an accuracy of 135 μm, corresponding to a systematic uncertainty of 0.3% on the luminosity, where the error is largely the statistical error of the fit.

Since the determination of the tube chamber position by the drift chambers was made at approximately 100 mrad, while the important inner edge cut was at 58 mrad, an uncertainty in the precise pitch of the tubes led to a further 0.4% systematic uncertainty in the luminosity. The coordinates of the tube chambers at the inner edge were checked by examining the reconstructed positions of tracks in events which were selected by means of the fine luminosity scintillation counters (see method II below). The image of the A counters in the tube chambers is clearly visible in Figure 7, and agreed with the drift chamber survey, albeit with a limited systematic accuracy of 300 μm.

Possible detector reconstruction inefficiencies and local distortions due to tube chamber gain variations were studied extensively. Inefficiencies were found to be negligible (<0.1%). Evidence of inhomogeneity in tube chamber reconstruction was found and led to the assignment of a 0.5% systematic uncertainty. One method used to quantify this effect was to examine the variation of the luminosities measured in different portions of the acceptance. We divided the acceptance in ϕ into sixteen identical telescopes, of which opposite pairs were summed to cancel the azimuthal modulation of the acceptance due to any inclination of the beam with respect to the detector axis. The r.m.s. variation in the eight resulting measurements was 1.5%, well beyond the 0.5 ± 0.3% expected from statistics. Since systematic errors due to tube chamber inhomogeneities varied independently for the eight measurements, the resulting variation in the overall luminosity was expected to be only $1.5\%/\sqrt{8}$ or 0.5%. Several other studies corroborated this result.

The contributions to the experimental systematic error in method I are listed in Table 1. Of the total 0.8% experimental error in the luminosity determined by method I, 0.3% was due to the finite statistics of the Bhabha sample.

A second, experimentally independent luminosity calculation was made using the fine luminosity scintillation counters (method II). The scintillators were arranged in four independent back-to-back

telescopes, each consisting of two A-C scintillator pairs. The basic geometrical selection for Bhabha events required hits in one of the A counters and the two C counters in a telescope. By summing the events from all four quadrants and averaging over the luminosities found when the A counter requirement was imposed separately at each end, the sensitivity of method II to first order effects in the position of the beam interaction point relative to the counters was removed. The energy deposited in the calorimeter quadrants associated to an ACC coincidence was required to be greater than 72% of the centre of mass energy to remove background. Additional cuts on the longitudinal development of the showers in the forward calorimeters reduced the effect of spurious coincidences due to showering in the beam pipe support web.

The accepted cross section for method II was determined to be 8.2 nb at $\sqrt{s}$=91.1 GeV by means of a simple Monte Carlo detector simulation based on events generated using BABAMC. Two corrections to the calculated cross section based on the results of a full showering Monte Carlo and studies of the data were made to account for effects ignored in the simple detector simulation. The first considered scintillators hit by particles accompanying Bhabha electrons, the second considered scintillators hit by the Bhabha electrons themselves but only because they were scattered by the beampipe. Corrections of $1.6 \pm 0.9\%$ and $1.9 \pm 1.0\%$ were made to account for these effects. The effective broadening of the electrons due to scattering in the beam pipe is apparent as the low angle tail in Figure 7. Small uncertainties in the simulation, such as the effect of the finite scintillator thickness, resulted in a 0.5% error. Imperfect simulation of hard radiative events led to a potential overestimate of the acceptance. Studies showed this effect to be less than 0.3%. The position of each of the scintillators was surveyed to an accuracy of 300 μm, leading to a 0.2% uncertainty in the acceptance. The resulting total experimental error was 1.5%, to which finite event statistics contributed 0.4%. The complete list of correction factors and uncertainties is given in Table 2.

The integrated luminosities determined by methods I and II for the sample of 1990 data used to determine the multihadronic cross section were 6.58 ± 0.05 pb^{-1} and 6.68 ± 0.10 pb^{-1} respectively. The final luminosity value was taken as the average of both measurements, weighted according to their experimental errors. This resulted in an overall experimental uncertainty in the final luminosity determination, including statistics, of 0.7%.

Recent theoretical work [9,10] has led to a better understanding of the accuracy of $O(\alpha)$ calculations and of higher order corrections, including the effect of direct light fermion pair production (resulting in four-fermion final states). In calculating our experimental acceptances we followed the method outlined in reference [10]. We first validated the numerical accuracy of BABAMC within our acceptance by generating events without vacuum polarisation or s-channel and interference contributions, and compared its results with the exact $O(\alpha)$ analytic calculation of reference [9]. We find agreement to within 0.1% when K_0, the photon cut-off parameter, is 0.001. We then re-enabled the s-channel and interference contributions and included leptonic loop diagrams and the parametrisation of hadronic vacuum polarisation of reference [11], and generated events to determine the $O(\alpha)$ experimental acceptance. We did not modify the structure of BABAMC to include the effect of loop diagrams in radiative events. Leptonic loops changed the reference t-channel cross section by +3.73% and quark loops by $+2.1 \pm 0.1\%$. We then used the LUMLOG program [10] to calculate higher order QED corrections in the leading log approximation. These represented -0.10% for method I and +0.15% for method II. The magnitude and sign of the higher order corrections are sensitive to the detailed definition of the experimental acceptance. Cuts which constrain the geometry of radiative events tend to result in large negative $O(\alpha)$ corrections, which are then partially offset by positive corrections in higher order. An independent higher order calculation [12], which required $3^\circ \leq \theta(e^\pm) \leq 8^\circ$ and $E_{e^\pm} \geq 0.5 E_{\mathrm{beam}}$ resulted in a higher order correction of $(+0.4 \pm 0.5)\%$. The LUMLOG program, within the same acceptance cuts, obtained

in a correction of $(+0.3 \pm 0.2)\%$, in better agreement than the errors would suggest.

The theoretical uncertainty resulting from the procedure adopted was as follows: 0.3% total QED uncertainty [10], 0.2% from the exclusion of hadronic loops in hard radiative events, and 0.1% from uncertainty in the parametrisation of hadronic vacuum polarisation [11]. We therefore assigned a 0.4% total theoretical uncertainty to the absolute luminosity calculation, which we assumed to be completely correlated between methods I and II. The resulting total absolute luminosity uncertainty was then 0.8%.

A simple calorimeter-based luminosity counter which offered a considerably larger acceptance to Bhabha events was used in calculating all physics cross sections described in this paper. The requirements of the counter were that it be stable with time and beam energy, and be background free. The only two selection cuts imposed were that the total cluster energy in the main calorimeters be greater than 70% of the centre of mass energy, and that the acoplanarity angle be less than 20°. Selected events contained only a small fraction of background (4.0×10^{-5}). Careful calibration of the energy scale of the forward calorimeters reduced the uncertainty in measured shower energy for each LEP fill to less than 0.5%. This corresponded to a fill to fill uncertainty in the luminosity measurement of 0.8%; the energy point to energy point luminosity uncertainty resulting from this instability of the calorimeter calibration was therefore $0.8\%/\sqrt{N_{fills}}$, where N_{fills} is the number of fills contributing to the measurement at a given energy point. This uncertainty was always smaller than the statistical error.

The relative and absolute scales of the counter's acceptance were established in three steps. The BABAMC program [8] was used to determine the energy dependence of the Bhabha cross section within the counter's acceptance. Interference caused a maximum deviation of 0.8% with respect to a simple $1/s$ dependence. At each energy point the statistical accuracy of the Monte Carlo calculation was 0.1%. Since the effective width of the Z^0 resonance in BABAMC differed by 150 MeV from the measured value, we assigned 25% of the calculated interference effect at each energy point as a systematic error. The total uncertainty on the $Z^0\gamma$ interference was added in quadrature to the uncertainty resulting from the calorimeter instability to give the final energy point to energy point systematic error in the luminosity.

The counter luminosity was then compared with that of methods I and II as a function of time and beam energy; no statistically significant deviations were observed. Finally the absolute acceptance of the calorimeter counter was determined by requiring the counter luminosity to agree with the luminosity determined by methods I and II for the entire 1990 data sample. It was found to be 43.6 nb at $\sqrt{s}$=91.1 GeV. By determining the counter's Bhabha acceptance from methods I and II, we avoided the difficulty of accurately simulating electron showers in a complicated geometry, while obtaining high statistics luminosity measurements at each centre of mass energy point.

4 The Hadronic Decays

The criteria used to select hadronic Z^0 decays were based on energy clusters in the electromagnetic calorimeter and the charged track multiplicity. Clusters in the barrel region were required to have an energy of at least 100 MeV, and clusters in the end cap detectors were required to contain at least two adjacent lead glass blocks and have an energy of at least 200 MeV. Tracks were required to have at least 20 measured space points and a distance of closest approach to the interaction point of less than 2 cm in the direction perpendicular to the beam axis and less than 40 cm along the beam axis. Tracks were also required to have a minimum momentum component transverse to

the beam direction of 50 MeV.

The following four requirements defined a multihadron candidate:

- at least 7 clusters
- at least 5 tracks
- a total energy deposited in the lead glass of at least 10% of the centre-of-mass energy:

$$R_{vis} \equiv \Sigma E_{clus}/\sqrt{s} > 0.1,$$

  where E_{clus} is the energy of each cluster
- an energy imbalance along the beam direction which satisfied

$$R_{bal} \equiv \mid \Sigma(E_{clus} \cdot \cos\theta) \mid / \Sigma E_{clus} < 0.65.$$

where θ is the polar angle of the cluster. For the modelling of hadronic decays we used the JETSET 7.2 [13] parton shower model event generator, with five flavours and string fragmentation. The model was used with a set of optimised parameters determined from a study of global event shape variables performed by OPAL [14]. The events generated were then processed by the detector simulation Monte Carlo program [5].

The measured distributions of the variables used in the selection are shown in Figure 8 for the Monte Carlo simulation and the real data (at the Z^0 peak), in each case after all cuts except that on the distribution shown have been applied. The differences between data and Monte Carlo are discussed below. Figure 9 shows the distribution of the cosine of the polar angle of the thrust axis of selected multihadronic events, $|\cos\theta_{Thrust}|$, for data and Monte Carlo. The data are well reproduced by the Monte Carlo in the critical region of $|\cos\theta| > 0.9$.

The cut on the number of clusters and the number of tracks efficiently eliminated Z^0 decays into charged lepton pairs. The vertex requirements on tracks served to eliminate events caused by cosmic rays. The R_{vis} cut discarded two-photon and beam-gas events. The cut in R_{bal} rejected beam-wall, beam-gas and beam-halo events, as well as cosmic rays in the end caps.

Alternative selection criteria which used only charged tracks, as well as the selection criteria based on the electromagnetic calorimeter and the time-of-flight counters, as described in the previous publications [15,1], were used to check the selection described above. The numbers of events and the overlap of the selected samples were checked for these different selections and no significant fill-to-fill variations were observed. The relative cross sections as functions of energy were compared and were found to be identical at the level of 0.3%. The absolute peak cross section for the selection described here also agreed to better than 0.1% with that obtained using the selection decribed in [15,1].

The main contamination in the hadronic data sample came from $\tau^+\tau^-$ events and two-photon multihadronic events. For $\tau^+\tau^-$ events, a background fraction of $0.11 \pm 0.03\%$ was estimated by using Monte Carlo events generated with the KORALZ program [16]. The background from two-photon processes was estimated from the data by measuring the ratio of the numbers of events with high and low R_{vis} and the ratio of the numbers of events with high and low R_{bal} as functions of the beam energy. This resulted in a background estimate of 0.02 ± 0.01 nb, corresponding to approximately 0.5% of the resonant cross section at the extreme energy points of the scan. This estimate also accounted for other non-resonant background sources with a small energy deposit

and a large energy imbalance, such as beam-related background. Possible beam-wall and beam-gas interaction events were investigated by changing the vertex requirements on tracks and were found to be negligible. Any remaining cosmic ray background and the background contribution from $e^+e^- \to e^+e^-$ and $e^+e^- \to \mu^+\mu^-$ to the hadronic event sample were also estimated to be negligible.

The acceptance of the event selection procedure was determined to be 98.4%, with a negligible statistical error, for the Monte Carlo sample of simulated multihadronic events. Various checks were made to estimate the uncertainties in the acceptance calculation, which might arise from shortcomings of the detector simulation as well as in the modelling of fragmentation in hadronic Z^0 decays.

The distribution of the energy deposited in the electromagnetic calorimeter showed a clear systematic shift in scale between data and Monte Carlo, of approximately 6%, and both the cluster and track multiplicity distributions showed an offset of the Monte Carlo with respect to the data of approximately 0.5 to 1 unit in multiplicity (see Figure 8). Possible errors in the acceptance calculation resulting from these discrepancies were estimated by calculating the acceptance after rescaling the electromagnetic energy response in the Monte Carlo by 6%, and after offsetting each of the Monte Carlo cluster and charged multiplicities by 0.5 and 1 units respectively. This study resulted in an estimated uncertainty of 0.2% on the hadronic acceptance calculation, which was attributed to possible shortcomings in the detector simulation.

The effect of uncertainties resulting from modelling of hadronisation was investigated in two ways. We compared the acceptance calculated using the JETSET model with that obtained with the HERWIG model [17], with a set of optimised parameters determined by OPAL [14] (HERWIG versions 4.6 and 5.0). We observed a difference of $0.23 \pm 0.07\%$. We also repeated the acceptance calculation with the JETSET model varying the optimised parameters of the model by one standard deviation (see [14] for details). The parameter Q_0, the invariant mass cut-off for parton showers, was varied in the interval $0.7 < Q_0 < 1.8$; Λ_{QCD} was varied in the interval $0.28 < \Lambda_{QCD} < 0.31$; the width of the transverse momentum distribution of primary hadrons, σ_q, was varied within $0.32 < \sigma_q < 0.40$ and the fragmentation parameter a was varied within $0.13 < a < 0.30$. We also varied the parameter $\Delta(s/u)$, the suppression of strange quark pair production in the colour field with respect to up or down quark pairs, within the range $0.24 < \Delta(s/u) < 0.36$. The largest change in the acceptance ($0.2 \pm 0.1\%$) resulted from the variation of Q_0. The sum in quadrature of the deviations observed in this study and of the difference between the JETSET and HERWIG hadronisation models was 0.3%. This was added in quadrature with the uncertainty of 0.2% attributed to the detector simulation, and resulted in a total systematic uncertainty on the hadronic acceptance of 0.4% at the peak.

The energy dependence of the acceptance in the region of the scan was evaluated as $0.2 \pm 0.2\%$ for the points at ± 3 GeV from the peak, where the error was due to the lower statistics of the Monte Carlo events available at these energies. No energy dependent correction to the acceptance was applied, but an energy point to energy point uncertainty of $0.2\% \cdot |\Delta E|/(3\ \mathrm{GeV})$ was assigned, where ΔE is the difference in energy, in GeV, with respect to the point at the peak of the Z^0 resonance. The correction factors and systematic uncertainties in the multihadron selection are summarised in Table 3; they result in an overall correction factor of 1.014 ± 0.004 at the peak of the Z^0 resonance. The multihadron cross section results are given in Table 7.

5 The Leptonic Decays

The cross sections and the forward-backward asymmetries were obtained for each charged leptonic final state at the seven centre of mass energy points of the scan. The criteria used to select $e^+e^- \to e^+e^-$, $e^+e^- \to \mu^+\mu^-$ and $e^+e^- \to \tau^+\tau^-$ events were similar to those used for the analysis of our 1989 data sample [2]. In the present analysis, however, the acceptance for the $e^+e^- \to e^+e^-$ channel has been defined by $|\cos\theta_{e^-}| < 0.7$, which refers only to the electron direction, and no attempt is made to exclude events with non-colinear radiation. The angular region of acceptance has been extended to $|\cos\theta| < 0.90$ for $\tau^+\tau^-$ and $|\cos\theta| < 0.95$ for $\mu^+\mu^-$ and the systematic errors have been reduced substantially. For each reaction, the cross section was determined from the subset of the total data sample for which a reliable luminosity and efficiency could be evaluated. For the asymmetry measurements these restrictions were relaxed, in order to reduce the statistical errors, but a reliable charge determination was required. Quality cuts similar to those used in the hadronic event selection were also applied in the lepton analyses to eliminate noisy calorimeter hits and to define a well understood set of tracks. None of the analyses was sensitive to the details of these cuts.

In order to study efficiencies and backgrounds in the following analyses, use was made of Monte Carlo generated events which had been processed by the detector simulation program [5]. Unless otherwise stated, multihadronic events were generated using the JETSET program (version 7.2) as described above. The HERWIG program (version 4.3) [17,14] was also used for some systematic checks. The program BABAMC [8] was used to generate $e^+e^- \to e^+e^-$ events and KORALZ (version 3.7) [16] for $e^+e^- \to \mu^+\mu^-$ and $e^+e^- \to \tau^+\tau^-$ events. Backgrounds from two-photon processes were studied using events generated by the Monte Carlo program of reference [18].

5.1 $e^+e^- \to e^+e^-$

The selection of $e^+e^- \to e^+e^-$ events used information from the electromagnetic calorimeter and the central tracking detectors. The events were required to have low multiplicity, at least two high energy electromagnetic clusters, and had to contain at least two $e^\pm$ candidates, each consisting of an electromagnetic cluster associated to a charged track. The polar angular acceptance was restricted to the barrel part of the electromagnetic calorimeter in order to eliminate the forward regions where the $e^+e^- \to e^+e^-$ cross section is dominated by QED t-channel contributions and has a very strong dependence on polar angle. The selection cuts were:

- $2 \leq$ number of electromagnetic clusters ≤ 8
- $2 \leq$ number of charged tracks ≤ 8
- At least two electromagnetic clusters were required each with energy greater than half the beam energy and within $|\cos\theta| < 0.85$.
- The sum of all electromagnetic energy had to be greater than 80% of the centre of mass energy.

Near the region of overlap between the barrel and endcap parts of the electromagnetic calorimeter ($0.715 < |\cos\theta| < 0.835$) the energy resolution was degraded due to extra material in front of the lead glass. Lower energy thresholds were used for clusters in this region. The final acceptance cut for $e^+e^- \to e^+e^-$ events (see below) required the e^- direction to fall within $|\cos\theta_{e^-}| < 0.7$ and so

the final number of clusters affected by this degradation was small. The association of clusters to charged tracks was done as follows:

- at least two of the three highest energy clusters within $|\cos\theta| < 0.85$ were required to be matched with charged tracks to within $|\Delta\phi| < 3°$ and $|\Delta\theta| < 10°$, where $\Delta\phi$ and $\Delta\theta$ are the differences in azimuthal and polar angles between the track and the cluster.

When two clusters were matched to charged tracks, these were taken to be $e^{\pm}$ candidates. When three clusters were matched to charged tracks, the set corresponding to the two highest energy clusters were used. If one track was assigned to two clusters, the combination with smaller opening angle was chosen. If more than one track was associated to a single cluster the highest momentum track was taken. The measurement of the direction of each particle was optimised by taking the polar angle, θ, from the position of the energy cluster in the calorimeter and the azimuthal angle, ϕ, from the charged track. The final acceptance cuts were:

- The acolinearity angle between the two $e^{\pm}$ candidates was required to be less than 10°.

- The polar angle of the e^- candidate had to satisfy the condition $|\cos\theta_{e^-}| < 0.7$.

Electron and positron were distinguished by the sign of the charge of the track. For a small fraction of events both $e^{\pm}$ candidates were assigned the same charge due to conversions of high-energy radiative photons and some tracking problems near to jet chamber sense-wire planes. The $\cos\theta$ dependence of the fraction of these same sign events was consistent with a uniform distribution, within the angular acceptance of this analysis. For same sign events only the charge of the highest momentum $e^{\pm}$ candidate was considered. The charge determination for this sample was less reliable than that for the sample of opposite sign events. Applying the geometrical acceptance cut randomly on the e^- or e^+ changed the acceptance by less than 0.5% with respect to that defined by the canonical cut on the e^- direction. Since only about 1.2% of events accepted had same sign $e^{\pm}$ candidates, no significant bias to the cross section measurement was introduced. Same sign events were not used for the forward-backward asymmetry measurement. The possible bias was estimated and also found to be negligible.

The multiplicity requirements rejected multihadronic events and most $e^+e^- \to \gamma\gamma$ events. The energy cuts removed events from $e^+e^- \to \tau^+\tau^-$ and two-photon processes such as $e^+e^- \to e^+e^-e^+e^-$. The requirement that charged tracks be associated with two of the three highest energy clusters in the event further reduced the remaining backgrounds, mainly from $e^+e^- \to \gamma\gamma$. The effects of these selection criteria were studied using Monte Carlo generated events, and with checks based on the data themselves.

Figure 10 shows the total energy distribution, after all other cuts have been applied, for Monte Carlo $e^+e^- \to e^+e^-$ events together with the expected background from $e^+e^- \to \tau^+\tau^-$ and $e^+e^- \to$ hadrons. The measured distribution is well described by the Monte Carlo. the events at low energy are mainly due to $e^+e^- \to \tau^+\tau^-$. The inefficiencies of the electromagnetic energy cuts were evaluated using the Monte Carlo. This was checked by making a separate $e^+e^- \to e^+e^-$ selection in which the energy cuts were relaxed but high momentum charged tracks were required. The resulting energy distributions in the data were well represented by the combined Monte Carlo prediction for $e^+e^- \to e^+e^-$ and background and the final cross section measurement did not show a strong dependence on the precise choice of cut applied. As a result of these studies the inefficiencies of the cluster energy cut and the total energy cut were estimated to be $0.1 \pm 0.1\%$ and $0.3 \pm 0.2\%$ respectively.

Another check was carried out by using a set of slightly different calorimeter energy based selection criteria, in which the selection efficiency, background fraction and their energy dependence were different from the standard selection. The energy of the highest energy cluster, E_1, was required to be $E_1 > 0.8E_{beam}$ and the energy of the next highest energy cluster, E_2, was required to be $E_2 > 0.4E_{beam}$. No cut was applied to the total electromagnetic energy. The resulting numbers of events were compared after correcting for inefficiency and backgrounds. They agreed within 1% (the agreement was better than 0.1% at the energy point closest to the peak of the Z^0 resonance which had the best statistical accuracy) and the deviations were consistent with statistical fluctuation.

A small fraction of the $e^+e^- \to e^+e^-$ events contained also a high energy photon due to hard final state bremsstrahlung or interaction of a particle with detector material. For these events a track might not have been matched to a cluster if the particle left only a very small energy deposit in the electromagnetic calorimeter, below the energy threshold for a good cluster. This potential loss of events was reduced by using, for low-momentum ($p < 2$ GeV) tracks, the direction of the track at the origin, before bending in the magnetic field, when matching to clusters. In this way the track could be matched with the cluster from the high-energy photon and the event could be selected. The remaining inefficiency was studied using Monte Carlo generated events and by varying the cuts used to define good clusters and for matching tracks with clusters. It was checked by scanning the events in the data which were rejected by these cuts. These studies gave consistent results and the inefficiency was estimated to be $0.2 \pm 0.1\%$. An additional $0.1 \pm 0.1\%$ inefficiency was included to account for losses due to tracking problems at jet chamber sense-wire planes.

The main background in the final $e^+e^- \to e^+e^-$ sample came from $e^+e^- \to \tau^+\tau^-$ events. This was evaluated by Monte Carlo to be $0.2 \pm 0.1\%$, with an energy dependence of less than 0.1% within the range of this analysis. The Monte Carlo models predicted less than 0.1% background from multihadronic events and negligible backgrounds from two-photon processes. The contribution from $e^+e^- \to \gamma\gamma$ was estimated to be less than 0.1% based on the measured conversion probability (6% [19]) of high energy photons in the material around the beam pipe, and checked by scanning events with no or only one charged track matched with an electromagnetic cluster. The total background fraction at the Z^0 peak was $0.3 \pm 0.2\%$. The effect of the $e^+e^- \to \tau^+\tau^-$ background on the measurement of the $e^+e^- \to e^+e^-$ forward-backward asymmetry was estimated to be smaller than 0.001, assuming the background fraction determined above and the angular distribution predicted by the standard model. The measured forward-backward asymmetry was corrected accordingly.

Because the $e^+e^- \to e^+e^-$ cross section rises steeply with increasing $\cos\theta$, a small imprecision in the definition of the acceptance cut, $|\cos\theta_{e^-}| < 0.7$, could lead to a significant error in the measured cross section and forward-backward asymmetry. This acceptance cut depended on the cluster position reconstructed in the lead glass electromagnetic calorimeter. This was checked by comparing, between data and Monte Carlo simulation, the reconstructed positions of the boundaries between lead glass blocks. These could be identified by the energy sharing between blocks in a cluster. This distribution was sensitive to the detailed simulation of the shower development through the magnet coil, and directly affected the reconstructed cluster coordinates. Showering in the coil led to a correction of the reconstructed θ angle for Bhabha electron clusters of about 0.1° at $|\cos\theta| = 0.7$. An upper limit of 0.15° was set for any apparent offset of the reconstructed lead glass block boundaries from their nominal geometry, corresponding to a systematic uncertainty of 0.5% for the $e^+e^- \to e^+e^-$ cross section and 0.002 for the forward-backward asymmetry. In addition, the finite angular resolution for acceptance and acolinearity cuts led to systematic errors of 0.2% on the cross section and 0.004 on the asymmetry. Displacement of the true event vertex along the beam direction from the centre of the detector could also distort the measurement of $\cos\theta$. Systematic errors of 0.1% for the cross section and 0.001 for the asymmetry were attributed

to this effect.

The systematic errors on the inefficiency, background and acceptance are summarised in Table 4. The overall correction factor, within the acceptance cuts of $|\cos\theta_{e^-}| < 0.7$ and acolinearity angle less than 10°, was 1.005 ± 0.007. There was no significant energy dependence of the acceptance, and the background varied by less than 0.1% over the range of the scan. The total systematic error on the asymmetry measurement was 0.005. The resulting cross section and forward-backward asymmetry measurements are summarised in Tables 8 and 11.

As discussed in Section 6.3, the ALIBABA [20] program was used for estimating the t-channel and s-t interference contributions to $e^+e^- \to e^+e^-$. In Figure 11 the measured angular distribution and acolinearity distribution, at the peak of the Z^0 resonance, are compared with the ALIBABA predictions. The data are unfolded for effects of resolution, inefficiency and backgrounds. The measured distributions agree well with the predictions of the ALIBABA program.

5.2 $e^+e^- \to \mu^+\mu^-$

The selection of $e^+e^- \to \mu^+\mu^-$ events used information from the central tracking detectors together with muon identification from the outer detectors. Time-of-flight (TOF) measurements were used to reject cosmic ray events. The selection cuts were:

- The charged track multiplicity had to be no more than 5.

At least two good tracks, within the polar angular range $|\cos\theta| < 0.95$, had to be separated in azimuthal angle by $\Delta\phi > 320$ mrad and be identified as muons by any one of the following conditions:

- At least 2 muon chamber hits associated with the track within $\Delta\phi = (100 + 100/p)$ mrad, with the momentum p, in GeV.

- At least 4 hadron calorimeter strips associated with the track within $\Delta\phi = (20 + 100/p)$ mrad, with p in GeV. The average number of strips in layers containing hits had to be less than 2 to discriminate against hadrons. For $|\cos\theta| < 0.65$, where tracks traverse all 9 layers of strips in the barrel calorimeter, a hit in one of the last 3 layers of strips was required.

- The track had momentum $p > 15$ GeV and the electromagnetic energy associated to the track within $\Delta\phi < 70$ mrad was less than 3 GeV.

Backgrounds from $e^+e^- \to e^+e^-\mu^+\mu^-$ and $e^+e^- \to \tau^+\tau^-$ were rejected by demanding that the scaled visible energy, F_{vis}, defined as the sum of the momenta of the two muon candidates and the energy of the highest energy electromagnetic cluster in the event, divided by the centre of mass energy, satisfied

- $F_{vis} > 0.6$.

The remaining background from cosmic rays was removed by the following TOF and vertex cuts:

- In the barrel region, at least one TOF measurement was required within 10 ns of that expected for a particle coming from the interaction point. In addition, back-to-back pairs of TOF counters were used to reject cosmic rays which had traversed the detector.

- In the forward region, which is not instrumented with TOF counters, the matching of the central detector tracks to the interaction vertex was used in order to remove cosmic ray background.

The high degree of redundancy provided by the OPAL experiment for the detection of $e^+e^- \to \mu^+\mu^-$ events enabled efficiencies to be calculated from the muon pair data themselves.

A systematic check of the TOF cuts to remove cosmic rays was provided by the matching of the central detector tracks to the interaction point. The inefficiency for $e^+e^- \to \mu^+\mu^-$ events and the remaining background from cosmic rays were both found to be less than 0.1% in the barrel region. In the forward region the events that failed the cut on matching to the vertex, but satisfied looser vertex requirements, were used to estimate a residual background from cosmic rays of $0.1 \pm 0.1\%$ of the total dataset. The efficiency for $e^+e^- \to \mu^+\mu^-$ events to pass the vertex matching cuts is discussed below as part of the study of tracking efficiencies.

For 98% of the tracks in the region close to the edge of the angular acceptance the polar angle was measured using the track seen in the endcap muon chambers. Otherwise the central detector track was used. The systematic uncertainty on the acceptance was less than 0.1%.

The remaining efficiency and background calculations made limited use of Monte Carlo models. The selection efficiency for $e^+e^- \to \mu^+\mu^-$ was predicted to be $91.6\pm0.2\%$, with a background of $1.3\pm0.1\%$ from $e^+e^- \to \tau^+\tau^-$ and no background from $e^+e^- \to e^+e^-\mu^+\mu^-$, where the errors given are purely statistical.

The muon identification efficiencies per track measured directly from the data were: $91.7\pm0.2\%$, $67.7\pm0.4\%$ and $94.2\pm0.2\%$, for the muon chambers, the hadron calorimeter and the electromagnetic calorimeter, respectively. Taking angular correlations into account this led to an overall muon identification efficiency of 99.8% per muon. For the Monte Carlo generated events the overall muon identification efficiency per track was found to be 0.05% higher than that measured in the data. Since both muons were required to be identified, a correction of $-0.1 \pm 0.1\%$ was applied to the acceptance calculated by the Monte Carlo.

A comparison of the scaled visible energy distribution, F_{vis}, between data and normalised Monte Carlo samples is shown in Figures 12 (a), (b) and (c) for the angular regions $|\cos\theta| < 0.8$, $0.8 < |\cos\theta| < 0.9$ and $0.9 < |\cos\theta| < 0.95$. The background below the cut, $F_{vis} < 0.6$, was well described, giving confidence in the reliability of the background prediction. The region dominated by $e^+e^- \to \mu^+\mu^-$ events ($F_{vis} > 0.6$) was not so well described. In the angular region $|\cos\theta| < 0.8$ the peak due to $e^+e^- \to \mu^+\mu^-$ events was slightly broader in the data than in the Monte Carlo, whereas for $|\cos\theta| > 0.9$ it was slightly narrower. The discrepancy was due mainly to the imperfect simulation of stiff tracks close to the sense-wire planes of the jet chamber. A correction of $0.1\pm0.1\%$ was applied to the efficiency calculated by the Monte Carlo to account for the discrepancy within $|\cos\theta| > 0.9$. The loss of events in the barrel region is discussed below.

A direct check on the $\tau^+\tau^-$ background predicted by the Monte Carlo was provided by the distribution of the acoplanarity angle; most $\tau^+\tau^-$ events had a large acoplanarity due to the undetected neutrinos. A subsample of the selected $e^+e^- \to \mu^+\mu^-$ candidates that was enriched in $e^+e^- \to \tau^+\tau^-$ background was obtained by requiring that they satisfied either of the following two additional criteria: $0.6 < F_{vis} < 0.8$, or the event contained at least one track within the muon chamber acceptance that was identified as a muon by only the electromagnetic calorimeter or only the hadron calorimeter. Such tracks were likely to be pions misidentified as muons. Radiative $\mu^+\mu^-$ events were removed from this subsample if the acoplanarity expected from any observed photon

in the event was greater than 10 mrad. The acoplanarity distribution of the remaining events is shown in Figure 13. For acoplanarity greater than 10 mrad data and Monte Carlo agreed well. The excess of data over Monte Carlo in the first bin was due mainly to the differences between data and Monte Carlo discussed above (Figure 12). This check confirmed the level of $e^+e^- \to \tau^+\tau^-$ background predicted by the Monte Carlo model. Because of the limited statistical accuracy with which the check could be performed a systematic error of 0.3% was assigned to the estimate of the $e^+e^- \to \tau^+\tau^-$ background of 1.3%.

A direct search was made for $e^+e^- \to \mu^+\mu^-$ events that failed the selection cuts due to possible track reconstruction problems not already taken into account by the detector simulation. A loose preselection was made of possible lost events, using criteria based mainly on information from the outer detectors, relying as little as possible on the central tracking. An inefficiency of 0.6% was estimated due mainly to $e^+e^- \to \mu^+\mu^-$ events lost when one track was mismeasured close to a jet chamber sense-wire plane. A systematic error of 0.3% was assigned due to $e^+e^- \to \tau^+\tau^-$ or endcap cosmic ray events which might have been wrongly classified as lost muon pairs, and a possible bias due to the weak dependence on tracking of the preselection of events.

The various corrections and systematic errors for the cross section measurement are summarised in Table 5. Note that the effects labelled "muon identification", "F_{vis} resolution for $|\cos\theta| > 0.9$" and "tracking losses" were, in principle, simulated by the Monte Carlo. The quoted corrections were applied to take into account the observed discrepancies between the data and Monte Carlo for these effects. The efficiency within the geometrical acceptance of $|\cos\theta| < 0.95$ was 98.7%. The overall correction factor was 1.084 ± 0.005 and the results of the $e^+e^- \to \mu^+\mu^-$ cross section measurement are given in Table 9. There was no significant energy dependence of either the acceptance or the background fraction over the range of the scan.

For the purpose of the measurement of the forward-backward charge asymmetry additional event selection criteria were imposed to ensure an unambiguous charge determination:

- An acolinearity cut at 15° was applied in order to select back-to-back muon pairs and to suppress radiative events. At the peak of the Z^0 resonance, this cut rejected about 1.3% of the muon pair events.
- It was demanded that there be exactly two good tracks. About 1.8% of events were rejected by this requirement, because they had converted photons or split tracks at sense-wire planes.
- Events where both muons had the same charge were not used for the asymmetry measurement. This rejected about 1.2% of the events remaining after all other cuts.

Since the dominant background was small (1.3%) and was from $e^+e^- \to \tau^+\tau^-$ events, which were expected to have the same asymmetry as $e^+e^- \to \mu^+\mu^-$ events, no correction was applied for the background. Uncertainties due to charge mismeasurement and distortions arising from angular resolutions and displacements of the event vertex were investigated. The overall systematic error of the asymmetry measurement was estimated to be 0.003, much smaller than the statistical error of even the data point with the highest statistics (0.013). The forward-backward asymmetry results are listed in Table 12.

5.3 $e^+e^- \to \tau^+\tau^-$

The selection of $e^+e^- \to \tau^+\tau^-$ events used information from the central tracking detectors and electromagnetic calorimetry to identify events with two back-to-back, collimated, low multiplicity

jets. Time-of-flight measurements were used to reject cosmic ray events and muon identification to reject $e^+e^- \to \mu^+\mu^-$ events. The selection cuts are detailed below.

Multiplicity cuts were imposed to reject Z^0 decays into hadrons:

- $2 \leq$ number of charged tracks ≤ 6, and
- the sum of the number of charged tracks and the number of clusters ≤ 15.

The multiplicity distributions are shown in Figures 14 (a) and (b). The total energy of an event was restricted in order to reject events from $e^+e^- \to e^+e^-(\gamma)$ and two-photon processes:

- $E_{vis} > 0.18\sqrt{s}$, where the total visible energy $E_{vis} = E_{shw} + E_{trk}$, E_{shw} was the total energy in the lead glass calorimeters and E_{trk} was the sum of the track momenta
- $E_{shw} < 0.8\sqrt{s}$, for the region $|\cos\theta| < 0.7$
- $E_{vis} < 1.05\sqrt{s}$ or $E_{shw} < 0.25\sqrt{s}$, for the region $|\cos\theta| > 0.7$, where there was additional material in front of the electromagnetic calorimeter.

The shower and total energy distributions are shown in Figures 14 (c) and (d). Vertex and TOF cuts were imposed to remove cosmic ray events. Finally,

- the $e^+e^- \to \mu^+\mu^-$ events identified by the criteria described in section 5.2 were removed.

The remaining background was mostly from multihadronic events and events from two-photon processes and $e^+e^- \to e^+e^-\gamma$, which were characterised by relatively wide-spread or acolinear event topology. In order to suppress them, a narrow back-to-back structure was required. Charged tracks and lead glass clusters, each treated as separate particles, were combined in the following way. First the highest energy particle in the event was selected and a cone with a half angle of 35 degrees was defined around it. The particle with the next highest energy inside the cone was combined with the first. The momenta of the combined particles were added and the direction of the sum was used to define a new cone, inside which the next highest energy particle was again looked for. This procedure was repeated until no more particles were found inside the cone. Similarly, starting with the highest energy particle among the remainder, a new cone was initiated and treated in the same way. This process continued until finally all the particles in the event had been assigned to a cone. At least one charged particle was required for each cone, and the sum of the energy in the lead glass and the track momenta in a cone had to have more than 1% of the beam energy.

- Events which had exactly two such cones were selected as $e^+e^- \to \tau^+\tau^-$ candidates.

The direction of each τ was approximated by that of the total momentum vector of its cone of particles. The vectorial difference between the momenta of the two τ jets was used to define an event axis.

The following final acceptance cuts rejected most of the remaining background from two-photon processes:

- acolinearity angle $< 15°$ and
- event axis satisfied $|\cos\theta| < 0.9$.

The acolinearity angle distribution and the $|\cos\theta|$ distribution of the event axis are shown in Figures 14 (e) and (f). Monte Carlo generated $e^+e^- \to \tau^+\tau^-$ events were used to calculate

the geometrical acceptance and efficiency of this selection. The total efficiency was $76.9 \pm 0.2\%$ at $\sqrt{s} = M_Z$. The quoted uncertainty includes only the Monte Carlo statistical error. The 15° acolinearity cut introduced a significant energy dependent correction factor to the acceptance, which was calculated using KORALZ. At the extreme points of the energy scan this correction factor was approximately 2%.

The distributions of the variables used for the selection are shown in Figure 14, along with the Monte Carlo expectations. The hatched parts of the histograms correspond to background contributions: multihadronic, $e^+e^-(\gamma)$, $\mu^+\mu^-(\gamma)$ and two-photon ($e^+e^-e^+e^-$ and $e^+e^-\mu^+\mu^-$ only) events. The systematic errors arising from the specific choice of selection cuts were estimated from the changes in the cross section which resulted when these cut values were varied over reasonable ranges. With the exception of the cut on the sum of the number of charged tracks and clusters, there was no indication of any systematic variation beyond that expected from the statistical errors. Systematic errors, reflecting the limited statistical sensitivity of this procedure, were assigned to each of the cuts and added in quadrature resulting in a total of 0.8%.

In order to determine the systematic uncertainty associated with the measurement of the event axis used to define the geometrical acceptance the analysis was repeated, first using only tracks, and secondly using only clusters, to measure the event axis. From the resulting changes in cross section a systematic error of 0.6% was estimated.

By examining the distribution of vertices, and scanning events which were close to the vertex cuts, a systematic error of 0.1% was assigned to the effect of these cuts. The TOF inefficiency was found to be less than 0.1% by checking the vertex distribution of events which had no TOF hits. This was assigned as a systematic error. Remaining backgrounds from cosmic ray, beam-gas or beam-wall events were estimated at $0.2 \pm 0.1\%$.

The background coming from multihadronic events was estimated at 0.4% using Monte Carlo events. The difference between the predictions of the JETSET 7.2 and HERWIG 4.3 programs was included in the estimate of the systematic error. The estimate of the uncertainty in the multihadronic background was affected by the discrepancy between data and Monte Carlo in the multiplicity distribution of figure 14(b). The background simulation was best checked in the high multiplicity region, were the proportion of multihadronic events was largest. In this region a small excess of data over Monte Carlo was observed. The analysis was repeated with the multiplicity cut relaxed and the results were compared with those obtained from the standard $e^+e^- \to \tau^+\tau^-$ selection. As a result an overall uncertainty of 0.4% was assigned to the hadronic background fraction.4%.

The background from $e^+e^- \to \mu^+\mu^-(\gamma)$ events was estimated to be $0.6 \pm 0.2\%$ by using Monte Carlo generated events and taking into account the inefficiencies discussed in section 5.2. A direct search for residual $e^+e^- \to \mu^+\mu^-$ events within the $e^+e^- \to \tau^+\tau^-$ data sample was performed in order to check the calculated muon identification efficiency. One of the τ candidates was required to have electromagnetic energy less than 10% and visible energy larger than 60% of the beam energy. Of the $e^+e^- \to \mu^+\mu^-$ events within the geometrical acceptance 97% should have had a visible energy between 88% and 112% of the centre of mass energy. The numbers of predicted and observed events in this region agreed well within the statistical error of 0.2%.

The background from $e^+e^- \to e^+e^-(\gamma)$ events was predicted by Monte Carlo to be 0.3%. This was checked by repeating the analysis after removing the high visible energy cut. A systematic error of 0.3% was estimated.

Background from two-photon processes entered at lower visible energies as seen in Figure 14(d).

The Monte Carlo predicted 4.1±0.8 pb from $e^+e^- \to e^+e^-e^+e^-$ and 1.1±0.4 pb from $e^+e^- \to e^+e^-\mu^+\mu^-$, while the other two-photon contributions were negligibly small. This was checked by comparing the angular distribution of the missing momentum vector in events between data and Monte Carlo, especially in the forward direction where two-photon events were concentrated. As a result a total systematic uncertainty of 4.3 pb was assigned to backgrounds from two-photon processes.

The correction factors and systematic errors are summarised in Table 6. The efficiency within the geometrical acceptance of $|\cos\theta| < 0.90$ was 88.8%. The overall correction factor at the peak was 1.276 ± 0.013. The cross section results are given in table 10.

For the measurement of the forward-backward asymmetry the charge of each τ-jet was defined by the sum of the charges of the tracks within its cone. The charge assigned to each τ had to be different and at least one τ was required to have a charge of $+1$ or -1. About 1.7% of the sample was rejected due to this criterion. From this number and a comparison with the Monte Carlo simulation, the forward-backward misassignment probability was found to be small. The effect of residual $e^+e^- \to e^+e^-$ background, angular resolution and displacement of the event vertex on the forward-backward asymmetry was also studied. An overall uncertainty of 0.003 was assigned to the forward-backward asymmetry measurement. The asymmetry results are summarised in Table 13.

5.4 $e^+e^- \to l^+l^-$

For some of the fits (described in section 6.5) the data were analysed under the assumption of lepton universality. In these cases the individual cross section and forward-backward asymmetry measurements from $e^+e^- \to e^+e^-$, $e^+e^- \to \mu^+\mu^-$ and $e^+e^- \to \tau^+\tau^-$ analyses were still used as separate input data, but were combined in the fit by assuming a universal leptonic decay width of the Z^0 and universal leptonic couplings.

It has been demonstrated in sections 5.1, 5.2 and 5.3 that the analyses of the three lepton pair decay channels each suffered from different sources of systematic uncertainty; this resulted in the definition of rather different geometrical acceptances for each channel. By retaining the separate e^+e^-, $\mu^+\mu^-$ and $\tau^+\tau^-$ measurements, even after the assumption of lepton universality, the optimum use was made of all the available data, without the need to compromise the analysis of any one channel by the requirements of another.

There was no overlap between the $e^+e^- \to e^+e^-$ and $e^+e^- \to \mu^+\mu^-$ samples, nor was any inefficiency introduced by separating the two samples. The cuts used to discriminate between the other leptonic channels were chosen to be complementary. The $e^+e^- \to e^+e^-$ and $e^+e^- \to \tau^+\tau^-$ channels were distinguished according to whether the total energy in the electromagnetic calorimeter was greater or smaller than 80% of the centre of mass energy. The cuts used to identify $e^+e^- \to \mu^+\mu^-$ events were used to explicitly veto such events in the $e^+e^- \to \tau^+\tau^-$ sample. Hence, on combining the three sets of measurements in the fits, by assuming lepton universality, an inclusive analysis of $e^+e^- \to l^+l^-$ events was obtained. Within the region of common geometrical acceptance, the systematic errors which were assigned to the separate measurements due to uncertainties in signal identification efficiencies and background misidentification probabilities of each lepton species were almost entirely anticorrelated with respect to one another and cancelled in the combined $e^+e^- \to l^+l^-$ analysis. Also, the fact that the remaining systematic uncertainties were largely uncorrelated between the three analyses led to a reduced systematic error in the combined analysis.

The error matrix used in the fitting procedure took into account the full correlation matrix

of systematic uncertainties between the three lepton-pair analyses. The effective final systematic uncertainty in the leptonic cross section, due to the lepton event selections, was somewhat less than 0.4%.

6 Analysis

6.1 Summary of measured cross sections and forward-backward asymmetries

In extracting final results the measurements of the hadronic line-shape and the lepton line-shapes and forward-backward asymmetries performed with the 1990 data set were combined with our previously published measurements [1,2], with the exception of the $e^+e^- \rightarrow e^+e^-$ channel, for which the 1989 data were re-analysed to reflect the same kinematic acceptance region defined for the 1990 analysis. [1]

In Table 7 the numbers of hadronic events, the integrated luminosities and the corresponding acceptance corrected hadronic cross sections are listed as functions of the centre of mass energy, separately for the data taken in 1989 and 1990. Tables 8, 9 and 10 list the numbers of lepton pair events observed as functions of centre of mass energy together with the corresponding luminosities and cross sections. For the e^+e^- events, the cross section is given for the acceptance $|\cos\theta_{e^-}| < 0.7$ and an acolinearity $< 10°$. For the $\mu^+\mu^-$ and $\tau^+\tau^-$ events the total cross sections, after all corrections for acceptance and efficiency, are given. The error on the cross sections includes the statistical errors of the event sample and the point-to-point systematic errors on the acceptance and luminosity. The absolute acceptance errors and an overall normalisation error of 0.8% and 2.2% deriving from the luminosity measurements in 1990 and 1989 respectively are not included in the tables, but were taken into account in the subsequent analysis.

The forward-backward charge asymmetries measured for leptons at different centre of mass energies are listed in Tables 11, 12 and 13. For the e^+e^- analysis these have been evaluated at each centre of mass energy point by counting the numbers of events in which the electron direction was in the forward and backward polar angular regions, N_F and N_B, and using the definition $A_{FB} = (N_F - N_B)/(N_F + N_B)$. In the $\mu^+\mu^-$ and $\tau^+\tau^-$ analyses the direction of the anti-lepton was used for the determination of the forward-backward asymmetry. The forward-backward asymmetries were determined both by the counting method (applying bin-by-bin efficiency corrections in $|\cos\theta|$), and by fitting the function $(1 + \cos^2\theta) + b\cos\theta$ to the inferred $\cos\theta$ distributions of the leptons using a maximum-likelihood method. The forward-backward asymmetry within an angular acceptance $|\cos\theta| < K$, $A_{FB}(K)$, could then be calculated from the fitted parameter b, using the relationships $A_{FB} = 3b/8$ and

$$A_{FB}(K) = \frac{4K}{3 + K^2} A_{FB}$$

In each case the asymmetry is quoted only within the experimental polar angular acceptance region for each final state. Whereas the results of the counting method make no assumptions about the underlying angular distribution of the events, the maximum likelihood method offers a somewhat enhanced statistical sensitivity and, in the absence of charge asymmetric inefficiencies, does not require efficiency corrections. The presence of radiation, and in particular initial state radiation, distorts the $\cos\theta$ distribution with respect to the naive form assumed in this fitting method. We have checked that, at the present level of statistics, these distortions had no significant effect on

[1] For the reanalysis of the 1989 data only the two highest energy clusters in the event were considered for matching to charged tracks. This led to a reduction in efficiency by approximately 0.5%.

our results. In the fits which follow, the forward-backward asymmetries derived from the maximum likelihood fits were used for the $\mu^+\mu^-$ and $\tau^+\tau^-$ channels.

6.2 Treatment of the LEP energy scale

During the scan of the Z^0 resonance in 1990, data were taken at seven nominal centre of mass energy points. The energy of the colliding beams was measured by the SL division, for each fill of the LEP machine. Typical variations from the mean beam energy were less than 10 MeV. Measurements at nearby energies were combined into one data point at the luminosity-weighted average energy. Since different subsets of the total data sample were used for each measurement, this resulted in slightly different energy values in each table.

The uncertainties in the LEP energy scale are discussed in references [21,22]. The 0.02 GeV uncertainty in the absolute centre-of-mass energy scale of the LEP machine, close to the Z^0 peak, dominates the uncertainty on M_Z. The point-to-point energy scale uncertainty, the fill-to-fill reproducibility and the beam energy spread also have an important impact on the results of our measurements. All these effects may potentially distort the line shape and, given the current level of statistical precision of our measurements, must be correctly taken into account. The uncertainty in the point-to-point LEP energy scale is taken as 10 MeV, the fill-to-fill energy scale uncertainty is assumed to be of the same order and the beam energy spread results in a one standard deviation spread in the centre of mass energy of about 50 MeV, known to about 5 MeV. The point-to-point energy scale uncertainty dominates other contributions to the systematic uncertainty on Γ_Z, but does not introduce a significant net bias in the measurement; it contributes approximately 5 MeV to the uncertainty on Γ_Z. The effect of 10 MeV fill-to-fill fluctuations in the centre of mass energy is negligible, because measurements at each energy point contained data from at least 5 fills. The beam energy spread uncertainty, on the other hand, is large enough to have a significant, albeit second order, net bias on the measured line-shape. We correct for this in our fitting procedure by estimating iteratively the effect of the beam energy spread on the measured cross section at each energy point using the Taylor expansion:

$$\Delta\sigma(E) \approx \frac{d^2\sigma(E)}{dE^2}\Delta E^2$$

where $\sigma(E)$ expresses the energy dependence of the total cross section and ΔE is the centre of mass energy spread. The differentiation of $\sigma(E)$ is carried out numerically at each energy point. We have verified that, for a 50 MeV centre of mass energy spread, this approximation reproduces well the results of convoluting a Gaussian with $\sigma = 50$ MeV with the line-shape. For our line-shape measurements, this results in a correction to Γ_Z of -4 ± 1 MeV. Since the centre of mass energy spread is known to about 5 MeV, no additional uncertainty is ascribed to this effect.

In our fits the correlation matrix of the uncertainties in the LEP energy scale for data taken in 1989 and 1990 was also taken into account. To facilitate comparison with other LEP experiments, we quote experimental errors on M_Z derived from a fit ignoring all energy uncertainties. The second error quoted on M_Z reflects the uncertainties in the LEP machine energy, which are correlated for the LEP experiments.

6.3 Treatment of QED radiative corrections

Radiative corrections significantly modify the $e^+e^- \to f\bar{f}$ cross sections and forward-backward asymmetries with respect to the tree level (Born) calculation. Photonic corrections, defined as the set of all diagrams incorporating an additional real or virtual photon with respect to the Born diagrams, form a gauge-invariant subset and can therefore be considered independently of other virtual corrections [23].

For the parametrisation of the total and differential cross section of the $q\bar{q}$, $\mu^+\mu^-$ and $\tau^+\tau^-$ channels the program ZFITTER [24] was used. This is an updated version of the program package ZBIZON [25], which was used in our previous publications [1,2]. In this program photonic corrections are included as a complete $O(\alpha)$ calculation; leading $O(\alpha^2)$ corrections and the exponentiation of soft photons are also included. The total cross section agrees with that obtained from the program ZSHAPE [26] to better than 0.2%, for all final state fermions concerned. The effect of cuts on the differential cross section reproduces the results obtained with KORALZ [16] to better than 0.5% over the range of the energy scan. This allows us to fit the lepton pair cross sections and forward-backward asymmetries determined within both the geometric acceptance and the acolinearity cuts applied in each analysis.

The treatment of the $e^+e^- \to e^+e^-(\gamma)$ differential cross section is technically complicated by the presence of t-channel exchange diagrams; these diagrams are not included in the ZFITTER program.

In our previous publication [2] a parametrisation of the differential cross section for $e^+e^- \to e^+e^-(\gamma)$ based on the formulae given in references [27] was used. The approximations made in this parametrisation are expected to be valid only within a restricted phase space, which is defined in a way that does not correspond directly to experimentally accessible cuts. Application of these formulae is therefore complicated by the need for Monte Carlo corrections to map the experimental acceptance onto the phase space of the calculated cross section. The correction required was minimised by explicitly rejecting events with large angle hard radiative photons; even so, the size of the correction varied from a minimum of -0.3% at the peak, up to -5% at 95 GeV. Once the acceptance cuts were imposed, the s-channel part of the parametrisation differed from the parametrisation of KORALZ (by 1.5% at the peak) thus introducing a small, but increasingly significant, bias. Finally, there was no reliable estimate of the systematic uncertainty for the t-channel exchange and s-t-channel interference, and no other sufficiently accurate calculations with which to compare the results. In view of these difficulties, the effect of the t-channel was reduced by the use of an asymmetric acceptance cut for the e^+e^- channel: $-0.7 < \cos\theta_{e^-} < 0.4$. A systematic uncertainty corresponding to 25% of the remaining t-channel contribution was assigned to the total cross section at each energy point.

Since that publication, a new calculation of the cross section for the process $e^+e^- \to e^+e^-(\gamma)$ has become available in the form of the program ALIBABA [20]. This calculation includes, in lowest order, all diagrams associated with the s- and t-channel exchange of a γ or a Z^0, and all possible interference terms between them. Weak corrections are calculated in $O(\alpha)$, except for propagator terms in which some of the $O(\alpha^2)$ terms are included. Photonic corrections are treated exactly to first order. The $O(\alpha^2)$ corrections are evaluated in the leading log approximation and soft photons are resummed to all orders. The authors assign an uncertainty of 0.5% to the calculation of the cross section, over the full range of the energy scan, for scattering angles greater than 10°.

In the program, acceptance cuts may be directly applied to the direction of the e^-, and to the acolinearity of the final state e^+e^- pair: this eliminates the need for Monte Carlo corrections to the

experimental acceptance. For the acceptance cuts applied to the data, the s-channel parametrisation in ALIBABA is found to agree with that of KORALZ and ZFITTER to better than 0.2%, and the forward-backward asymmetries to better than 0.001, over the full range of the energy scan.

Because the ALIBABA program is too slow to be used directly in the fitting process, and in order to ensure a consistent treatment of s-channel exchange for all processes, we have adopted the following ansatz. For the model independent fits and those based on improved Born approximations, which cannot be directly formulated in terms of Standard Model parameters, we constrain the top quark mass M_t=150 GeV, and the Higgs mass M_H=100 GeV and use the value of α_s=0.118, determined from the measured hadronic jet production rates in Z^0 decays [28], in the ALIBABA calculation. For each point of the energy scan, the calculated t-channel contribution, including s-t-channel interference, is then added to the total, forward and backward s-channel cross sections calculated, in a manner analogous to the other Z^0 decay modes, with the ZFITTER program. (Note that ZFITTER also allows the acceptance defining cuts used for the $e^+e^- \rightarrow e^+e^-(\gamma)$ channel). We assign the quoted uncertainty of 0.5% to the calculated t-channel contributions. The resulting set of cross sections and forward-backward asymmetries are then fitted directly to the measured data points. This technique ensures a transparent error calculation which preserves the gaussian nature of the experimental statistical errors.

This procedure, in principle, results in both a loss of information and a possible bias. We have therefore repeated the model independent fits varying the input parameter M_t from 50 to 230 GeV in the ALIBABA calculations: this changed the results of the fits concerned by less than 5% of the respective experimental uncertainty.

For the fits discussed in section 6.5.4, which explicitly reference the Standard Model, we have used the program ALIBABA to calculate the contribution to the cross section and forward-backward asymmetry due to t-channel exchange and s-t interference terms at each centre of mass energy point, in a grid which treats the Standard Model set of input parameters (M_Z, M_t, M_H, α_s) as interpolation points.

6.4 The Hadronic Line Shape

All fits are based on a χ^2 minimisation procedure, which takes into account the full correlation matrix of the experimental uncertainties. We perform a model independent fit to the hadronic line-shape data based on a Breit-Wigner line-shape with s-dependent width. Excluding photonic corrections the line-shape is parametrised as:

$$\sigma(s) = \sigma_{had}^{pole} \frac{s\Gamma_Z^2}{(s - M_Z^2)^2 + \frac{s^2}{M_Z^2}\Gamma_Z^2}$$

where σ_{had}^{pole} represents the resonance hadronic cross section at $s = M_Z^2$ (in the absence of initial state photonic corrections). The s-dependence of the propagator is introduced to account for the effect of higher order virtual corrections (see section 6.5.1 and reference [23]). The fit, including the convolution of the cross section given above with photonic corrections, is performed with the program ZFITTER[24]. We treat M_Z, Γ_Z and σ_{had}^{pole} as free parameters. The results are summarised in Table 14. The parameter values obtained are

$$M_Z = 91.156 \pm 0.009 \text{ (exp)} \pm 0.02 \text{ (LEP) GeV}$$

$$\Gamma_Z = 2.492 \pm 0.017 \text{ GeV}$$

$$\sigma_{had}^{pole} = 41.01 \pm 0.41 \text{ nb.}$$

The χ^2 value for this fit is 8.8 for 15 degrees of freedom. The errors on M_Z have been separated into the experimental error and the uncertainty due to the LEP beam energy. The error on Γ_Z includes a contribution of 5 MeV due to the beam energy uncertainty. Figure 15 shows the central values and the confidence contours for our measurement of Γ_Z and σ_{had}^{pole}.

The Standard Model predictions for the pole cross section, σ_{had}^{pole}, the width, Γ_Z, and the partial decay widths discussed below are a function of M_Z and depend on the values assumed for the top quark mass, M_t, the Higgs mass, M_H and the strong coupling constant, α_s. In order to compare our measurement with the Standard Model predictions we calculate those assuming $M_t = 150$ GeV, $M_H = 100$ GeV, and setting $\alpha_s = 0.118$. The errors on the predictions are derived by allowing a variation of M_t from 50 to 230 GeV, M_H from 50 to 1000 GeV and α_s by ± 0.008 . Figure 15 shows that the effect of varying the number of light neutrino generations from 3 to 4 is large compared to the uncertainty in the predicted values of σ_{had}^{pole} and Γ_Z.

The number of light neutrinos, N_ν, can also be found by using the Standard Model partial widths for $M_t = 150$ GeV and $M_H = 100$ GeV in a fit to M_Z and N_ν [15]. This two parameter fit yields

$$M_Z = 91.154 \pm 0.009 \text{ (exp)} \pm 0.02 \text{ (LEP) GeV}$$

$$N_\nu = 3.046 \pm 0.068 \text{ (exp)} \pm 0.04(M_t, M_H)$$

with a χ^2 of 9.3 for 16 degrees of freedom. Though this method to determine the number of light neutrinos is the statistically most precise one, it relies on the validity of the Standard Model prediction for all the Z^0 partial widths. This constraint can be removed by a measurement of the hadronic and the leptonic partial widths.

6.5 Results of the Combined Fits to Hadronic and Leptonic data

6.5.1 Model Independent Fits

In a first approach to fitting the combined hadronic and leptonic data, we use a generalisation of the improved Born approximation [23] for the leptonic differential cross section of the s-channel exchange. The resulting kernel, to be convoluted with the photonic corrections discussed above, is of the form:

$$\frac{2s}{\pi\alpha^2}\frac{d\sigma}{d\cos\theta}(e^+e^- \to l^+l^-) = \left(\frac{1}{1-\Delta\alpha}\right)^2 (1+\cos^2\theta) \qquad (1)$$

$$+\frac{2}{1-\Delta\alpha}\text{Re}\left\{\chi(s)\left[\kappa_{\gamma Z}^s \hat{v}_l^2(1+\cos^2\theta) + 2\kappa_{\gamma Z}^a \hat{a}_l^2 \cos\theta\right]\right\}$$

$$+|\chi(s)|^2\left[\kappa_{ZZ}^s(\hat{a}_l^2+\hat{v}_l^2)^2(1+\cos^2\theta) + 8\kappa_{ZZ}^a \hat{a}_l^2 \hat{v}_l^2 \cos\theta\right]$$

with

$$\chi = \frac{G_F M_Z^2}{8\pi\alpha\sqrt{2}} \frac{s}{s - M_Z^2 + is\Gamma_Z/M_Z}$$

In this expression the first term accounts for the pure photon exchange channel, the second term for γZ^0 interference and the third for pure Z^0 exchange. G_F is the Fermi coupling constant and α is the fine structure constant. $\Delta\alpha$ is the QED vacuum polarisation correction evaluated at $M_t = 100$ GeV. The variation of $\Delta\alpha$ over the range of M_t considered here is negligible.

In the improved Born approximation, the effect of higher order virtual corrections expected in the Standard Model framework is approximated by the introduction the QED vacuum polarisation correction factor, $\Delta\alpha$, of effective axial vector and vector couplings, which we label $\hat{a}_l$ and $\hat{v}_l$, and of an s-dependence of the width in the propagator. In the improved Born approximation $\hat{a}_l^2$ and $\hat{v}_l^2$ are taken to be real.

The four coefficients $\kappa_{\gamma Z}^s$, $\kappa_{\gamma Z}^a$, κ_{ZZ}^s and κ_{ZZ}^a are equal to 1 in the improved Born approximation. They are introduced here to account for residual effects of higher order virtual corrections. In this notation the super-scripts "s" and "a" are used to distinguish the κ coefficients terms symmetric and antisymmetric in $\cos\theta$ respectively. Radiative corrections are sensitive to the detailed structure of the underlying theory: in general each of the κ coefficients should be treated as a free parameter and thus the differential cross section is expressed in terms of four independent parameters. Higher order corrections may also introduce an s-dependence in the κ coefficients. In the framework of the Standard Model, however, this s-dependence is negligible at the current level of sensitivity; therefore no s-dependence is assigned to the κ parameters in our fitting procedure. As a further approximation we constrain the κ coefficients to be real.

The γZ^0 interference term in Equation (1), $\mathrm{Re}\{\chi(s)\}\,\kappa_{\gamma Z}^s \hat{v}_l^2$, vanishes at $s = M_Z^2$, in the absence of photonic corrections, and contributes less than 0.2% to the cross section over the full range of the energy scan. We therefore fix $\kappa_{\gamma Z}^s \hat{v}_l^2$ to the Standard Model prediction for $M_t = M_H = 100$ GeV. The effect of varying $\kappa_{\gamma Z}^s \hat{v}_l^2$, by up to a factor 10 with respect to the value assigned it by this procedure does not significantly affect the quality of the fits nor the results obtained for the other three parameters.

For an acceptance interval symmetric in $\cos\theta$, the remaining three independent parameters are related to the data as follows. The parameter $\kappa_{ZZ}^s(\hat{a}_l^2 + \hat{v}_l^2)^2$ normalises the contribution to the cross section from the s-channel Z^0 exchange. Neglecting non factorisable contributions from electroweak box corrections, the parameter $\kappa_{ZZ}^s(\hat{a}_l^2 + \hat{v}_l^2)^2$ can be rewritten in terms of the leptonic partial widths, or peak cross section, as:

$$\kappa_{ZZ}^s(\hat{a}_l^2 + \hat{v}_l^2)^2 \equiv \left(\frac{24\pi\sqrt{2}}{G_F M_Z^3}\right)^2 \frac{\Gamma_{ee}\Gamma_{l^+l^-}}{\delta_{QED}^2} = \frac{3\pi}{2}\left(\frac{8}{G_F}\frac{\Gamma_Z}{M_Z^2}\right)^2 \frac{\sigma_{ll}^{\mathrm{pole}}}{\delta_{QED}^2}$$

where $\sigma_{ll}^{\mathrm{pole}}$ is the resonant cross section at $s = M_Z^2$ (in the absence of initial state photonic corrections) and $\Gamma_{l^+l^-}$ is the partial decay width of the Z^0 for the final state leptons in question; Γ_{ee} is the partial decay width of the Z^0 to electrons. The factor $\delta_{QED} = 1 + \frac{3}{4}\frac{\alpha}{\pi}$ accounts for the effect of final state radiation. By convention the effect of final state radiation is absorbed in the definition of the partial widths, whereas it is unfolded when quoting effective couplings. When the electron data are combined in the fit with those for the other leptonic decays Γ_{ee} and $\Gamma_{l^+l^-}$ can each be determined.

For a fixed normalisation, and in the absence of photonic corrections, the forward-backward asymmetry at the peak is determined by $\kappa^a_{ZZ}\hat{a}^2_l\hat{v}^2_l$, whereas the ratio $(\mathrm{Re}\{\chi(s)\}/|\chi(s)|^2)\kappa^a_{\gamma Z}\hat{a}^2_l$ determines the energy evolution of the forward-backward asymmetry. Since $\mathrm{Re}\{\chi(s)\}$ vanishes at the peak, the parameters $\kappa^a_{\gamma Z}\hat{a}^2_l$ and $\kappa^a_{ZZ}\hat{a}^2_l\hat{v}^2_l$ are only weakly correlated. In order to account for the possibility of a negative forward-backward asymmetry at $s = M^2_Z$, negative values of $\kappa^a_{ZZ}\hat{a}^2_l\hat{v}^2_l$ are allowed.

The hadronic line-shape is parametrised in an analogous manner, but, given that no information on the forward-backward asymmetry of quarks is included in this analysis, only the terms symmetric in $\cos\theta$ are retained. In all the fits discussed below the hadronic line-shape data are included, and M_Z and Γ_Z are treated as free parameters, although they are no longer mentioned explicitly.

In a first step, we carry out a fit to our combined data set, parametrised in terms of the hadronic and leptonic partial widths Γ_{had}, Γ_{ee}, $\Gamma_{\mu\mu}$, $\Gamma_{\tau\tau}$, and the parameters $\kappa^a_{ZZ}\hat{a}^2_l\hat{v}^2_l$ and $\kappa^a_{\gamma Z}\hat{a}^2_l$. In this fit no assumption of lepton universality is made with respect to the partial widths. The leptonic partial widths thus obtained, shown in Table 15 column 3, are an explicit test of lepton universality: they are found to be consistent with each other. The parameters $\kappa^a_{ZZ}\hat{a}^2_l\hat{v}^2_l$ and $\kappa^a_{\gamma Z}\hat{a}^2_l$ are also extracted separately for each of the three lepton species, but no factorisation between initial and final state couplings is performed. These are listed in column 3 of Table 15: each of the three lepton data sets yields consistent results for these parameters. The correlation matrix for the parameters extracted from this fit is shown in Table 2 of Appendix A.

As a further check of the consistency of our data, we also carry out separate fits to each of the e^+e^-, $\mu^+\mu^-$ and $\tau^+\tau^-$ data sets, explicitly assuming lepton universality between initial and final state with respect to all the parameters extracted. The results of these fits, summarised in Table 16 are in excellent agreement for all three data sets. Therefore, for the subsequent fits, all our data are included and lepton universality is assumed with regards to all the parameters extracted.

The results of a fit to the combined data set, parametrised in terms of Γ_{had}, $\Gamma_{l^+l^-}$, $\kappa^a_{ZZ}\hat{a}^2_l\hat{v}^2_l$ and $\kappa^a_{\gamma Z}\hat{a}^2_l$ are shown in Table 15 column 2. The different uncertainties in the values obtained for Γ_{had} with and without the assumption of lepton universality reflect the use of $\Gamma_{l^+l^-}$ and Γ_{ee} respectively in the two fits. Figures 16 and 17 show the corrected cross sections and forward-backward asymmetries as functions of $\sqrt{s}$, together with the corresponding fitted curves. In Figures 18 (a), (b), and (c) the confidence level contours of our result are shown in the $\kappa^a_{ZZ}\hat{a}^2_l\hat{v}^2_l$ vs. $\kappa^a_{\gamma Z}\hat{a}^2_l$, $\kappa^a_{ZZ}\hat{a}^2_l\hat{v}^2_l$ vs. $\Gamma_{l^+l^-}$, and Γ_{had} vs. $\Gamma_{l^+l^-}$ planes. Also shown is the Standard Model prediction for these parameters, allowing the masses of the top quark, M_t, and of the Higgs particle, M_H, to vary within the range $50 < M_t < 230$ GeV and $50 < M_H < 1000$ GeV. The measured values are in good agreement with the Standard Model prediction for the ranges of M_t and M_H considered here. The correlation matrix for the parameters extracted from this fit is shown in Table 1 of Appendix A.

From the measured hadronic and leptonic partial widths the ratio

$$R_Z \equiv \Gamma_{had}/\Gamma_{l^+l^-} = 20.95 \pm 0.22$$

is determined. The Standard Model prediction is $R^{SM}_Z = 20.8 \pm 0.1$ (M_t, M_H, α_s), where the range results from a variation of M_t between 50 and 230 GeV, M_H between 50 and 1000 GeV and the strong coupling constant, $\alpha_s = 0.118 \pm 0.008$. Our measurement is consistent with the prediction of the Standard Model.

6.5.2 Improved Born Approximation Fits

Here we fix the four κ coefficients in expression (1) to unity, thus recovering the improved Born approximation, and perform a fit for the effective axial vector and vector couplings, $\hat{a}_l^2$ and $\hat{v}_l^2$. In order to account for the possibility of a negative forward-backward asymmetry at $s = M_Z^2$, negative values of $\hat{v}_l^2$ are allowed.

The results from this fit are given in Table 17, column 1. The value of $\hat{a}_l^2$ is determined mainly by the cross section measurements and the value of $\hat{v}_l^2$ mainly by the asymmetry measurements. It is not possible to determine the signs of $\hat{a}_l$ and $\hat{v}_l$ using these data alone. Comparing the results of this fit with those from the more general parametrisation, listed in Table 15, it can be seen that at the current level of sensitivity the three κ parameters are consistent with unity.

Within the improved Born approximation the differential cross section may be reparametrised in terms of an effective ρ parameter, ρ_Z, and an effective weak mixing angle, $\sin^2\bar{\theta}_W$ [23], by substituting in (1) the following expressions for the coupling constants:

$$\hat{a}_l^2 \to \rho_Z \qquad \text{and} \qquad \hat{v}_l^2 \to \rho_Z(1 - 4\sin^2\bar{\theta}_W)^2.$$

Note that this parametrisation cannot accommodate negative values for the forward-backward asymmetry at $s = M_Z^2$. The results of a fit using this parametrisation are given in Table 17, column 2. Figure 19 shows the one standard deviation confidence level contour in the ρ_Z vs. $\sin^2\bar{\theta}_W$ plane. Because $\hat{v}_l$ enters only quadratically in the improved Born approximation, the confidence level contour obtained from the fit is symmetric about the axis $\sin^2\bar{\theta}_W = 0.25$. The stars indicate our best fitted values:

$$\rho_Z = 0.998 \pm 0.009 \qquad \text{and} \qquad \sin^2\bar{\theta}_W = 0.238^{+0.030}_{-0.006},$$

where the central value of $\sin^2\bar{\theta}_W < 0.25$ has been chosen.

In this fit, ρ_Z is determined mainly by the cross section measurements and $\sin^2\bar{\theta}_W$ mainly by the asymmetry measurements. Note that, whereas the error on $\hat{v}_l^2$ is gaussian, the error on $\sin^2\bar{\theta}_W$ is non-gaussian: the positive and negative uncertainties are asymmetric and their size is very sensitive to the central value obtained, due to the symmetry of the confidence level contours about $\sin^2\bar{\theta}_W = 0.25$. The leptonic couplings can be specified with a single parameter by making use of the approximate relationship between ρ_Z and $\sin^2\bar{\theta}_W$ valid in the Standard Model with minimal Higgs structure [23]:

$$\sin^2\bar{\theta}_W^{\mathrm{IBA}} = \frac{1}{2}\left(1 - \sqrt{1 - \frac{4A}{\rho_Z M_Z^2(1-\Delta\alpha)}}\right) \tag{2}$$

where $A = (\pi\alpha)/(\sqrt{2}G_F)$ and the superscript IBA refers to the improved Born approximation. The results of a fit with this constraint imposed are given in Table 17, column 3. For the effective weak mixing angle we obtain:

$$\sin^2\bar{\theta}_W^{\mathrm{IBA}} = 0.2337 \pm 0.0021$$

This value of $\sin^2\bar{\theta}_W^{\mathrm{IBA}}$ is obtained from a fit to both the leptonic asymmetry and cross section measurements, but is determined mainly by the value of $\Gamma_{l^+l^-}$.

The improved Born approximation definition of $\sin^2\bar{\theta}_{\rm W}^{\rm IBA}$ differs slightly from the exact definition of $\sin^2\bar{\theta}_{\rm W}$. The difference between the two may be as large as 0.002 and depends on the values of $M_{\rm t}$ and $M_{\rm H}$. This comparison illustrates the point that, at the present level of experimental precision, care must be taken as to the exact definition used in extracting the parameter $\sin^2\bar{\theta}_{\rm W}$ when quoting the value obtained.

In Figure 19 the shaded area shows the Standard Model expectations corresponding to various choices of $M_{\rm t}$ and $M_{\rm H}$. Also indicated as an error bar is our result for $\sin^2\bar{\theta}_{\rm W}^{\rm IBA}$, calculated using relation (2).

6.5.3 Analysis of the Z^0 invisible width

The combination of hadronic and leptonic cross sections allows a model independent determination of the partial decay width of the Z^0 into invisible final states. The value derived from our data for the invisible width of the Z^0 is:

$$\Gamma_{\rm inv} \equiv \Gamma_{\rm Z} - \Gamma_{\rm had} - 3\Gamma_{l^+l^-} = 504 \pm 15 \text{ MeV}$$

Under the assumption that the only invisible decay modes of the Z^0 are to light neutrinos, and assuming the Standard Model value of:

$$\Gamma_\nu^{\rm SM} = 166.8 \pm 1.5 \text{ MeV } (M_{\rm t}, M_{\rm H})$$

for the partial decay width into a single light neutrino species, the number of light neutrino species is:

$$N_\nu \equiv \Gamma_{\rm inv}/\Gamma_\nu^{\rm SM} = 3.02 \pm 0.09(\text{exp}) \pm 0.03 \ (M_{\rm t}, M_{\rm H})$$

The Standard Model prediction for the ratio of partial decay widths of the Z^0 is less sensitive to the unknown top quark and Higgs masses than are the predictions for the partial widths themselves. The Standard Model value for the ratio of the partial widths of neutrinos and charged leptons is:

$$\left(\frac{\Gamma_\nu}{\Gamma_{l^+l^-}}\right)^{\rm (SM)} = 1.992 \pm 0.003 \ (M_{\rm t}, M_{\rm H})$$

A fit to our line-shape data results in:

$$\frac{\Gamma_{\rm inv}}{\Gamma_{l^+l^-}} = 6.07 \pm 0.17$$

The number of neutrinos can be extracted from this measurement as:

$$N_\nu \equiv \frac{\Gamma_{\rm inv}}{\Gamma_{l^+l^-}} \cdot \left(\frac{\Gamma_{l^+l^-}}{\Gamma_\nu}\right)^{\rm (SM)} = 3.05 \pm 0.09(\text{exp}) \pm 0.005 \ (M_{\rm t}, M_{\rm H})$$

in excellent agreement with the determination of N_ν discussed above. Note that not only are the theoretical assumptions in these two methods different, but also the experimental uncertainties contribute differently in the two cases.

Being insensitive to many virtual corrections, the ratio $\Gamma_{\rm inv}/\Gamma_{l^+l^-}$ is also a good quantity from which to derive limits on any new particles contributing to the invisible width. Our measurement places an upper limit of:

$$\frac{\Gamma_{\rm inv}}{\Gamma_{l^+l^-}} < 6.35$$

at the 95% confidence level. The lowest value allowed by the Standard Model, with three light neutrino families, for the ratio $\Gamma_{\rm inv}/\Gamma_{l^+l^-}$ is 5.966. With this assumption our measurement results in an upper limit of $\Gamma_{\nu'}/\Gamma_{l^+l^-} < 0.38$ at 95% confidence level, where $\Gamma_{\nu'}$ is the partial decay width to a new light invisible object.

We may also place mass limits on a stable heavy fourth generation neutrino, with Standard Model couplings. The partial decay width to a heavy neutrino is affected by the kinematic suppression factor:

$$\delta(M_\nu) = \left(1 - 4\frac{M_\nu^2}{s}\right)^{1/2}\left(1 - \frac{{M_\nu}^2}{s}\right)$$

Therefore the presence of a heavy neutrino would not only increase the invisible width, but would also distort the line shape. We express the ratio of the invisible to the charged leptonic width as

$$\Gamma_{\rm inv}/\Gamma_{l^+l^-} = (1 + \delta(M_\nu)/3)\cdot 5.966$$

and parametrise the total decay width, in the presence of a heavy neutrino, as $\Gamma_Z = \Gamma_{\rm had} + 3\Gamma_{l^+l^-} + \Gamma_{l^+l^-}(\Gamma_{\rm inv}/\Gamma_{l^+l^-})$. We then perform the model independent fit discussed in section 6.5.1 treating M_ν as a free parameter. The χ^2 for this fit is minimised for $M_\nu = 45.5$ GeV, where it takes on the value of 60.1, similar to the χ^2 value of the canonical model independent fit. This fit places a lower limit of

$$M_\nu > 44.1 \text{ GeV}$$

at the 95% confidence level. A similar analysis was performed to place limits on a stable massive scalar neutrino, with the couplings specified by the Minimal Supersymmetric extension of the Standard Model. In this case the suppression factor is:

$$\delta(M_{\tilde\nu}) = \frac{1}{2}\left(1 - 4\frac{M_{\tilde\nu}^2}{s}\right)^{3/2}$$

and the resulting limit is:

$$M_{\tilde\nu} > 31.2 \text{ GeV}$$

at the 95% confidence level. The same kinematic suppression factor also applies to the case of a stable Majorana neutrino. The coupling to the Majorana neutrino is, however, twice that to the scalar neutrino so that the corresponding mass limit is:

$$M_\nu(\text{Majorana}) > 37.2 \text{ GeV}$$

at the 95% confidence level.

6.5.4 Standard Model Fits and Limits on the Top Quark Mass

As discussed above, the Standard Model predictions for the parameters we have measured have a range of uncertainty due to the unknown top quark and Higgs masses. Since our data are well accommodated within the range of the Standard Model predictions, they may be used to constrain the top quark mass. We use the full one-loop Standard Model calculation, with leading $O(\alpha^2 M_t^4)$ terms, provided in the program ZFITTER. This calculation is performed within the framework of a minimal Higgs sector, that is assuming $\rho_{tree} = 1$. Input parameters to this calculation, in addition to the values of α and G_F, are M_Z, M_t, M_H and the strong coupling constant α_s, or $\Lambda_{\overline{MS}}$. The top quark mass and QCD corrections are highly correlated in this procedure. We therefore have implemented a precise parametrisation of QCD corrections for the partial widths, described in [29], and have included the QCD corrections to electroweak loops [30].

All fits are repeated for four different Higgs mass values spanning the interval $50 < M_H < 1000$ GeV. In quoting a χ^2 and results for the top quark mass we refer to the values obtained for the fit with $M_H = 300$ GeV; the observed changes in the mean value obtained for the four fits are used to derive the uncertainty due to the unknown value of M_H.

In the first instance we constrain the value of α_s as determined by the OPAL collaboration from a study of jet production rates in hadronic Z^0 decays [28] to be $\alpha_s = 0.118 \pm 0.008$. Figure 20 (a) shows the resulting χ^2 curves for fits to the OPAL measurements of the hadronic and leptonic line shapes and the leptonic forward-backward asymmetries (the parameters M_Z and α_s are varied to minimise the χ^2 at each point on the curves shown). The results obtained from this set of fits are listed in column 2 of Table 18. The envelope of the four curves allows an upper limit to be placed on the top quark mass at:

$$M_t < 218 \text{ GeV at 95\% confidence level.}$$

Note that using the χ^2 envelope of the four fits in setting an upper limit amounts to adding the uncertainty due to the unknown Higgs mass linearly with the experimental uncertainties.

Using the values of M_Z and M_t obtained from these fits we can, within the framework of the Standard Model, extract the predicted values for other electroweak parameters (and their uncertainties). Of particular interest are the mass of the $W^\pm$ boson, M_W, the weak mixing angle $\sin^2\theta_W \equiv 1 - \frac{M_W^2}{M_Z^2}$, the effective weak mixing angle $\sin^2\bar{\theta}_W^{SM}(\text{lept})$ for leptons and the effective weak mixing angle $\sin^2\bar{\theta}_W^{SM}(b)$ for b quarks [2]. The results are shown in column 2 of Table 19; the χ^2 curves for each parameter are shown in Figure 21.

[2] Here we adopt the definition $\sin^2\bar{\theta}_W^{SM}(f) \equiv (1 - \frac{M_W^2}{M_Z^2}) Re[\kappa_f(M_Z^2)]$ where $\kappa_f(M_Z^2)$ is the form factor defined in [24].

Our determination of $\sin^2\theta_W \equiv 1 - \frac{M_W^2}{M_Z^2}$ can be compared with the mean value resulting from deep inelastic neutrino scattering experiments, derived assuming $M_t = M_H = 100$ GeV [33,34]: $\sin^2\theta_W = 0.230 \pm 0.004(\text{stat.}) \pm 0.005(\text{syst.})$. There is good agreement. The CHARM-II Collaboration has recently reported [34] an improved determination of the effective electroweak mixing angle from the ratio of $\nu_\mu e$ to $\overline{\nu}_\mu e$ scattering cross sections. They measured $\sin^2\theta_W^\circ = 0.239 \pm 0.009(\text{stat.}) \pm 0.007(\text{syst.})$. They state that their definition of $\sin^2\theta_W^\circ$ coincides to within 0.001 with that of $\sin^2\overline{\theta}_W^{SM}(\text{lept})$, independent of M_t and M_H [34]. Our value for $\sin^2\overline{\theta}_W^{SM}(\text{lept})$ is consistent with and more precise than the value of $\sin^2\theta_W^\circ$ of CHARM-II. The value we have determined for $\sin^2\overline{\theta}_W^{SM}(b)$ agrees with the less precise direct measurements of this quantity from the forward-backward asymmetry of bottom quark-antiquark pairs in Z^0 decays [35].

The value of $M_W = 79.93 \pm 0.36$ GeV obtained from the Standard Model fits to our data is also in excellent agreement with the direct measurements of the ratio $M_W/M_Z = 0.8831 \pm 0.0048(\text{stat}) \pm 0.0026(\text{syst})$ and $M_W = 79.91 \pm 0.39$ GeV from the UA2 and CDF experiments respectively [31,32], and of a similar precision. This is an important further test of the Standard Model.

Having established the consistency of our data and the direct measurements of M_W with the Standard Model prediction, we proceed to combine them in order to extract more precise predictions for the top quark mass. In Figure 20(b) are shown the χ^2 curves derived from the combination of the OPAL value of M_Z with the measurements of M_W/M_Z and M_W from UA2 and CDF. These distributions show a similar sensitivity to the top quark mass as the OPAL line-shape and forward-backward asymmetry measurements alone. The results of this set of fits are listed in column 3 of Table 18.

In Figure 20(c) are shown the χ^2 contours resulting from combining the full set of OPAL's line-shape and forward-backward asymmetry measurements with the ratio M_W/M_Z from UA2 and M_W from CDF. These show a further enhanced sensitivity to the top quark mass. The results are shown in column 4 of Table 18. The envelope of these curves results in a top quark mass limit of:

$$M_t < 207 \text{ GeV at } 95\% \text{ confidence level.}$$

The results obtained from parameter transformations to other electroweak parameters for this set of fits are shown in column 3 of Table 19. The corresponding χ^2 curves for each parameter are shown in Figure 22.

A further set of fits to the combination of OPAL data and the measured values of M_W and M_W/M_Z has been carried out in which we allowed $\Lambda_{\overline{MS}}$ to vary freely, with no external constraint. The results of this set of fits are listed in column 2 of Table 20. Figure 23 shows the χ^2 contour in the M_t versus $\Lambda_{\overline{MS}}$ plane, for the fit assuming $M_H = 300$ GeV. This can be compared with the result of a similar calculation using only R_Z as input shown in column 3 of Table 20. In both cases the value of α_s obtained from these fits is somewhat higher, but consistent with, the value derived from the jet rate measurement of α_s. The central value of the top quark mass derived from the fit with α_s unconstrained is correspondingly reduced.

7 Summary

Using the data recorded by the OPAL detector during 1989 and 1990 the Z^0 parameters have been measured with high precision, through an analysis of the reactions $e^+e^- \to$ hadrons, $e^+e^- \to e^+e^-$, $e^+e^- \to \mu^+\mu^-$ and $e^+e^- \to \tau^+\tau^-$ at several centre of mass energies around the Z^0 mass.

We obtain from a combined fit to hadrons and leptons a mass of $M_Z = 91.161 \pm 0.009 \pm 0.02$ GeV, and a total width of $\Gamma_Z = 2.492 \pm 0.016$ GeV. The errors on M_Z have been separated into the experimental error and the uncertainty due to the LEP beam energy. The error on Γ_Z includes a contribution of 5 MeV due to the beam energy uncertainty. The measured charged leptonic partial widths are $\Gamma_{ee} = 82.9 \pm 1.0$ MeV, $\Gamma_{\mu\mu} = 83.2 \pm 1.5$ MeV, and $\Gamma_{\tau\tau} = 82.7 \pm 1.9$ MeV, consistent with lepton universality. From a fit assuming lepton universality we obtain $\Gamma_{l^+l^-} = 83.00 \pm 0.69$ MeV. The hadronic partial width is $\Gamma_{\rm had} = 1739 \pm 17$ MeV. The ratio of the hadronic to the leptonic partial width of the Z^0 is measured as $R_Z = 20.95 \pm 0.22$. From the measured total and visible partial widths a model independent value for the invisible width is calculated to be $\Gamma_{\rm inv} = 504 \pm 15$ MeV, corresponding to $N_\nu = 3.02 \pm 0.09 \pm 0.03$. Alternatively we obtain for the ratio of the invisible width to the charged leptonic partial width $\Gamma_{\rm inv}/\Gamma_{l^+l^-} = 6.07 \pm 0.17$, which corresponds to $N_\nu = 3.05 \pm 0.09 \pm 0.005$.

The couplings of the Z^0 to charged leptons are studied using measurements of the lepton pair cross sections and forward-backward asymmetries at the different centre of mass energy points of the Z^0 scan. Using a generalisation of the improved Born approximation for the lepton pair differential cross section, the square of the product of the effective axial vector and vector coupling constants of the Z^0 to charged leptons, determined mainly from the forward-backward asymmetries at the peak, is found to be $\kappa^a_{ZZ}\hat{a}_l^2\hat{v}_l^2 = 0.0017 \pm 0.0028$. Within this parametrisation the energy dependence of the forward-backward asymmetries provides an independent measure of the axial vector coupling constant, which is determined to be $\kappa^a_{\gamma Z}\hat{a}_l^2 = 0.89 \pm 0.11$. A parametrisation in the form of the improved Born approximation gives effective leptonic axial vector and vector coupling constants $\hat{a}_l^2 = 0.998 \pm 0.009$ and $\hat{v}_l^2 = 0.0023 \pm 0.0028$. Alternatively, these results may be re-expressed as: $\rho_Z = 0.998 \pm 0.009$ and $\sin^2\overline{\theta}_{\rm W} = 0.238^{+0.03}_{-0.006}$ respectively. Using an approximate minimal Standard Model relationship between ρ_Z and $\sin^2\overline{\theta}_{\rm W}$, the result $\sin^2\overline{\theta}^{\rm IBA}_{\rm W} = 0.2337 \pm 0.0021$ is obtained. The final results for M_Z, Γ_Z, $\sigma^{\rm pole}_{\rm had}$, partial decay widths and coupling constants are summarised in Tables 15 and 17 and Figures 15 to 19.

These data are in excellent agreement with the Standard Model, within the range of uncertainty introduced by the unknown top quark and Higgs masses, and with similar results reported by other collaborations at LEP and SLC [36]. The measurements presented here are sufficiently precise to be sensitive to the virtual radiative corrections, predicted by the Standard Model, due to the top quark and Higgs scalar.

Fits to our data using a full one loop Standard Model calculation, incorporating QCD corrections to both the hadronic decays and electroweak loops, are used to constrain the top quark mass. We find that a top quark mass greater than 218 GeV is ruled out at the 95% confidence level. From Standard Model fits to our data we obtain a value for the effective weak mixing angle in the charged lepton sector of $\sin^2\overline{\theta}^{\rm SM}_{\rm W}({\rm lept}) = 0.2341 \pm 0.0021$. The value of $M_{\rm W}$ resulting from the Standard Model fits, $M_{\rm W} = 79.93 \pm 0.36$ GeV, is in good agreement with the direct measurements of $M_{\rm W}/M_Z$ and $M_{\rm W}$ from the UA2 [31] and CDF [32] experiments. This is an important further test of the Standard Model. Combining our data with the measurements of $M_{\rm W}$ and $M_{\rm W}/M_Z$ results in a further enhanced sensitivity to the top quark mass. We find that, in the context of the Standard Model, a top quark mass greater than 207 GeV is ruled out at the 95% confidence level. From a similar fit, but leaving α_s unconstrained, we obtain $\alpha_s = 0.141^{+0.022}_{-0.020}$. From a fit using only the measured values of M_Z and R_Z as input we obtain $\alpha_s = 0.147^{+0.032}_{-0.029}$. These values are consistent with the value of $\alpha_s = 0.118 \pm 0.008$ extracted from measurements of jet rates [28].

Acknowledgements:

It is a pleasure to thank the SL Division for the efficient operation of the LEP accelerator, the precise information on the absolute energy, and their continuing close cooperation with our experimental group.

We are grateful to D. Bardin,W. Beenakker, F.A. Berends, M. Bilenky, S. Jadach, R. Kleiss, J.H. Kühn, S.C. van der Marck, T. Riemann, M. Sachwitz and Z. Wąs for their help and advice concerning the programs and the analytic formulae used in this analysis. We thank Erik Jagel for providing a convenient computing environment to perform the fits for the electroweak parameters.

In addition to the support staff at our own institutions we are pleased to acknowledge the following :
Department of Energy, USA
National Science Foundation, USA
Science and Engineering Research Council, UK
Natural Sciences and Engineering Research Council,Canada
Israeli Ministry of Science
Minerva Gesellschaft
The Japanese Ministry of Education, Science and Culture (the Monbusho) and a grant under the Monbusho International Science Research Program.
American Israeli Bi-national Science Foundation.
Direction des Sciences de la Matière du Commissariat à l'Energie Atomique, France.
The Bundesministerium für Forschung und Technologie, FRG.
and The A.P. Sloan Foundation.

Figure Captions

Figure 1: Luminosity analysis:
A schematic illustration of the OPAL forward detectors. The scale marked along the beam axis indicates the distance from the interaction point in millimeters.

Figure 2: Luminosity analysis:
A correlation plot showing the normalised cluster energy in the right and left calorimeters for a sample of events passing all method I cuts except for the total cluster energy cut (indicated by the diagonal line). The approximate trigger thresholds are shown as the hatched region. The off-momentum beam particle background events are clearly separated with low calorimeter energy on both sides. This plot represents approximately 11000 Bhabha events, corresponding to about 10% of the total sample.

Figure 3: Luminosity analysis:
The normalised cluster energy in the left and right calorimeters for method I events. The solid line shows the distribution for BABAMC Monte Carlo events with simple detector response functions applied.

Figure 4: Luminosity analysis:
The quantity $\Delta\phi$after all method I cuts except the acoplanarity cut, which is indicated by the arrows. The solid line shows the same distribution for Monte Carlo events subject to the same cut.

Figure 5: Luminosity analysis:
The distribution of electron and positron polar angles (θ), for events which pass the method I selection. The solid line is from Monte Carlo events for the same cuts. The arrows indicate the position of cuts made on the average angle between the two ends. The entries beyond these cuts are acolinear radiative events. The minimum and maximum angle cuts confine even the radiative events to well understood regions of the detector. The effect of the minimum and maximum angle cuts at each end is also visible.

Figure 6: Luminosity analysis:
Mapping the drift chamber survey onto the tube chambers. The drift time measured in a typical drift chamber vs. the coordinates measured in the tube chambers for a sample of clean single tracks. The lines are a best fit to the data with the assumption that drift time is linear with distance and that the drift velocity is the same on both sides of the sense wires. Points in the region of local field distortion near the sense wires were excluded from the fit. The inset is a schematic illustration of one of the planes of four drift chambers. The arrows indicate the drift directions towards the sense wires in each of the four chambers (including the Lorentz angle, which does not affect the analysis).

Figure 7: Luminosity analysis:
Image of the A counters projected onto the tube chambers. The polar angle distribution of the cluster in the tube chambers on the A counter side for events passing the fine luminosity scintillation counter selection (method II). The solid line is for the Monte Carlo simulation, which includes scattering and showering in upstream material.

Figure 8: Multihadron analysis:
Distributions of variables used for the multihadron event selection:
(a) R_{vis},
(b) Multiplicity of electromagnetic calorimeter clusters,
(c) Multiplicity of charged tracks,
(d) R_{bal}.
The variables are defined in Section 4. The histograms are the JETSET 7.2 + detector simulation expectations, the solid points are the measured distributions, after all cuts have been applied, other than on the quantity shown. The hatched histograms are the Monte Carlo expectation for the contribution from $e^+e^- \to \tau^+\tau^-$ events.

Figure 9: Multihadron analysis:
The $|\cos\theta_{Thrust}|$ distribution. A comparison between the JETSET 7.2 + detector simulation and the real data (at the peak) after all cuts is shown. This distribution is well reproduced all the way up to the edge of the acceptance.

Figure 10: $e^+e^- \to e^+e^-$ analysis:
Distribution of total electromagnetic calorimeter energy. The solid histogram is the Monte Carlo expectation for $e^+e^- \to e^+e^-$; the hatched histogram is the Monte Carlo expectation for the background contribution from $e^+e^- \to \tau^+\tau^-$. The double hatched histogram is the Monte Carlo expectation for hadronic background.

Figure 11: $e^+e^- \to e^+e^-$ analysis:
Comparison of measured distributions with ALIBABA predictions:
(a) angular distribution at Z^0 peak, requiring both the electron and positron clusters to be within $|\cos\theta| < 0.85$ and the acollinearity angle less than 10°
(b) acolinearity distribution at Z^0 peak, requiring both the electron and positron clusters to be within $|\cos\theta| < 0.70$
The points are the data unfolded for effects of resolution and backgrounds, the histogram is the result of the ALIBABA calculation.

Figure 12: $e^+e^- \to \mu^+\mu^-$ analysis:
(a) Distribution of scaled visible energy, F_{vis}, for Monte Carlo and data in the angular region $|\cos\theta| < 0.80$.
(b) Distribution of scaled visible energy, F_{vis}, for Monte Carlo and data in the angular region $0.80 < |\cos\theta| < 0.90$.
(c) Distribution of visible energy, F_{vis}, for Monte Carlo and data in the angular region $0.90 < |\cos\theta| < 0.95$.
The solid points are data, the solid histogram is the $e^+e^- \to \mu^+\mu^-$ Monte Carlo and the hatched histogram is the Monte Carlo expectation for the $e^+e^- \to \tau^+\tau^-$ contribution. The double hatched histogram is the contribution from hadronic background.

Figure 13: $e^+e^- \to \mu^+\mu^-$ analysis:
Distribution of the acoplanarity angle for Monte Carlo and data, for a sample of $\mu^+\mu^-$ candidate events enriched in $\tau^+\tau^-$ background (see text).
The solid points are data, the solid histogram is the $e^+e^- \to \mu^+\mu^-$ Monte Carlo and the hatched histogram is the Monte Carlo expectation for the $e^+e^- \to \tau^+\tau^-$ contribution.

Figure 14: $e^+e^- \to \tau^+\tau^-$ analysis:
Comparison with Monte Carlo :
a) number of tracks distribution,
b) sum of the number of tracks and the number of clusters distribution,
c) scaled shower energy distribution,
d) scaled visible energy distribution,
e) acolinearity angle distribution,
f) $|\cos\theta|$ distribution,
after the other cuts are made. Only the data collected at the peak energy was used for the comparison. The points are data, the solid histogram is the $e^+e^- \to \tau^+\tau^-$ Monte Carlo and the hatched histogram is the Monte Carlo expectation for the background contribution.

Figure 15: Confidence level contours for the measurement of Γ_Z and σ_{had}^{pole}.
The black parallelograms of bars indicate the Standard Model prediction for 3 and 4 light neutrino species. The range spanned by each parallelogram shows the variation in the Standard Model prediction for $50 < M_t < 230$ GeV, $50 < M_H < 1000$ GeV and $\alpha_s = 0.118 \pm 0.008$. The shaded bar linking the two parallelograms marks the expected modification introduced by an additional contribution to the invisible Z^0 decay width exclusively. The second, darker, shaded bar indicates the modification introduced by an additional contribution to the hadronic Z^0 decay width exclusively.

Figure 16: Cross sections as functions of centre of mass energy for:
a) $e^+e^- \to e^+e^-$, integrated over $|\cos\theta_{e^-}| < 0.7$ and corrected for efficiency within the geometrical acceptance;
b) $e^+e^- \to \mu^+\mu^-$, corrected for acceptance;
c) $e^+e^- \to \tau^+\tau^-$, corrected for acceptance;
d) $e^+e^- \to$ hadrons, corrected for acceptance.
The solid lines are the results of the fit to the combined e^+e^-, $\mu^+\mu^-$, $\tau^+\tau^-$ and hadronic data described in the text. The solid points show the 1990 data and the open points the 1989 data.

Figure 17: Forward-backward charge asymmetries for:
a) $e^+e^- \to e^+e^-$, within $|\cos\theta_{e^-}| < 0.7$;
b) $e^+e^- \to \mu^+\mu^-$, within $|\cos\theta| < 0.95$;
c) $e^+e^- \to \tau^+\tau^-$, within $|\cos\theta| < 0.90$.
The solid lines are the results of the fit to the combined e^+e^-, $\mu^+\mu^-$, $\tau^+\tau^-$ and hadronic data described in the text.

Figure 18: One and two standard deviation confidence level contours in the:
a) $\kappa^a_{ZZ}\hat{a}_l^2\hat{v}_l^2$ vs. $\kappa^a_{\gamma Z}\hat{a}_l^2$,
b) $\kappa^a_{ZZ}\hat{a}_l^2\hat{v}_l^2$ vs. $\Gamma_{l^+l^-}$ and
c) Γ_{had} vs. $\Gamma_{l^+l^-}$ planes.
The stars indicate our best fitted values. The shaded areas show the variation in the Standard Model prediction for $50 < M_t < 230$ GeV, $50 < M_H < 1000$ GeV and $\alpha_s = 0.118 \pm 0.008$.

Figure 19: One standard deviation confidence level contour in the ρ_Z vs. $\sin^2\bar{\theta}_W$ plane. The stars indicate our best fitted values for ρ_Z and $\sin^2\bar{\theta}_W$. There are two solutions, symmetric about $\sin^2\bar{\theta}_W = 0.25$. The error bar shows our one standard deviation limits on $\sin^2\bar{\theta}_W^{IBA}$ after applying the minimal Standard Model constraint (2) given in the text, at the corresponding value of ρ_Z. The shaded area shows the variation in the Standard Model prediction for ρ_Z vs $\sin^2\bar{\theta}_W^{SM}$ over the range of $50 < M_t < 230$ GeV, $50 < M_H < 1000$ GeV.

Figure 20: a) The χ^2 curves for the fit to M_t and $\Lambda_{\overline{MS}}$, using the OPAL cross section and forward-backward asymmetry measurements, for four different Higgs mass values spanning the interval $50 < M_H < 1000$ GeV. In these fits we constrain the strong coupling constant by $\alpha_s = 0.118 \pm 0.008$.
b) Similar contours are shown derived from the combination of the OPAL value of M_Z with the ratio M_W/M_Z from UA2 and M_W from CDF.
c) The χ^2 contours resulting from combining the full set of OPAL's cross section and forward-backward asymmetry measurements with the ratio M_W/M_Z from UA2 and M_W from CDF.

Figure 21: a) The χ^2 curves for the parameter M_W resulting from the fit to M_t and $\Lambda_{\overline{MS}}$, using the OPAL line-shape and forward-backward asymmetry data, for four different Higgs mass values spanning the interval $50 < M_H < 1000$ GeV. In these fits we constrain the strong coupling constant by $\alpha_s = 0.118 \pm 0.008$.
b) Similar χ^2 curves are shown for the parameter $\sin^2\theta_W \equiv 1 - \frac{M_W^2}{M_Z^2}$
c) Similar χ^2 curves are shown for the effective weak mixing angle $\sin^2\bar{\theta}_W^{SM}(\text{lept})$ for leptons.
d) Similar χ^2 curves are shown for the effective weak mixing angle $\sin^2\bar{\theta}_W^{SM}(b)$ for b quarks.

Figure 22: a) The χ^2 curves for the parameter M_W resulting from the fit to M_t and $\Lambda_{\overline{MS}}$, using the OPAL line-shape and forward-backward asymmetry data combined with the measurements of M_W/M_Z and M_W from the UA2 and CDF experiments, for four different Higgs mass values spanning the interval $50 < M_H < 1000$ GeV. In these fits we constrain the strong coupling constant by $\alpha_s = 0.118 \pm 0.008$.
b) Similar χ^2 curves are shown for the parameter $\sin^2\theta_W \equiv 1 - \frac{M_W^2}{M_Z^2}$
c) Similar χ^2 curves are shown for the effective weak mixing angle $\sin^2\bar{\theta}_W^{SM}(\text{lept})$ for leptons.
d) Similar χ^2 curves are shown for the effective weak mixing angle $\sin^2\bar{\theta}_W^{SM}(b)$ for b quarks.

Figure 23: The one standard deviation confidence level contour in the M_t versus $\Lambda_{\overline{MS}}$ plane, for a fit using the OPAL line-shape and forward-backward asymmetry data combined with the measured values of M_W and M_W/M_Z from the CDF and UA2 experiments. In this fit no external constraint is placed on $\Lambda_{\overline{MS}}$. The fit was carried out assuming $M_H = 300$ GeV. The horizontal band shows the $\pm$ one sigma region allowed by the determination of $\Lambda_{\overline{MS}}$ from the measured hadronic jet production rates in hadronic Z^0 decays [28].

References

[1] OPAL Collaboration, M.Z. Akrawy et al., Phys. Lett. **B240** (1990) 497.

[2] OPAL Collaboration, M.Z. Akrawy et al., Phys. Lett. **B247** (1990) 458.

[3] OPAL Collaboration, K. Ahmet et al., "The OPAL Detector at LEP", CERN-PPE/90-114 (August 1990), to be published by Nucl. Instr. and Meth.

[4] OPAL Collaboration, M. Arignon et al., "The Trigger System of the OPAL Experiment at LEP", CERN-PPE/91-32 (February 1991), submitted to Nucl. Instr. and Meth.

[5] J. Allison et al., Comp. Phys. Comm. 47 (1987) 55;
R. Brun et al., GEANT 3, Report DD/EE/84-1, CERN (1989).

[6] D.C. Imrie el al., Nucl. Instr. and Meth. **A283** (1989) 515.

[7] B.E. Anderson et al., Nucl. Instr. and Meth. **A283** (1989) 650.

[8] M. Böhm, A. Denner and W. Hollik, Nucl. Phys. **B304** (1988) 687;
F.A. Berends, R. Kleiss, W. Hollik, Nucl. Phys. **B304** (1988) 712.

[9] S. Jadach et al., Phys. Lett. **B253** (1991) 469.

[10] S. Jadach et al., "Higher order QED corrections to Bhabha scattering at low angles", CERN-TH.5995/91 (February 1991).

[11] H. Burkhardt et al., Z. Phys. **C43** (1989) 497.

[12] W.Beenakker, F.A.Berends and S.C.Van der Marck,
"Small Angle Bhabha Scattering",
Instituut Lorentz, Univ. of Leiden preprint, November 13,1990.

[13] T. Sjöstrand, Comp. Phys. Comm. 39 (1986) 347; JETSET, Version 7.2.

[14] OPAL Collaboration, M.Z. Akrawy et al., Z. Phys. **C47** (1990) 505.

[15] OPAL Collaboration, M.Z. Akrawy et al., Phys. Lett. **B231** (1989) 530.

[16] S. Jadach et al., Z Physics at LEP1, CERN 89-08, ed. G. Altarelli et al., Vol 1 (1989) 235; KORALZ, Version 3.7.

[17] G. Marchesini and B.R. Webber, Nucl. Phys. **B310** (1988) 461; HERWIG.

[18] R. Bhattacharya, J. Smith, G. Grammer, Phys. Rev. **D15** (1977) 3267;
J. Smith, J.A.M. Vermaseren, G. Grammer, Phys. Rev. **D15** (1977) 3280.

[19] OPAL Collaboration, M.Z. Akrawy et al., Phys.Lett. B257 (1991) 531.

[20] Bhabha line shape program ALIBABA, W.J.P. Beenakker, F.A. Berends and S.C.Van der Marck
W. Beenakker et al., Nucl. Phys. **B349** (1991) 323.

[21] R. Bailey et al., "LEP Energy Calibration", CERN-SL/90-95 (August 1990), contribution to the 2nd European Particle Accelerator Conference, Nice, France, June 12-16, 1990.

[22] Working Group on LEP Absolute Energy, V. Hatton et al., "LEP Absolute Energy in 1990", LEP Performance Note 12 (December 1990), unpublished;
A. Hofmann, private communication.

[23] M. Consoli and W. Hollik, Z Physics at LEP1, CERN 89-08, ed. G. Altarelli et al., Vol 1 (1989) 7.

[24] Line shape program ZFITTER, Dubna-Zeuthen radiative correction group, D. Bardin et al. (based on the ZBIZON package);
D. Bardin et al., Comp. Phys. Comm. **59** (1990) 303;
D. Bardin et al., Z. Phys. **C44** (1989) 493;
D. Bardin et al., Nucl. Phys. **B351** (1991) 1;
D. Bardin et al., Phys. Lett. **B229** (1989) 405.

[25] Line shape program ZBIZON, Dubna-Zeuthen radiative correction group, D. Bardin et al.;
R. Kleiss et al., Z Physics at LEP1, CERN 89-08, ed. G. Altarelli et al., Vol 3 (1989) 60.

[26] Line shape program ZSHAPE, W.J.P. Beenakker, F.A. Berends and S.C. van der Marck
R. Kleiss et al., Z Physics at LEP1, CERN 89-08, ed. G. Altarelli et al., Vol 3 (1989) 50.

[27] F. Aversa and M. Greco, Phys. Lett. **B228** (1989) 134;
F. Aversa et al., Phys. Lett. **B247** (1990) 93;
M. Greco, private communication.

[28] OPAL Collaboration, M.Z. Akrawy et al., Z. Phys. **C49** (1991) 375.

[29] K.G. Chetyrkin and J.H. Kühn, Phys. Lett. **B248** (1990) 359.

[30] A. Djouadi and C. Verzegnassi, Phys. Lett. **B195** (1987) 265;
A. Djouadi, Nuovo Cimento **A100** (1988) 357;
D. Bardin and A. Chizhov, JINR Dubna report E2-89-525 (1989) 42.

[31] UA2 Collaboration, J. Alitti et al., Phys. Lett. **B241** (1990) 150.

[32] CDF Collaboration, F. Abe et al., Phys. Rev. Lett. **65** (1990) 2243.

[33] A. Blondel et al., Z. Phys. **C45** (1990) 361;
CHARM Collaboration, J.V. Allaby et al., Z. Phys. **C36** (1987) 611.

[34] CHARM-II Collaboration, D. Geiregat et al., CERN-PPE/91-15 (January 1991).

[35] L3 Collaboration, B. Adeva et al., Phys. Lett. **B252** (1990) 713;
OPAL Collaboration, M.Z. Akrawy et al., CERN-PPE/91-48 (March 1991), submitted to Phys. Lett.

[36] Mark II Collaboration, G.S. Abrams et al., Phys. Rev. Lett. **63** (1989) 2173;
Mark II Collaboration, G.S. Abrams et al., Phys. Rev. Lett. **63** (1989) 2780;
ALEPH Collaboration, D. Decamp et al., Z. Phys. **C48** (1990) 365;
DELPHI Collaboration, P. Abreu et al., CERN-PPE/90-119 (August 1990), contribution to the 25th International Conference on High Energy Physics, Singapore, August 1990;
DELPHI Collaboration, P. Abreu et al., CERN-PPE/91-43 (March 1991);
L3 Collaboration, B. Adeva et al., L3 Preprint #28 (February 1991).

Source of Error	Uncertainty [%]
Inhomogeneity in tube chambers	0.5
Pitch of tubes	0.4
Survey (with drift chambers)	0.3
Calorimeter coordinates	0.1
Distance to interaction point	0.1
Trigger efficiency	<0.1
Tube chamber efficiency	<0.1
Data statistics	0.3
Monte Carlo statistics	0.2
overall	**0.8**

Table 1: Summary of experimental uncertainties in the tube chamber, calorimeter, and drift chamber (Method I) absolute luminosity analysis.

	Correction Factor	Uncertainty [%]
Scattering in beampipe	0.981	1.0
Counter hits from accompanying particles	0.984	0.9
Counter edge simulation	1.000	0.5
Simulation of hard radiative Bhabhas	1.000	<0.3
Survey	1.000	0.2
Distance to interaction point	1.000	0.1
Counter efficiency	1.000	<0.1
Data statistics	1.000	0.4
Monte Carlo statistics	1.000	0.2
overall	0.965	**1.5**

Table 2: Summary of correction factors and experimental uncertainties in the fine luminosity scintillation counter (Method II) absolute luminosity analysis.

	Correction Factor	Uncertainty [%]
Acceptance/Efficiency:		
Monte Carlo, detector simulation	1.016	0.2
$\sqrt{s}$ dependence of acceptance	1.000	<0.1
Overall Acceptance/Efficiency	1.016	0.2
Background:		
$e^+e^- \to \tau^+\tau^-$	0.999	<0.1
two-photon reactions (0.02 ± 0.01 nb)	0.999	<0.1
beam-gas and beam-wall interactions	1.000	<<0.1
cosmic ray events	1.000	<<0.1
Total Backgrounds	0.998	0.1
Theoretical error:		
Fragmentation	1.000	0.3
overall	**1.014**	**0.4**

Table 3: Summary of the correction factors and systematic errors for the hadronic event selection and acceptance. There is an additional point to point systematic uncertainty of $0.2\% \cdot |\Delta E|/3$, where ΔE is the difference in energy, in GeV, from the point at the peak of the Z^0 resonance.

	Correction Factor	Uncertainty [%]
Acceptance/Efficiency:		
edge of acceptance	1.000	0.6
total energy cut	1.003	0.2
cluster energy cut	1.001	0.1
low energy tracks	1.002	0.1
tracking losses	1.001	0.1
trigger efficiency	1.000	<0.1
Overall Acceptance/Efficiency	1.007	0.7
Background:		
$e^+e^- \to \tau^+\tau^-$	0.998	0.1
multihadrons	1.000	<0.1
$e^+e^- \to \gamma\gamma$	1.000	<0.1
$e^+e^- \to e^+e^-e^+e^-$	1.000	<0.1
Total Backgrounds	0.998	0.1
overall	**1.005**	**0.7**

Table 4: Summary of the correction factors and systematic errors for the $e^+e^- \to e^+e^-$ event selection and acceptance. Correction factors refer to the acceptance within $|\cos\theta_{e^-}| < 0.7$ and acolinearity less than 10°.

	Correction Factor	Uncertainty [%]
Acceptance/Efficiency:		
tracking losses	1.006	0.3
$e^+e^- \to \mu^+\mu^-$ Monte Carlo	1.092	0.2
muon identification	1.001	0.1
F_{vis} resolution for $\lvert\cos\theta\rvert > 0.9$	0.999	0.1
trigger efficiency	1.001	0.1
cosmic ray rejection using TOF	1.000	<0.1
edge of acceptance (defined by the muon endcap detectors)	1.000	<0.1
Overall Acceptance/Efficiency	1.100	0.4
Background:		
$e^+e^- \to \tau^+\tau^-$	0.987	0.3
cosmic rays in the endcap	0.999	0.1
$e^+e^- \to e^+e^-\mu^+\mu^-$	1.000	0.0
Total Backgrounds	0.986	0.3
overall	**1.084**	**0.5**

Table 5: Summary of the correction factors and systematic errors for the $e^+e^- \to \mu^+\mu^-$ event selection and acceptance.

	Correction Factor	Uncertainty [%]
Acceptance/Efficiency:		
τ-pair selection cuts	1.000	0.8
definition of $\lvert\cos\theta\rvert$	1.000	0.6
$e^+e^- \to \tau^+\tau^-$ Monte Carlo	1.300	0.3
vertex cut	1.000	0.1
time-of-flight efficiency	1.000	0.1
trigger efficiency	1.001	0.1
Overall Acceptance/Efficiency	1.301	1.1
Background:		
Multihadrons	0.996	0.4
two-photon reactions (5.2±4.3 pb)	0.995	0.4
$e^+e^- \to e^+e^-$	0.997	0.3
$e^+e^- \to \mu^+\mu^-$	0.994	0.2
cosmic rays and beam-gas events	0.998	0.1
Total Backgrounds	0.980	0.7
overall	**1.276**	**1.3**

Table 6: Summary of the correction factors and systematic errors for the $e^+e^- \to \tau^+\tau^-$ event selection and acceptance. Not included is the correction for the energy dependence of the acceptance, due mainly to the acollinearity requirement.

$\sqrt{s}$ (GeV)	Luminosity (nb^{-1})	N_{had}	σ_{had} (nb)	$\sqrt{s}$ (GeV)	Luminosity (nb^{-1})	N_{had}	σ_{had} (nb)
		1989				1990	
88.278	115.1±1.6	569	5.04 ± 0.23	88.224	485.9±3.2	2229	4.63 ± 0.11
89.283	80.7±1.4	766	9.68 ± 0.40	89.226	639.2±3.7	5322	8.43 ± 0.13
90.284	103.7±1.6	1990	19.56 ± 0.56	90.226	381.3±2.9	7045	18.74 ± 0.28
91.034	210.9±2.3	6192	29.94 ± 0.58				
91.289	186.2±2.1	5633	30.86 ± 0.62	91.223	3483.8±8.9	103664	30.19 ± 0.13
91.529	230.8±2.4	6612	29.21 ± 0.55				
92.282	85.5±1.5	1781	21.24 ± 0.66	92.215	497.6±3.4	10412	21.22 ± 0.27
92.562	9.2±0.5	150	16.66 ± 1.62				
93.286	111.4±1.7	1286	11.77 ± 0.39	93.220	563.1±3.7	6848	12.33 ± 0.18
94.277	95.4±1.6	710	7.59 ± 0.32	94.219	562.1±3.7	4373	7.88 ± 0.13
95.036	17.7±0.7	112	6.44 ± 0.66				
Total	1246.6	25801			6613.5	139893	

Table 7: The hadronic cross section, σ_{had}, from a total of 165,694 hadronic decays, as a function of the luminosity-weighted centre-of-mass energy, $\sqrt{s}$. Listed are also the integrated luminosity and the number of observed hadronic events N_{had}. The cross sections are quoted with their statistical and point-to-point systematic uncertainty of both the multihadron acceptance and the luminosity calculation. For the 1990 measurements the overall systematic error on the cross section is 0.9%. The overall systematic error on the cross section for the 1989 measurements is 2.3%. The energy scale error is discussed in the text. The point-to-point error on the energy is 10 MeV.

$\sqrt{s}$ (GeV)	Luminosity (nb^{-1})	N_{ee}	σ_{ee} (nb)	$\sqrt{s}$ (GeV)	Luminosity (nb^{-1})	N_{ee}	σ_{ee} (nb)
		1989				1990	
88.277	119.4±1.4	31	0.262 ± 0.048	88.224	486.6±3.2	169	0.349 ± 0.028
89.286	40.1±1.0	15	0.377 ± 0.098	89.226	638.9±3.7	306	0.481 ± 0.028
90.282	105.2±1.6	73	0.701 ± 0.085	90.226	399.7±2.9	320	0.804 ± 0.045
91.030	170.4±2.0	147	0.871 ± 0.073				
91.286	211.2±2.3	215	1.029 ± 0.072	91.221	3363.6±8.7	3363	1.004 ± 0.018
91.527	170.8±2.1	161	0.952 ± 0.079				
92.283	78.4±1.4	44	0.566 ± 0.089	92.215	456.6±3.3	271	0.596 ± 0.037
93.284	86.8±1.5	35	0.406 ± 0.070	93.220	563.2±3.6	203	0.362 ± 0.026
94.277	77.0±1.4	26	0.340 ± 0.068	94.219	562.1±3.7	128	0.229± 0.021
Total	1059.3	747			6470.8	4760	

Table 8: The cross section for $e^+e^- \to e^+e^-$, from a total of 5507 events. σ_{ee} is the cross section measured within the angular acceptance $|\cos\theta_{e^-}| < 0.7$ and the acollinearity angle less than 10°, corrected for the effects of efficiency. The cross sections are quoted with their statistical and point-to-point systematic uncertainty of both the $e^+e^- \to e^+e^-$ acceptance and the luminosity calculation. For the 1990 measurements the overall systematic error on the cross section is 1.1%. The overall systematic error on the cross section for the 1989 measurements is 2.4%.

$\sqrt{s}$ (GeV)	Luminosity (nb^{-1})	$N_{\mu\mu}$	$\sigma^{tot}_{\mu\mu}$ (nb)	$\sqrt{s}$ (GeV)	Luminosity (nb^{-1})	$N_{\mu\mu}$	$\sigma^{tot}_{\mu\mu}$ (nb)
		1989				1990	
88.280	113.6 ± 1.6	24	0.283 ± 0.058	88.223	485.5 ± 3.2	109	0.243 ± 0.024
89.280	41.7 ± 1.0	11	0.352 ± 0.106	89.227	604.5 ± 3.6	231	0.414 ± 0.028
90.279	78.7 ± 1.4	53	0.889 ± 0.123	90.226	409.6 ± 3.0	316	0.836 ± 0.047
91.034	157.9 ± 2.0	148	1.238 ± 0.102				
91.281	160.5 ± 2.0	179	1.467 ± 0.110	91.222	3563.1 ± 9.0	4834	1.471 ± 0.022
91.530	190.8 ± 2.2	198	1.366 ± 0.098				
92.281	53.7 ± 1.2	40	0.988 ± 0.157	92.216	530.9 ± 3.5	527	1.075 ± 0.047
93.279	85.4 ± 1.5	35	0.549 ± 0.093	93.220	565.6 ± 3.7	308	0.591 ± 0.034
94.282	79.2 ± 1.4	25	0.422 ± 0.085	94.219	555.5 ± 3.7	202	0.394 ± 0.028
Total	961.5	713			6714.9	6527	

Table 9: The cross section for $e^+e^- \to \mu^+\mu^-$, from a total of 7240 events. $\sigma^{tot}_{\mu\mu}$ is the total cross section after correction for efficiency and acceptance. The cross sections are quoted with their statistical errors and the point-to-point systematic uncertainty of the luminosity calculation. For the 1990 measurements the overall systematic error on the cross section is 0.9%. The overall systematic error on the cross section for the 1989 measurements is 3.2%.

$\sqrt{s}$ (GeV)	Luminosity (nb^{-1})	$N_{\tau\tau}$	$\sigma^{tot}_{\tau\tau}$ (nb)	$\sqrt{s}$ (GeV)	Luminosity (nb^{-1})	$N_{\tau\tau}$	$\sigma^{tot}_{\tau\tau}$ (nb)
		1989				1990	
88.279	110.9 ± 1.6	20	0.262 ± 0.059	88.224	481.4 ± 3.2	81	0.213 ± 0.024
89.285	56.1 ± 1.2	14	0.360 ± 0.096	89.226	638.9 ± 3.7	214	0.426 ± 0.029
90.283	92.9 ± 1.5	56	0.864 ± 0.116	90.228	305.1 ± 2.6	221	0.924 ± 0.062
91.033	174.6 ± 2.1	180	1.471 ± 0.111				
91.287	157.7 ± 2.0	151	1.367 ± 0.112	91.222	3151.3 ± 8.4	3563	1.443 ± 0.024
91.530	178.4 ± 2.1	181	1.448 ± 0.109				
92.286	56.3 ± 1.2	34	0.864 ± 0.149	92.215	456.0 ± 3.3	364	1.019 ± 0.054
93.286	99.2 ± 1.6	41	0.593 ± 0.093	93.220	513.7 ± 3.5	260	0.646 ± 0.040
94.282	78.1 ± 1.4	18	0.331 ± 0.078	94.216	505.2 ± 3.5	161	0.406 ± 0.032
Total	1004.2	695			6051.7	4864	

Table 10: The cross section for $e^+e^- \to \tau^+\tau^-$, from a total of 5559 events. $\sigma^{tot}_{\tau\tau}$ is the total cross section after correction for efficiency and acceptance. The cross sections are quoted with their statistical errors and the point-to-point systematic uncertainty of the luminosity calculation. For the 1990 measurements the overall systematic error on the cross section is 1.5%. The overall systematic error on the cross section for the 1989 measurements is 3.6%.

$\sqrt{s}$ (GeV)	N_F^{ee}	N_B^{ee}	A_{FB}^{ee}
88.234	133	61	0.372 ± 0.067
89.230	213	108	0.328 ± 0.053
90.238	235	149	0.225 ± 0.050
91.034	80	64	0.112 ± 0.083
91.225	2017	1702	0.084 ± 0.016
91.529	80	68	0.081 ± 0.082
92.225	166	142	0.078 ± 0.057
93.229	117	119	-0.008 ± 0.065
94.226	97	63	0.217 ± 0.078
Total	3138	2476	

Table 11: The forward-backward asymmetry, for 1989 and 1990 data, for the channel $e^+e^- \to e^+e^-$ within the angular acceptance $|\cos\theta_{e^-}| < 0.7$ and the acollinearity angle less than 10°, from a total of 5614 events.

$\sqrt{s}$ (GeV)	$N_F^{\mu\mu}$	$N_B^{\mu\mu}$	$A_{FB}^{\mu\mu}$ (counting)	$A_{FB}^{\mu\mu}$ (fitting)
88.233	57	73	-0.128 ± 0.087	-0.159 ± 0.083
89.230	96	162	-0.258 ± 0.060	-0.278 ± 0.057
90.234	179	212	-0.088 ± 0.051	-0.077 ± 0.048
91.040	79	98	-0.11 ± 0.08	-0.11 ± 0.08
91.222	2505	2458	0.009 ± 0.015	0.010 ± 0.013
91.530	116	91	0.12 ± 0.07	0.12 ± 0.07
92.222	303	273	0.052 ± 0.042	0.049 ± 0.040
93.227	192	162	0.085 ± 0.053	0.094 ± 0.051
94.226	127	104	0.101 ± 0.066	0.083 ± 0.061
Total	3654	3633		

Table 12: The forward-backward asymmetry, from combined 1989 and 1990 data, for $e^+e^- \to \mu^+\mu^-$ within $|\cos\theta| < 0.95$, from a total of 7287 events. The forward-backward asymmetries given in column four were obtained from the numbers in columns two and three, after acceptance correction; column five represents the results from a maximum-likelihood fit to the $\cos\theta$ distributions.

$\sqrt{s}$ (GeV)	$N_F^{\tau\tau}$	$N_B^{\tau\tau}$	$A_{FB}^{\tau\tau}$ (counting)	$A_{FB}^{\tau\tau}$ (fitting)
88.234	33	69	-0.357 ± 0.093	-0.344 ± 0.080
89.229	106	118	-0.059 ± 0.067	-0.064 ± 0.062
90.240	127	154	-0.093 ± 0.060	-0.094 ± 0.055
91.030	109	106	0.01 ± 0.07	0.01 ± 0.07
91.225	1843	1879	-0.009 ± 0.016	-0.007 ± 0.015
91.520	109	92	0.08 ± 0.07	0.08 ± 0.07
92.222	225	191	0.081 ± 0.049	0.070 ± 0.046
93.230	167	135	0.108 ± 0.058	0.129 ± 0.055
94.224	98	85	0.079 ± 0.074	0.090 ± 0.072
Total	2817	2829		

Table 13: The forward-backward asymmetry, from combined 1989 and 1990 data, for $e^+e^- \to \tau^+\tau^-$ within $|\cos\theta| < 0.90$, from a total of 5646 events. The forward-backward asymmetries given in column four were obtained from the numbers in columns two and three, after acceptance correction; column five represents the results from a maximum-likelihood fit to the $\cos\theta$ distributions.

	hadronic data only	hadronic data only	SM expectation
M_Z [GeV]	$91.156 \pm 0.009 \pm 0.02$	$91.154 \pm 0.009 \pm 0.02$	91.161 (input)
Γ_Z [GeV]	2.496±0.017		2.487
$\sigma_{\rm had}^{\rm pole}$ [nb]	41.01±0.41		41.47
N_ν		3.046 ± 0.068	3 (input)
χ^2 /NDOF	8.8/15	9.3/16	

Table 14: Results of the fit to the hadronic data. In this fit, the correlation matrix of the LEP energy scale uncertainties for data taken in 1989 and 1990 is taken into account. To facilitate comparison with other LEP experiments, we quote errors on $M_{\rm Z}$ derived from a fit ignoring all energy uncertainties. The second error on $M_{\rm Z}$ reflects all uncertainties in the LEP beam energy. Column 4 indicates the Standard Model expectations assuming $M_{\rm Z} = 91.161$ GeV, the value determined from a combined fit to the hadronic and leptonic data, 3 generations of light neutrinos, $M_{\rm t} = 150$ GeV, $M_{\rm H} = 300$ GeV and $\alpha_s = 0.118$.

	with lepton universality	w/o lepton universality	SM expectation
Γ_{ee} [MeV] $\Gamma_{\mu\mu}$ [MeV] $\Gamma_{\tau\tau}$ [MeV]		82.9±1.0 83.2±1.5 82.7±1.9	
$\Gamma_{l^+l^-}$ [MeV]	83.00±0.69		83.5
$\kappa^a_{ZZ}\hat{a}_l^2\hat{v}_l^2(ee)$ $\kappa^a_{ZZ}\hat{a}_l^2\hat{v}_l^2(\mu\mu)$ $\kappa^a_{ZZ}\hat{a}_l^2\hat{v}_l^2(\tau\tau)$		-0.0039±0.0069 0.0028±0.0040 0.0029±0.0046	
$\kappa^a_{ZZ}\hat{a}_l^2\hat{v}_l^2$	0.0017±0.0028		0.0047
$\kappa^a_{\gamma Z}\hat{a}_l^2(ee)$ $\kappa^a_{\gamma Z}\hat{a}_l^2(\mu\mu)$ $\kappa^a_{\gamma Z}\hat{a}_l^2(\tau\tau)$		0.82±0.30 0.90±0.16 0.91±0.17	
$\kappa^a_{\gamma Z}\hat{a}_l^2$	0.89±0.11		1.003
M_Z [GeV] Γ_Z [GeV] Γ_{had} [GeV]	91.161±0.009±0.020 2.492±0.016 1.739±0.017	91.161±0.009±0.020 2.492±0.016 1.740±0.021	91.161 (input) 2.487 1.736
χ^2 /NDOF	60.0/87	59.1/81	

Table 15: Results of the model independent fits to the combined e^+e^-, $\mu^+\mu^-$ and $\tau^+\tau^-$ cross sections and forward-backward asymmetries. For column 2 lepton universality has been assumed. Column 3 makes no assumption of lepton universality in regards to any partial width. The values obtained for the leptonic partial widths in column 3 are a direct test of lepton universality. To facilitate comparison with other LEP experiments, we quote errors on M_Z derived from a fit ignoring all energy uncertainties. The second error on M_Z reflects all uncertainties in the LEP beam energy. Column 4 indicates the Standard Model expectations assuming M_Z = 91.161 GeV, 3 generations of light neutrinos, M_t = 150 GeV, M_H = 300 GeV and α_s = 0.118. The correlation matrices for the parameters extracted from these fits are shown in Tables 1 and 2 of Appendix A.

	e^+e^-	$\mu^+\mu^-$	$\tau^+\tau^-$
$\Gamma_{l^+l^-}$ [MeV]	82.9±1.0	83.0±0.8	82.8 ±1.0
$\kappa^a_{ZZ}\hat{a}_l^2\hat{v}_l^2$	-0.0038±0.0069	0.0028±0.0040	0.0028±0.0046
$\kappa^a_{\gamma Z}\hat{a}_l^2$	0.82±0.30	0.90±0.16	0.91±0.17
M_Z [GeV]	91.156±0.009	91.160±0.009	91.158±0.009
Γ_Z [GeV]	2.491±0.017	2.491±0.017	2.493±0.017
Γ_{had} [GeV]	1.739±0.022	1.736±0.019	1.742±0.022
χ^2 /NDOF	28.3/37	28.1/37	20.8/37

Table 16: Results of the fits to the lepton pair cross sections and forward-backward asymmetries: for the results presented here each lepton species was fit individually. In each case universality has been assumed between initial and final state leptons. The hadronic cross section measurements are also included in every fit. To facilitate comparison with other LEP experiments, we quote errors on M_Z derived from a fit ignoring all energy uncertainties. M_Z has an additional error of 0.02 GeV from the LEP energy uncertainties.

	$\hat{a}_l^2$, $\hat{v}_l^2$ fit	ρ_Z, $\sin^2\overline{\theta}_W$ fit	$\sin^2\overline{\theta}_W^{IBA}$ fit
$\hat{a}_l^2$	0.998 ±0.009		
$\hat{v}_l^2$	0.0023 ±0.0028		
ρ_Z		0.998±0.009	
$\sin^2\overline{\theta}_W$		$0.238^{+0.030}_{-0.006}$	0.2337±0.0021
M_Z [GeV]	91.162±0.009	91.162±0.009	91.162±0.009
Γ_Z [GeV]	2.492±0.016	2.492±0.016	2.489±0.016
Γ_{had} [GeV]	1.739±0.017	1.739±0.017	1.738±0.017
χ^2 /NDOF	61.1/88	61.1/88	61.7/89

Table 17: Results of the fits to the combined e^+e^-, $\mu^+\mu^-$ and $\tau^+\tau^-$ cross sections and forward-backward asymmetries based on the improved Born approximation. Lepton universality has been assumed. The hadronic cross section measurements are also included in every fit. In the ρ_Z, $\sin^2\overline{\theta}_W$ fit, the value of $\sin^2\overline{\theta}_W < 0.25$ has been chosen from the two possible solutions, which are symmetric about $\sin^2\overline{\theta}_W = 0.25$. M_Z has an additional error of 0.02 GeV from the LEP energy uncertainties.

SM parameter	OPAL data only	OPAL M_Z and M_W	full OPAL data and M_W
M_Z [GeV]	$91.165 \pm 0.009 \pm 0.02$	$91.160 \pm 0.009 \pm 0.02$	$91.165 \pm 0.009 \pm 0.02$
M_t [GeV]	$100^{+70}_{-52}\ ^{+24}_{-11}(M_H)$	$149^{+46}_{-57}\ ^{+15}_{-19}(M_H)$	$129^{+42}_{-39}\ ^{+24}_{-16}(M_H)$
$\Lambda_{\overline{MS}}$ [MeV]	280^{+120}_{-95}	—	280^{+120}_{-95}
α_s	0.122 ± 0.007	—	0.122 ± 0.007
χ^2 /NDOF	63.8/91	0.9/1	64.8/93

Table 18: The values obtained by Standard Model fits to our data for the parameters: M_Z, M_t and $\Lambda_{\overline{MS}}$, or equivalently α_s. The central values given were obtained from a fit assuming $M_H = 300$ GeV. The uncertainty due to the unknown mass of the Higgs was derived from the observed changes in mean value obtained for fits carried out assuming four values of the Higgs mass in the range $50 \leq M_H \leq 1000$ GeV. For these fits the value of $\alpha_s = 0.118 \pm 0.008$ was used. In column 2 are listed the values obtained for these Standard Model parameters by a fit to the OPAL line shape and forward-backward asymmetry data alone. In column 3 are listed the results obtained by combining the OPAL measurement of M_Z with the measurements of M_W/M_Z and M_W from the UA2 and CDF experiments [31,32]. Finally, in column 4 are listed the values obtained by combining the full set of OPAL line shape and forward-backward asymmetry measurements with the measurements of M_W and M_W/M_Z. The χ^2 curves for M_t for each of these sets of fits are shown in Figure 20.

SM parameter	OPAL data only	OPAL data and M_{W}
M_{W} [GeV]	79.93 ± 0.36	80.03 ± 0.23
$\sin^2\theta_{\mathrm{W}} \equiv 1 - \frac{M_{\mathrm{W}}^2}{M_{\mathrm{Z}}^2}$	0.231 ± 0.007	0.2291 ± 0.0046
$\sin^2\overline{\theta}_{\mathrm{W}}^{\mathrm{SM}}(\mathrm{lept})$	0.2341 ± 0.0021	0.2336 ± 0.0016
$\sin^2\overline{\theta}_{\mathrm{W}}^{\mathrm{SM}}(b)$	0.2345 ± 0.0015	0.2342 ± 0.0012

Table 19: The values obtained by Standard Model fits to our data for the parameters: M_{W}, $\sin^2\theta_{\mathrm{W}} \equiv 1 - \frac{M_{\mathrm{W}}^2}{M_{\mathrm{Z}}^2}$, the effective weak mixing angle $\sin^2\overline{\theta}_{\mathrm{W}}^{\mathrm{SM}}(\mathrm{lept})$ for leptons and the effective weak mixing angle $\sin^2\overline{\theta}_{\mathrm{W}}^{\mathrm{SM}}(b)$ for b quarks. These were derived by a parameter transformation from the Standard Model fits for M_{Z}, M_{t} and $\Lambda_{\overline{MS}}$ (see Table 18). The central values given were obtained from a fit assuming $M_{\mathrm{H}} = 300$ GeV. For each parameter, the uncertainty due to the unknown mass of the Higgs was derived from the observed changes in mean value obtained for fits carried out assuming four values of the Higgs mass in the range $50 \leq M_{\mathrm{H}} \leq 1000$ GeV. For these fits the value of $\alpha_s = 0.118 \pm 0.008$ was used. In column 2 are listed the values obtained for these Standard Model parameters by a fit to the OPAL line shape and forward-backward asymmetry data alone. The value of $M_{\mathrm{W}} = 79.93 \pm 0.36$ GeV implied by our data is in excellent agreement with the direct measurements of CDF and UA2 experiments [31,32], and of a similar precision. In column 3 are listed the values obtained for each parameter by a set of fits which combines our data with the measurements of $M_{\mathrm{W}}/M_{\mathrm{Z}}$ and M_{W} from UA2 and CDF. The χ^2 curves for each parameter are shown in Figures 21 and 22, for each of these sets of fits.

SM parameter	OPAL data and M_W	OPAL R_Z only
M_Z [GeV]	$91.161 \pm 0.009 \pm 0.02$	—
M_t [GeV]	$119 \pm 44 \pm 18(M_H)$	—
$\Lambda_{\overline{MS}}$ [MeV]	670^{+700}_{-400}	750^{+1200}_{-600}
α_s	$0.141^{+0.022}_{-0.020}$	$0.147^{+0.032}_{-0.029}$

Table 20: For these fits no external constraint on α_s was imposed. In column 2 are listed the values obtained for each parameter by a set of fits which combines our data with the measurements of M_W/M_Z and M_W from the UA2 and CDF experiments [31,32]. The central values given were obtained from a fit assuming $M_H = 300$ GeV. The uncertainty due to the unknown mass of the Higgs was derived from the observed changes in mean value obtained for fits carried out assuming four values of the Higgs mass in the range $50 \leq M_H \leq 1000$ GeV. The χ^2 contour in the M_t versus $\Lambda_{\overline{MS}}$ plane for the fit assuming $M_H = 300$ GeV is shown in figure 23. In column 3 is shown the result obtained from Standard Model fits to the OPAL measurement of $R_Z \equiv \Gamma_{had}/\Gamma_{l^+l^-}$ for $\Lambda_{\overline{MS}}$, or equivalently α_s. The central value given was obtained from a fit assuming $M_t = 150$ GeV and $M_H = 300$ GeV.

APPENDIX A: Parameter Correlation Matrices

In this Appendix are listed the parameter correlation matrices for model independent fits to the OPAL data discussed in Section 6.5.1 of the text. Two correlation matrices are provided in the form of Tables: the first one refers to a fit which assumes lepton universality, the second to a fit carried out without assumption of lepton universality. The results of these two fits are summarised in columns 2 and 3 of Table 15.

Parameter		1	2	3	4	5	6
1	M_Z	1.000	0.052	0.052	0.023	-0.009	0.036
2	Γ_{had}	0.052	1.000	0.279	0.535	0.028	0.009
3	$\Gamma_{l^+l^-}$	0.052	0.279	1.000	0.653	0.106	0.041
4	Γ_Z	0.023	0.535	0.653	1.000	0.069	0.019
5	$\kappa^a_{\gamma Z}\hat{a}_l^2$	-0.009	0.028	0.106	0.069	1.000	0.138
6	$\kappa^a_{ZZ}\hat{a}_l^2\hat{v}_l^2$	0.036	0.009	0.041	0.019	0.138	1.000

Table 1: The parameter correlation matrix for the model independent fit, assuming lepton universality. The results of this fit are summarised in column 2 Table 15.

Parameter		1	2	3	4	5	6	7	8	9	10	11	12
1	M_Z	1.000	0.073	0.015	0.061	0.044	0.042	0.030	-0.008	-0.004	0.008	0.020	0.021
2	$\Gamma_{\rm had}$	0.073	1.000	-0.290	0.584	0.465	0.418	0.038	0.034	0.033	-0.070	0.014	0.012
3	Γ_{ee}	0.015	-0.290	1.000	-0.195	-0.157	0.466	-0.048	0.042	0.041	0.109	0.009	0.006
4	$\Gamma_{\mu\mu}$	0.061	0.584	-0.195	1.000	0.309	0.310	0.027	0.084	0.022	-0.049	0.018	0.008
5	$\Gamma_{\tau\tau}$	0.044	0.465	-0.157	0.309	1.000	0.247	0.021	0.017	0.106	-0.040	0.008	0.017
6	Γ_Z	0.042	0.418	0.466	0.310	0.247	1.000	0.005	0.053	0.053	-0.003	0.018	0.015
7	$\kappa^a_{\gamma Z}\hat{a}^2_l(ee)$	0.030	0.038	-0.048	0.027	0.021	0.005	1.000	-0.001	-0.001	0.003	0.002	0.002
8	$\kappa^a_{\gamma Z}\hat{a}^2_l(\mu\mu)$	-0.008	0.034	0.042	0.084	0.017	0.053	-0.001	1.000	0.005	0.003	0.146	0.000
9	$\kappa^a_{\gamma Z}\hat{a}^2_l(\tau\tau)$	-0.004	0.033	0.041	0.022	0.106	0.053	-0.001	0.005	1.000	0.002	0.001	0.161
10	$\kappa^a_{ZZ}\hat{a}^2_l\hat{v}^2_l(ee)$	0.008	-0.070	0.109	-0.049	-0.040	-0.003	0.003	0.003	0.002	1.000	-0.002	-0.002
11	$\kappa^a_{ZZ}\hat{a}^2_l\hat{v}^2_l(\mu\mu)$	0.020	0.014	0.009	0.018	0.008	0.018	0.002	0.146	0.001	-0.002	1.000	0.003
12	$\kappa^a_{ZZ}\hat{a}^2_l\hat{v}^2_l(\tau\tau)$	0.021	0.012	0.006	0.008	0.017	0.015	0.002	0.000	0.161	-0.002	0.003	1.000

Table 2:
The parameter correlation matrix for the model independent fit performed without assumption of lepton universality. The results of this fit are summarised in column 3 Table 15.

Figure 1

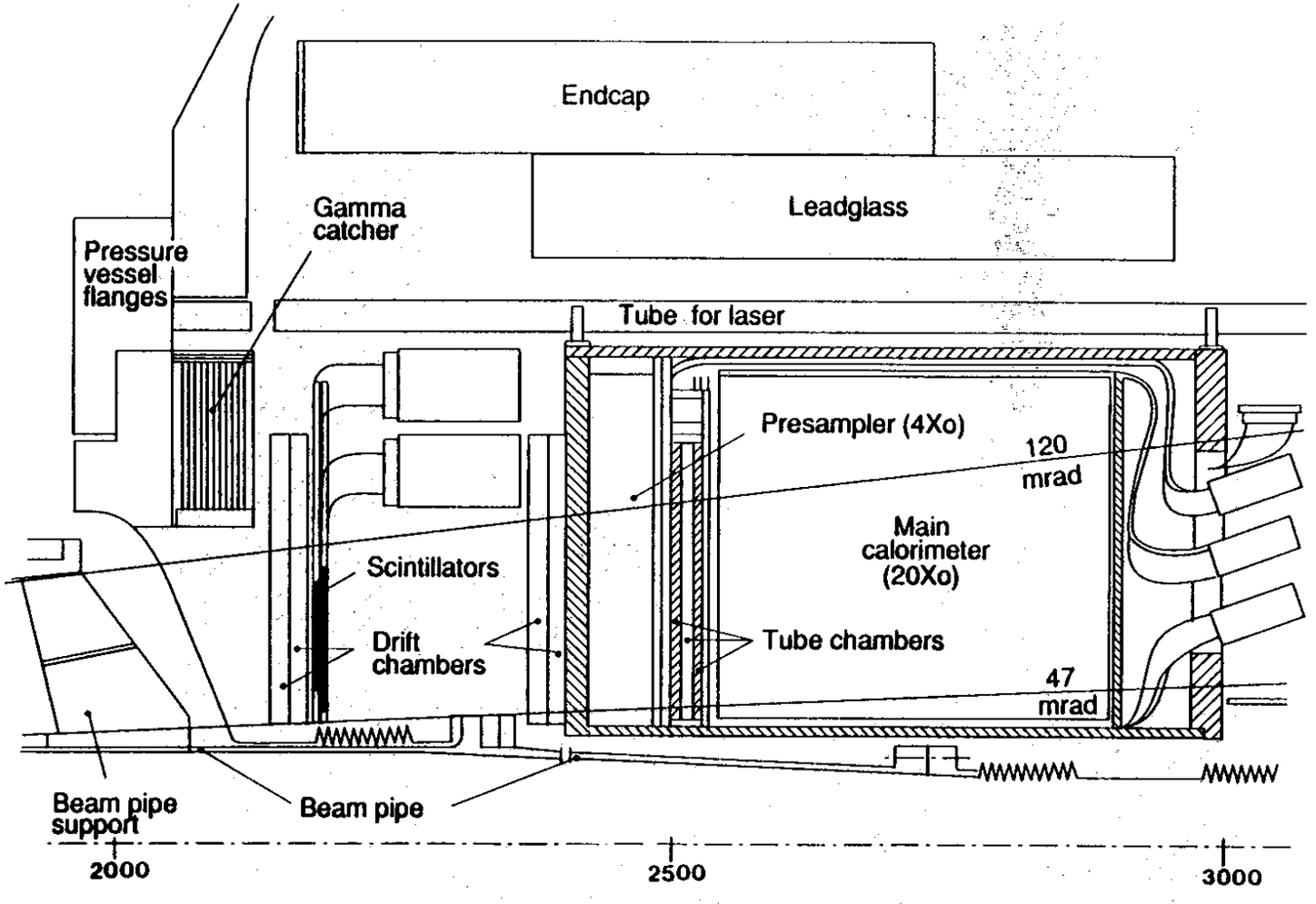
Endcap
Leadglass
Gamma catcher
Pressure vessel flanges
Tube for laser
Presampler (4Xo)
120 mrad
Main calorimeter (20Xo)
Scintillators
Drift chambers
Tube chambers
47 mrad
Beam pipe support
Beam pipe
2000
2500
3000

Figure 2

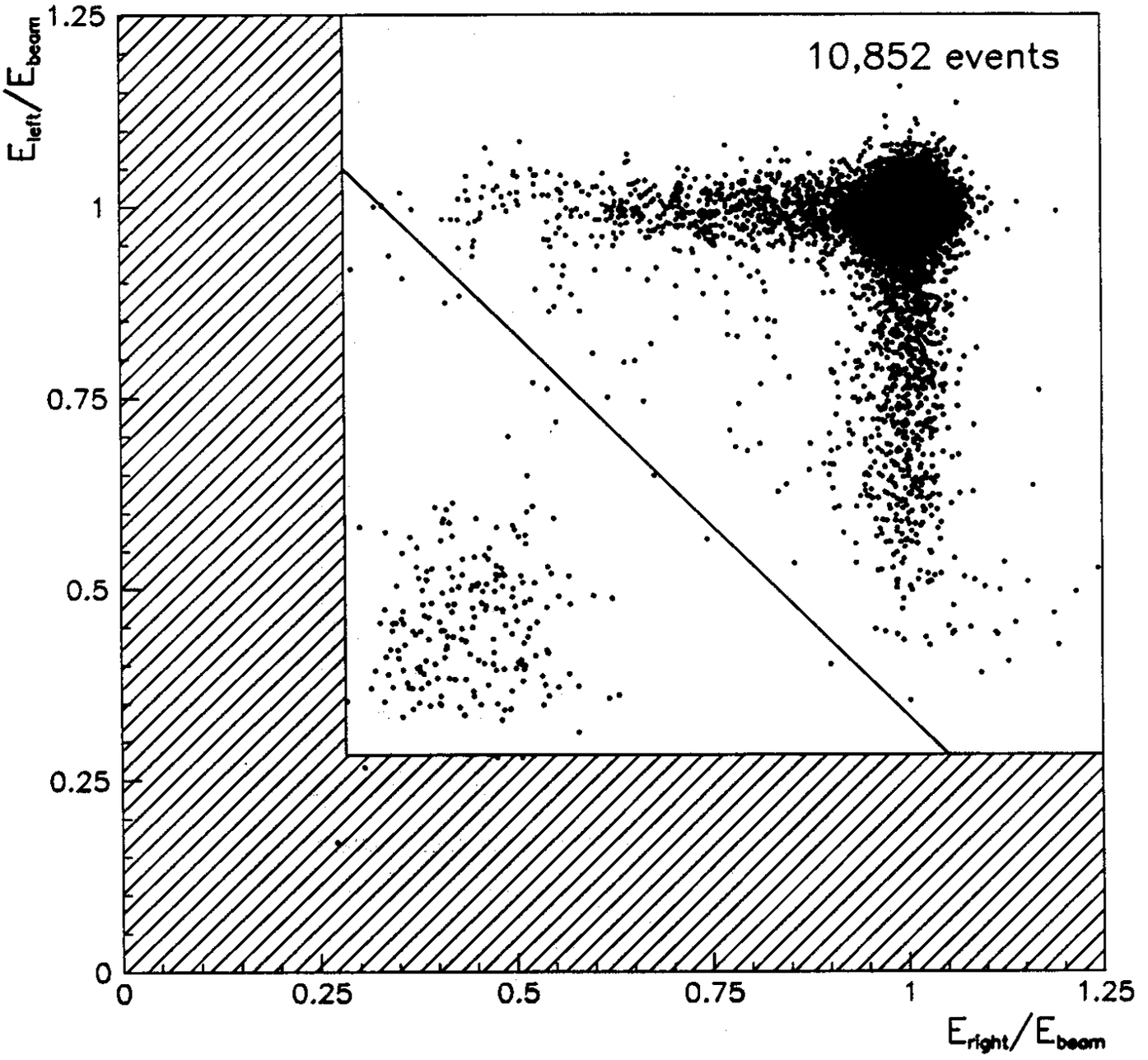

Figure 3,4

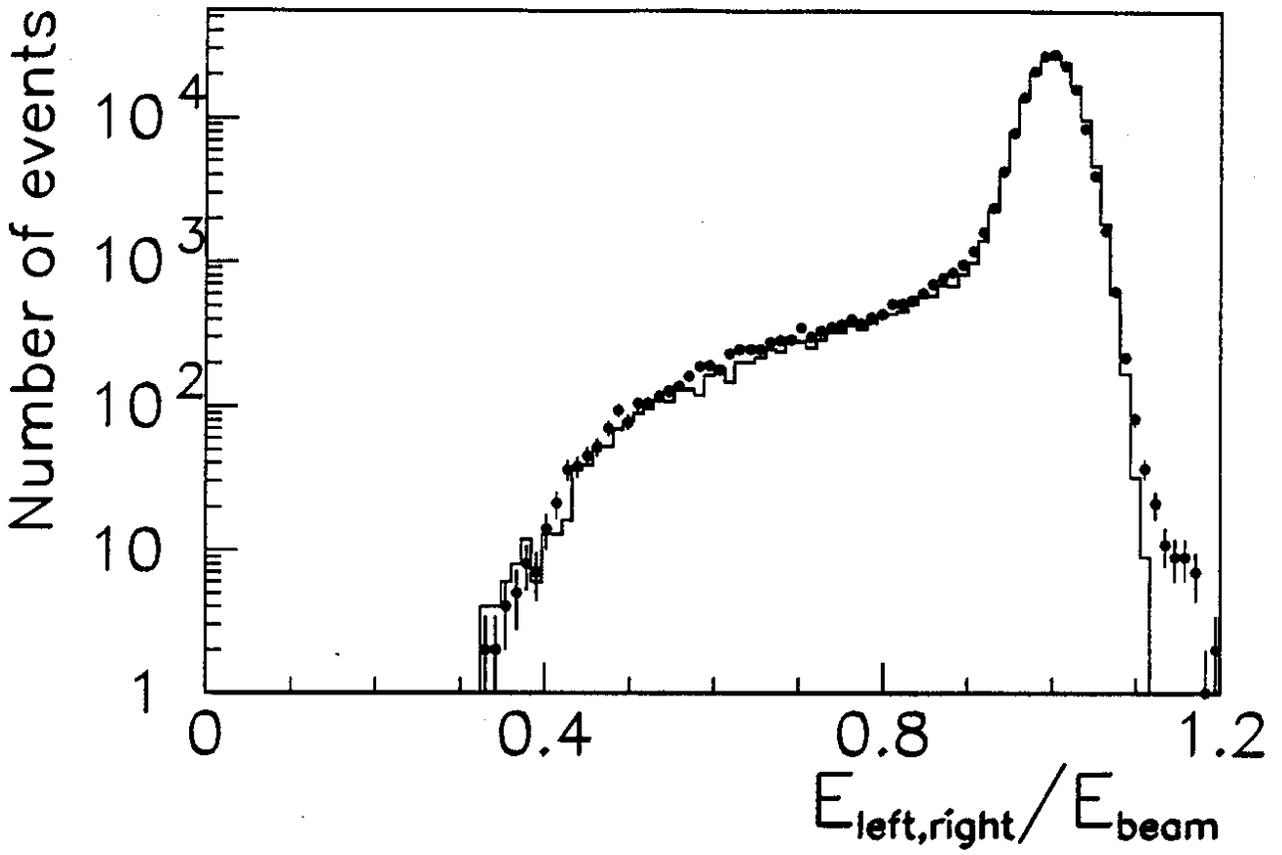
Number of events
10 4
10 3
10 2
10
1
0
0.4
0.8
1.2
E left,right / E beam

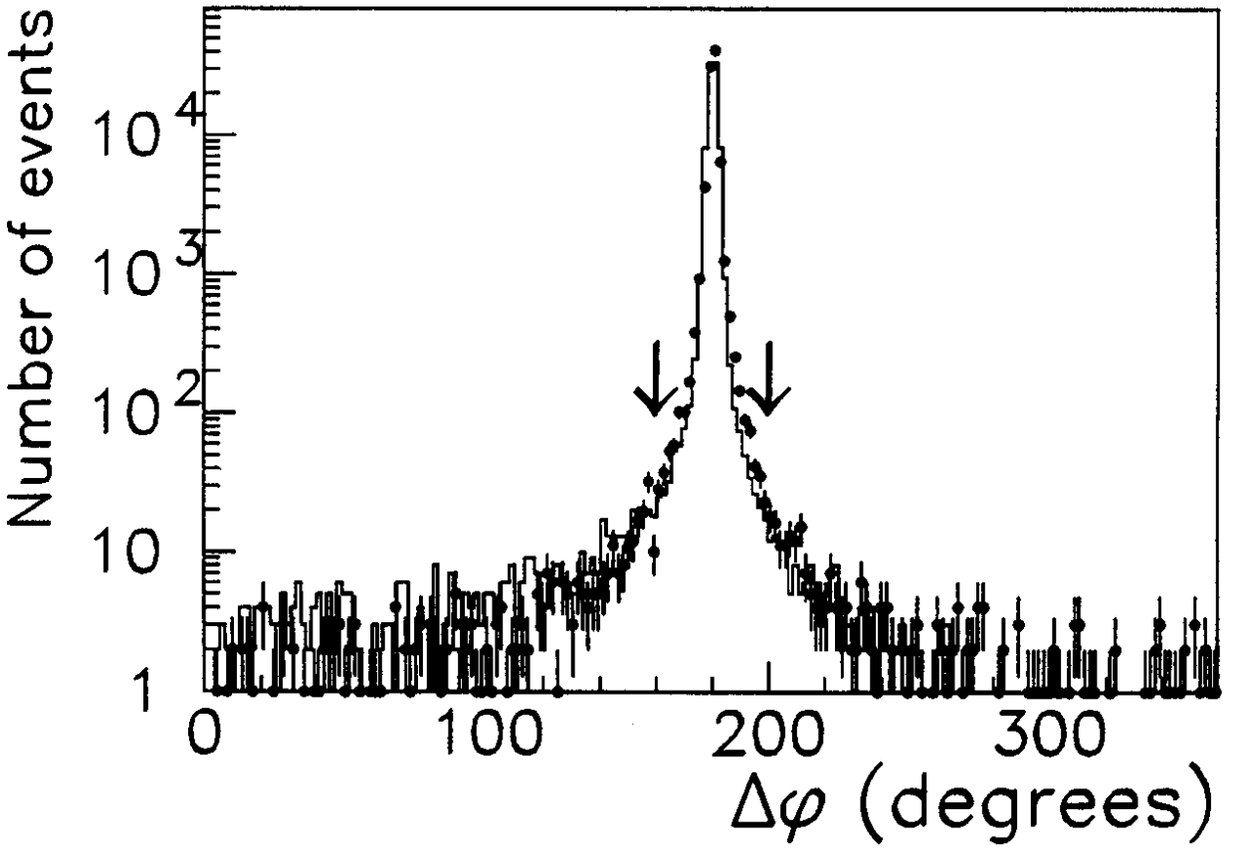
Number of events
10 4
10 3
10 2
10
1
0
100
200
300
Δφ (degrees)

Figure 5

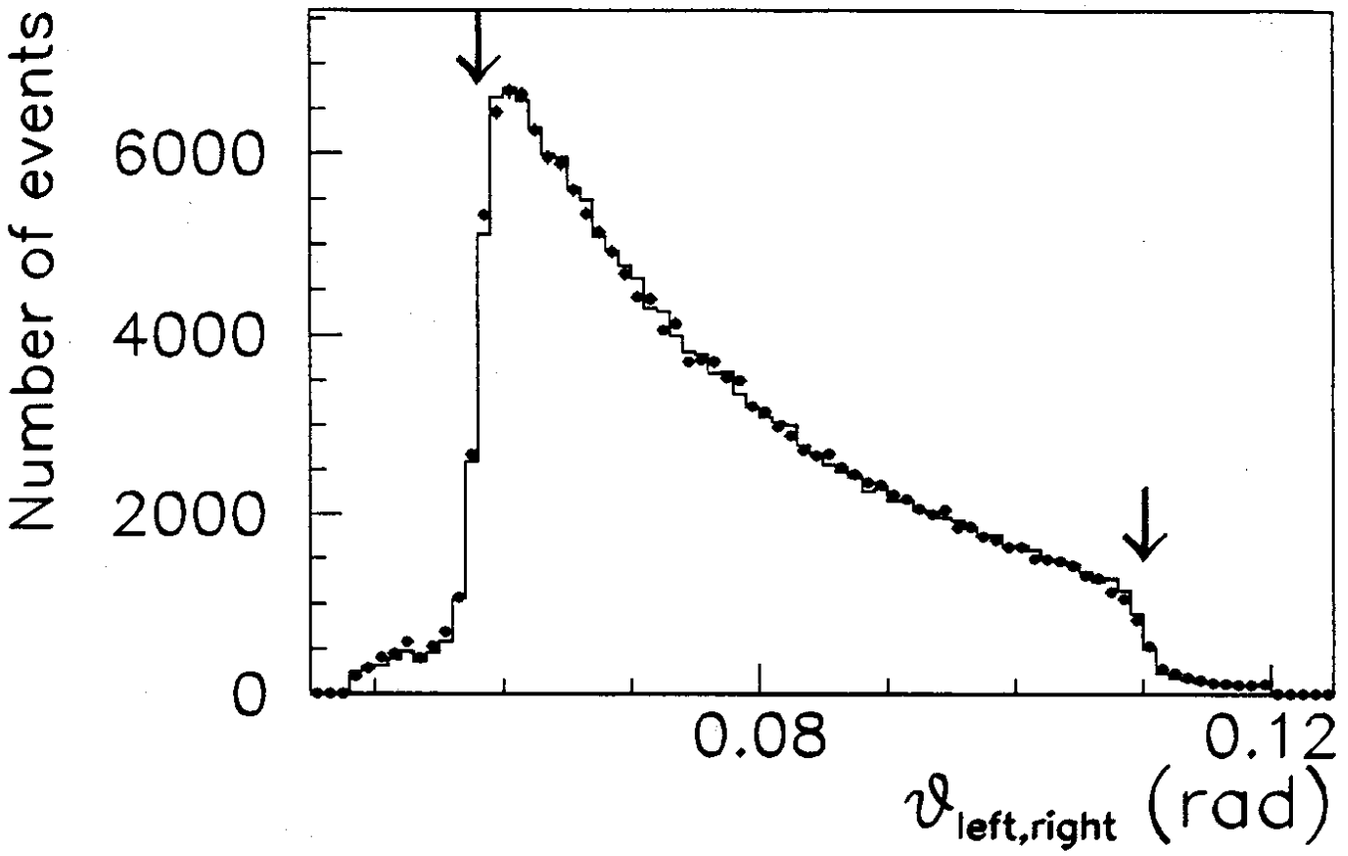
Number of events
6000
4000
2000
0
0.08
0.12
$\vartheta_{left,right}$ (rad)

Figure 6

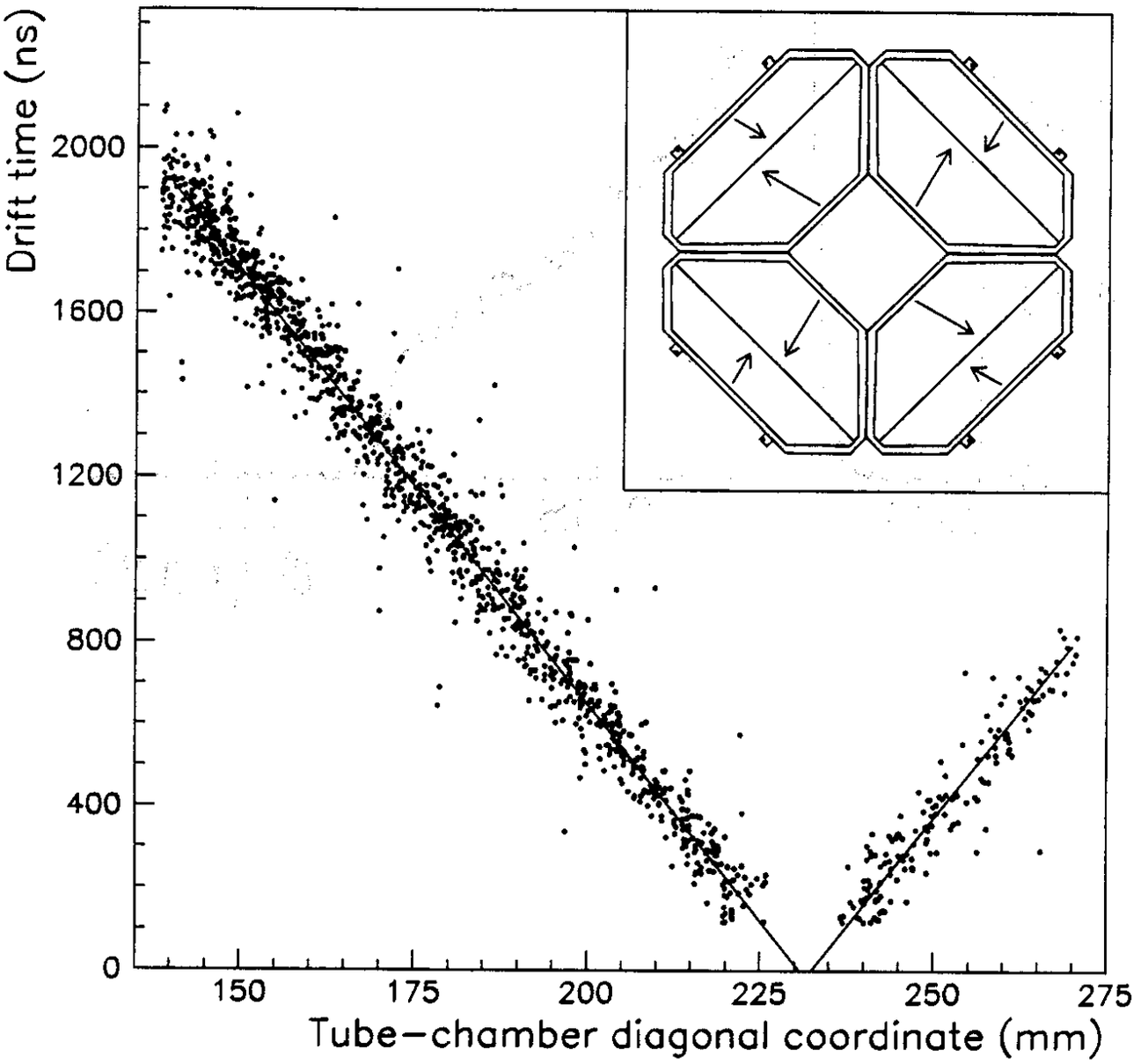
Drift time (ns)
2000
1600
1200
800
400
0
150
175
200
225
250
275
Tube–chamber diagonal coordinate (mm)

Figure 7

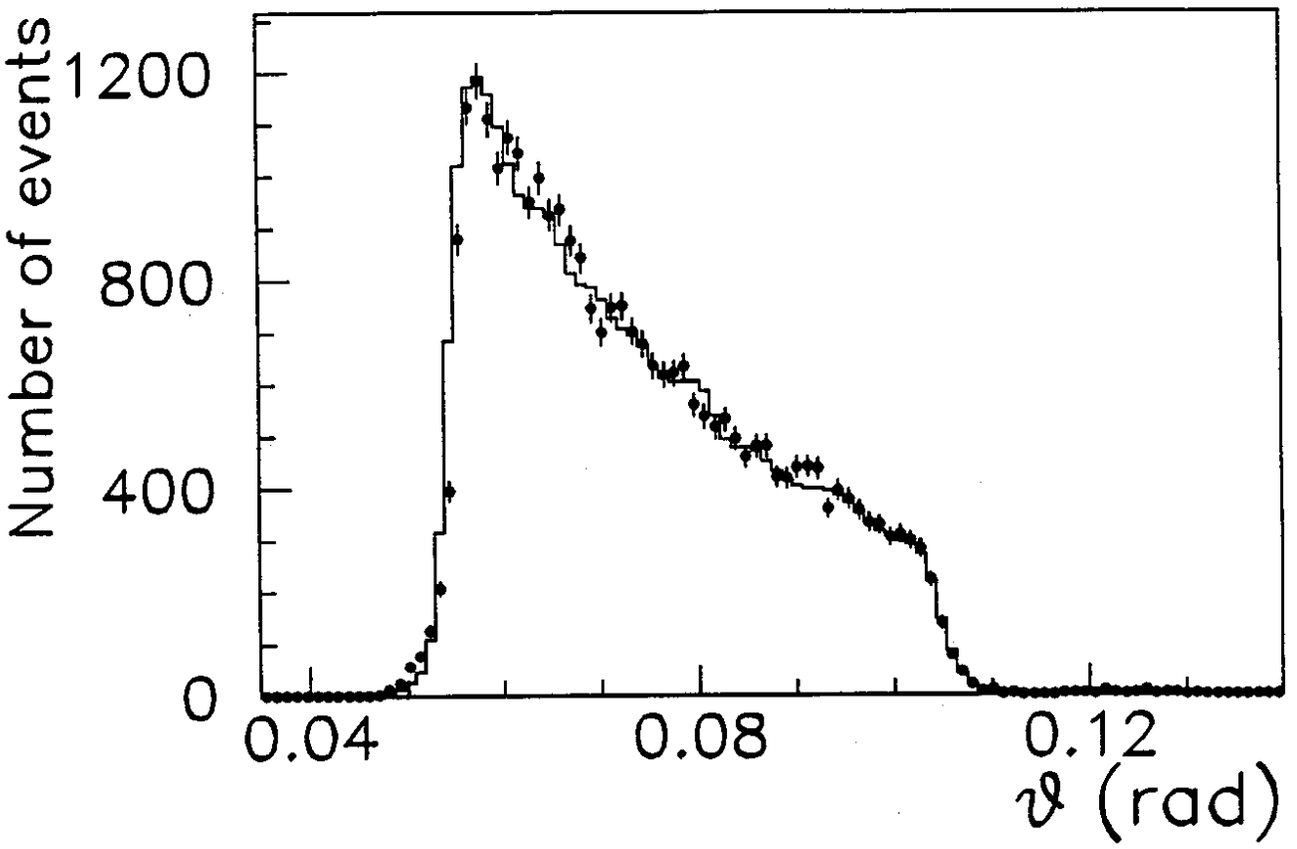

Figure 8 a,b

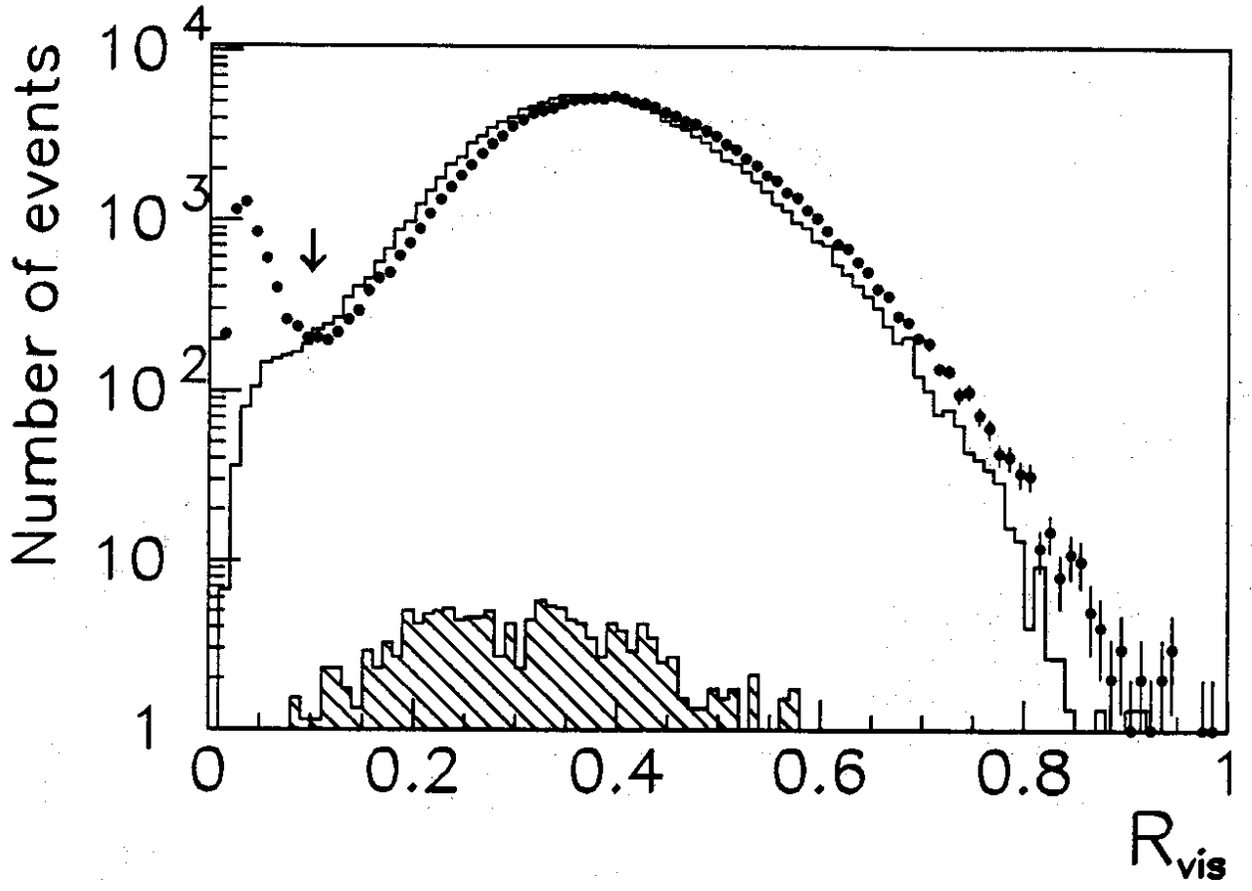
Number of events
10^4
10^3
10^2
10
1
0
0.2
0.4
0.6
0.8
1
R_{vis}

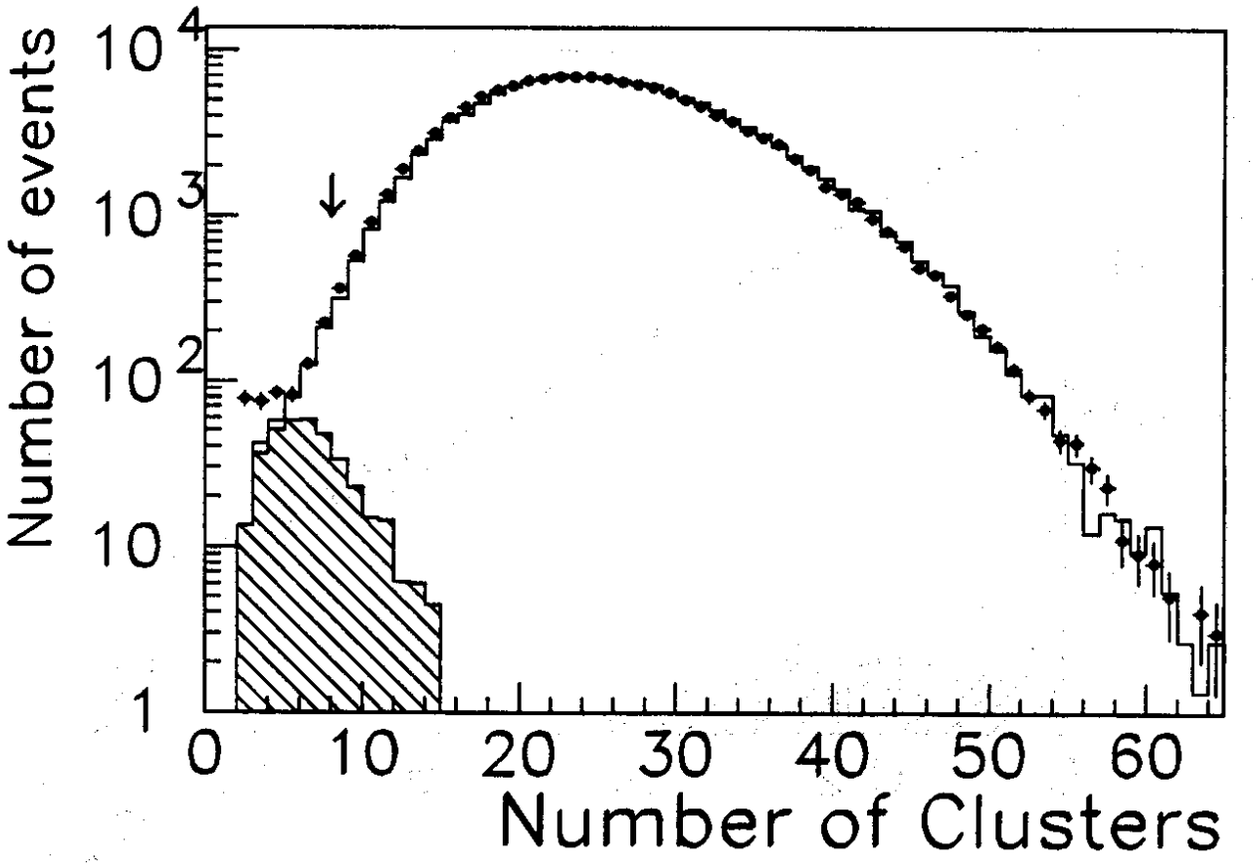
Number of events
10^4
10^3
10^2
10
1
0
10
20
30
40
50
60
Number of Clusters

Figure 8 c,d

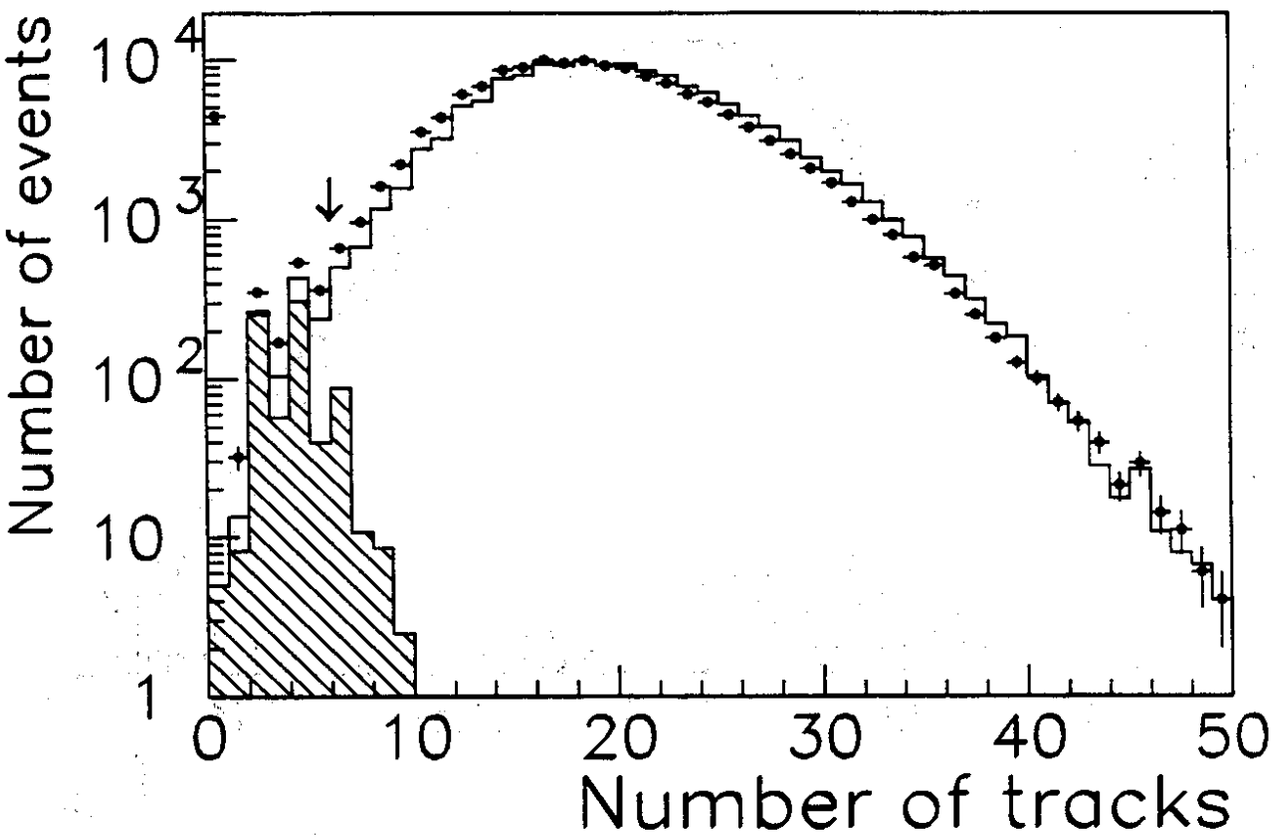
Number of events
10^4
10^3
10^2
10
1
0
10
20
30
40
50
Number of tracks

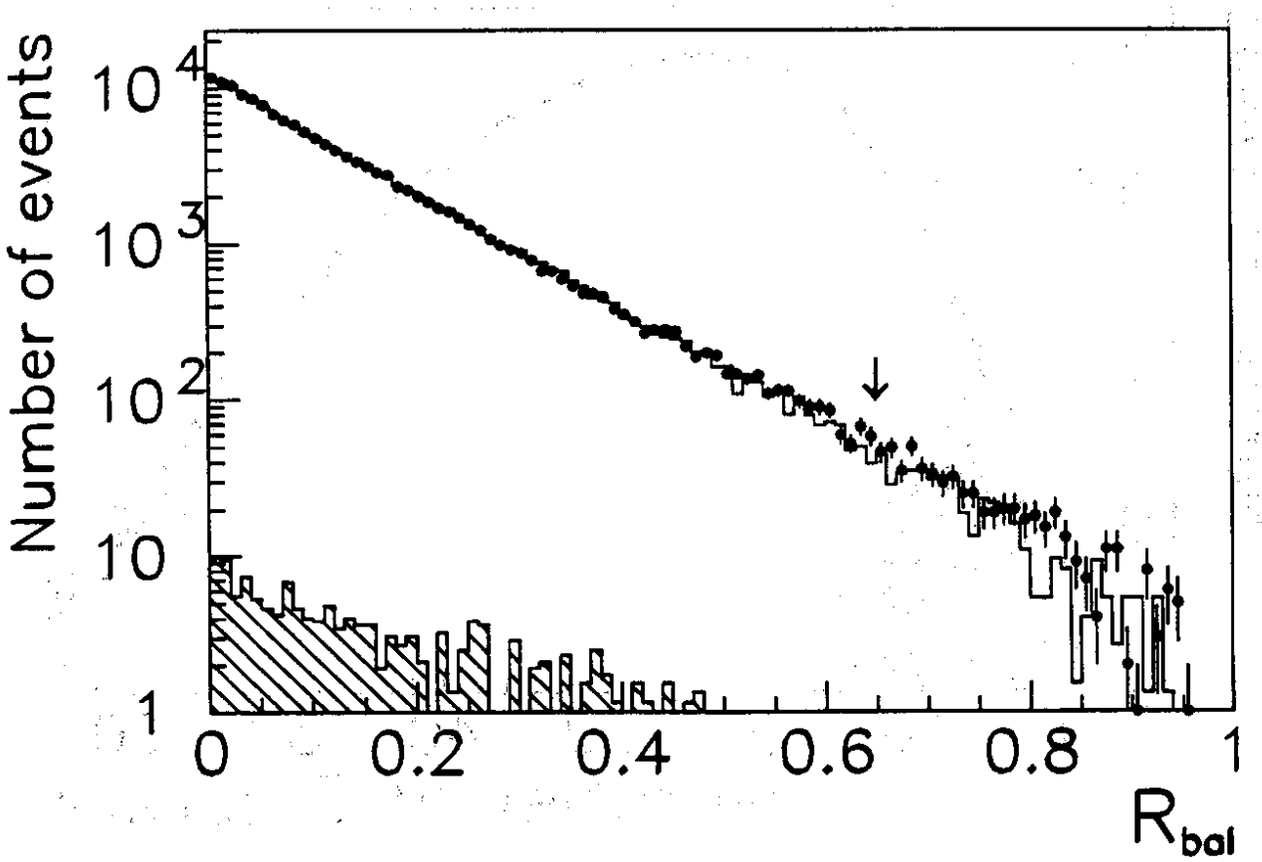
Number of events
10^4
10^3
10^2
10
1
0
0.2
0.4
0.6
0.8
1
R_bal

Figure 9

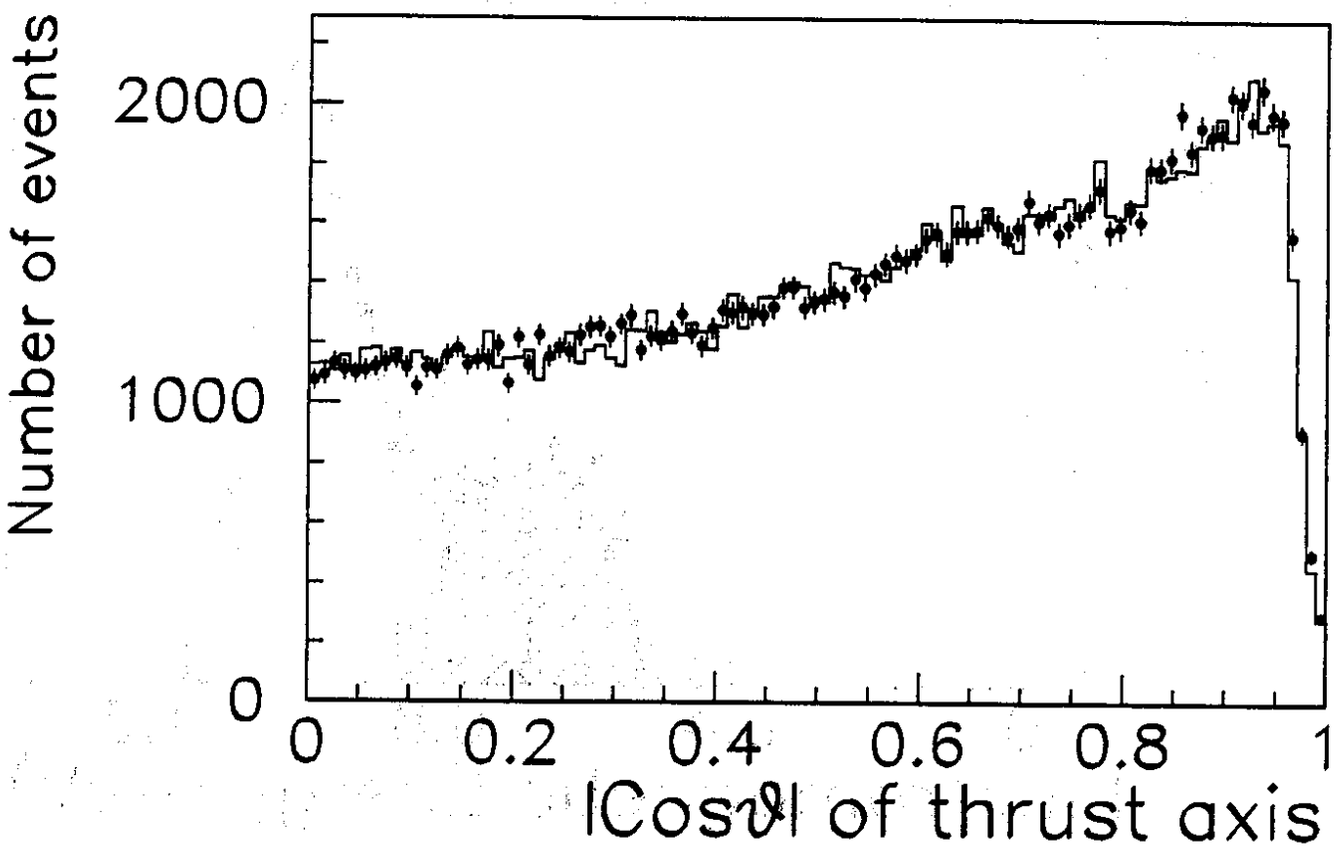

Figure 10

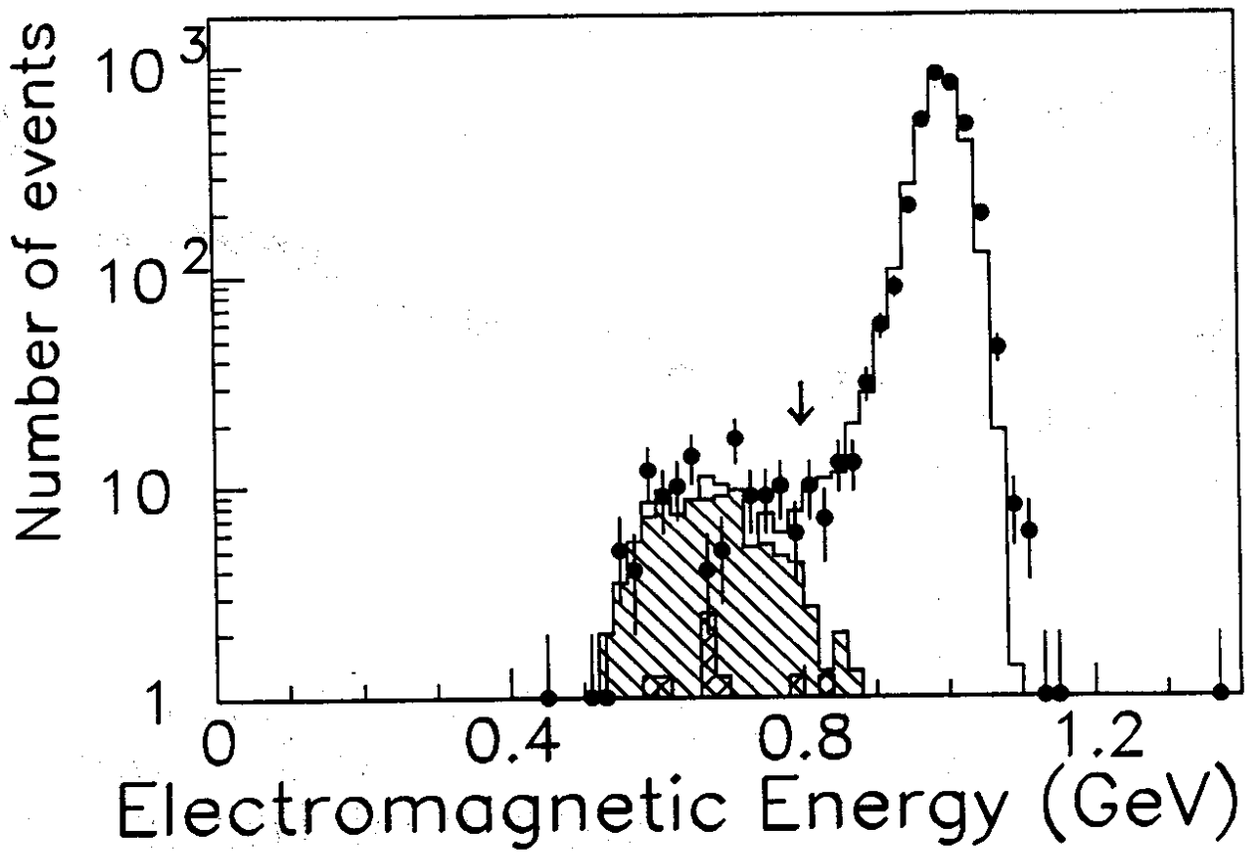
Number of events
10 3
10 2
10
1
0
0.4
0.8
1.2
Electromagnetic Energy (GeV)

Figure 11 a, b

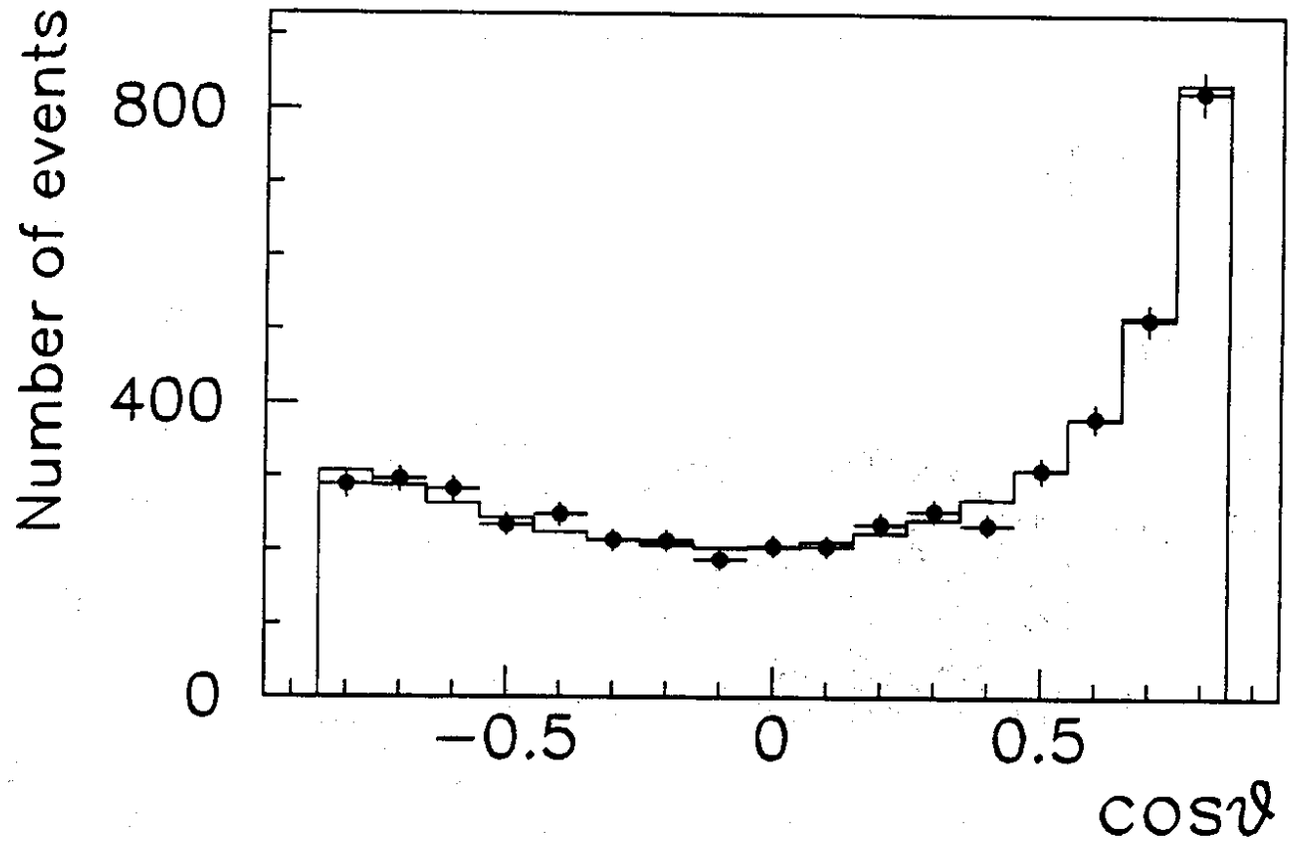
Number of events
800
400
0
−0.5
0
0.5
cosϑ

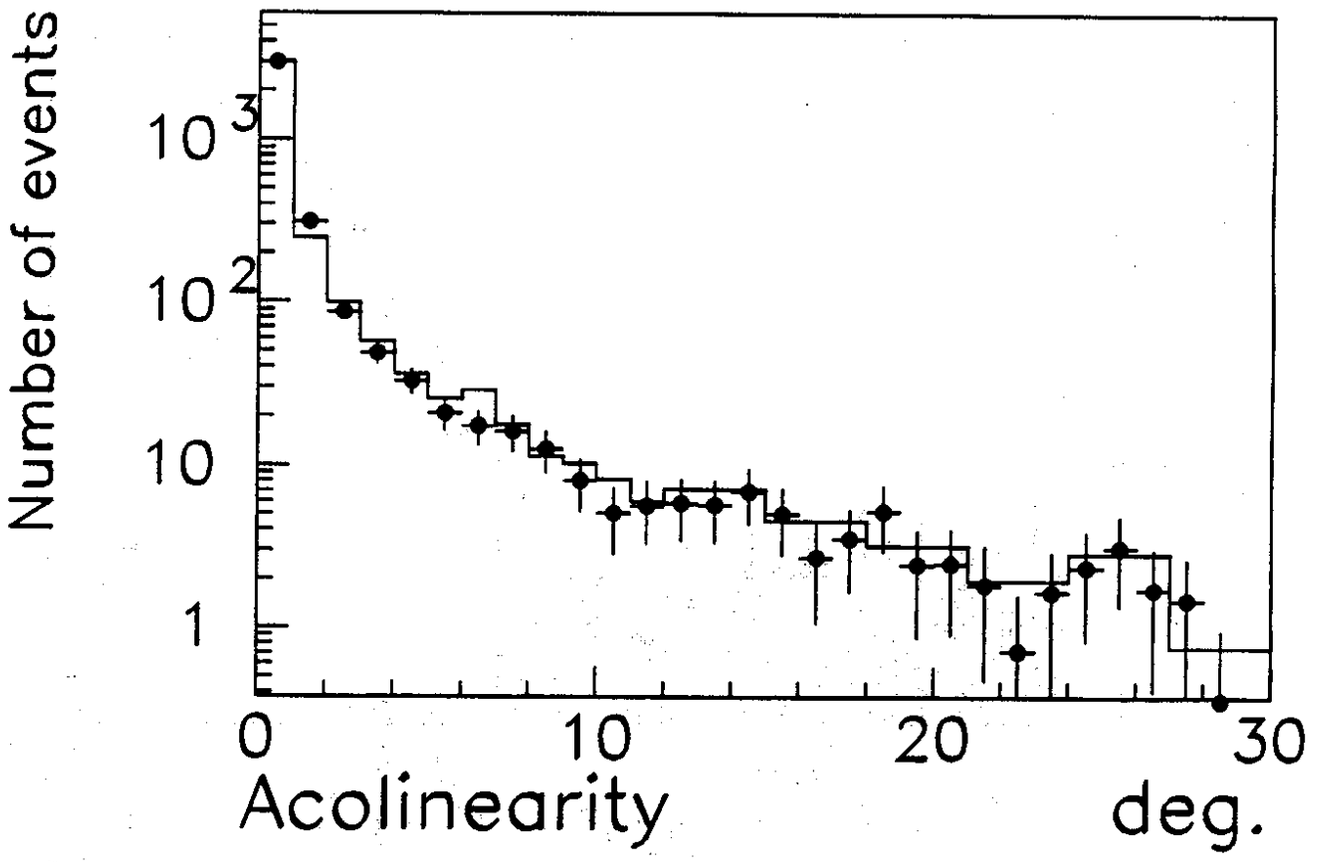
Number of events
10 3
10 2
10
1
0
10
20
30
Acolinearity
deg.

Figure 12 a, b ,c

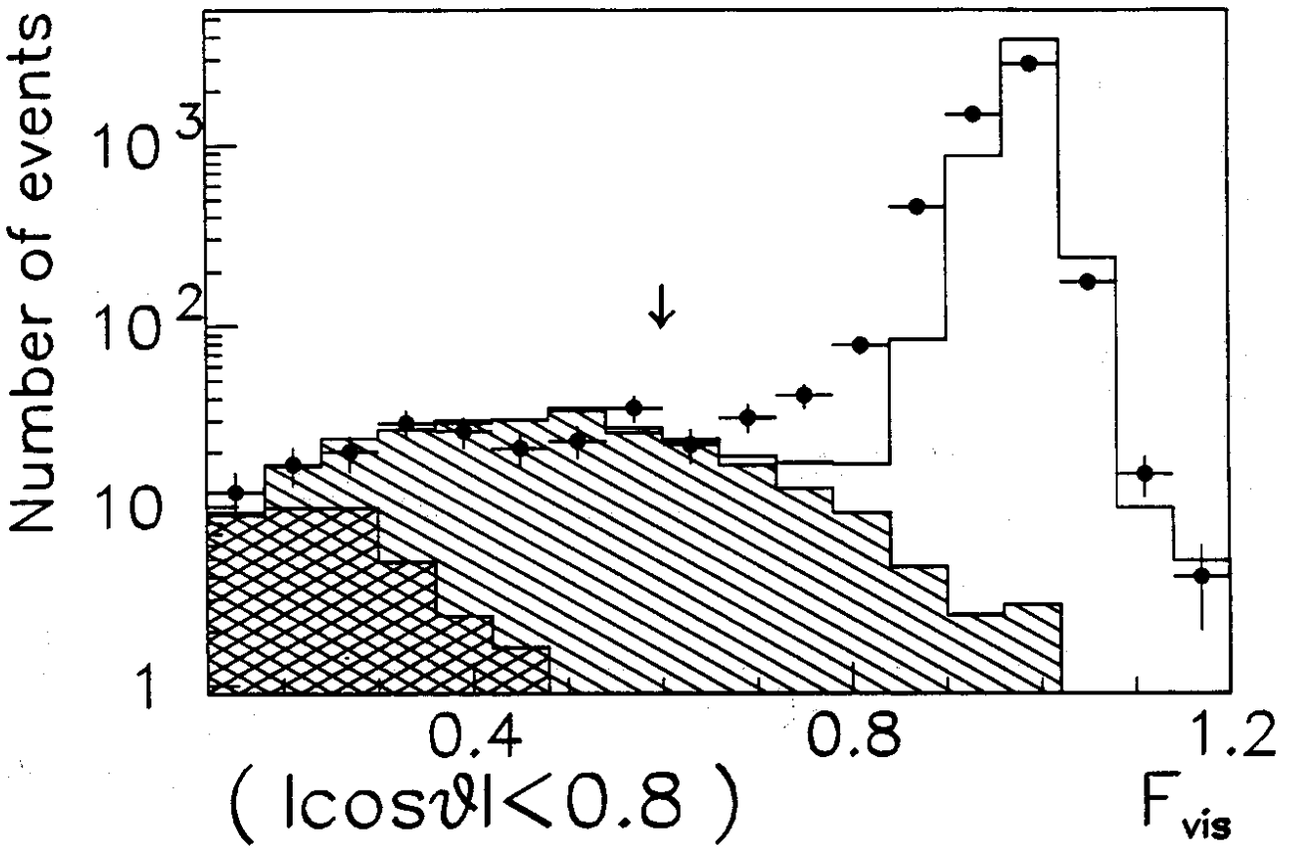

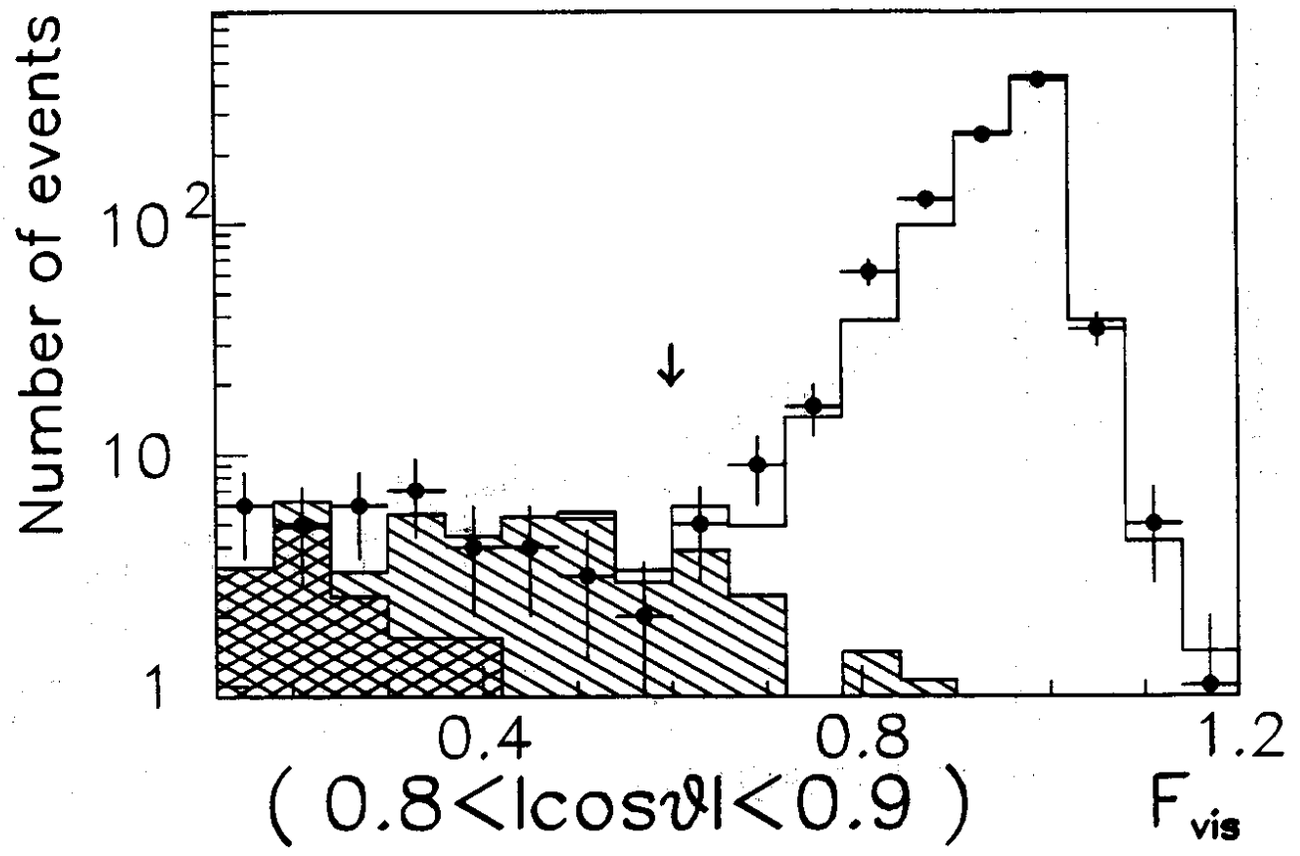

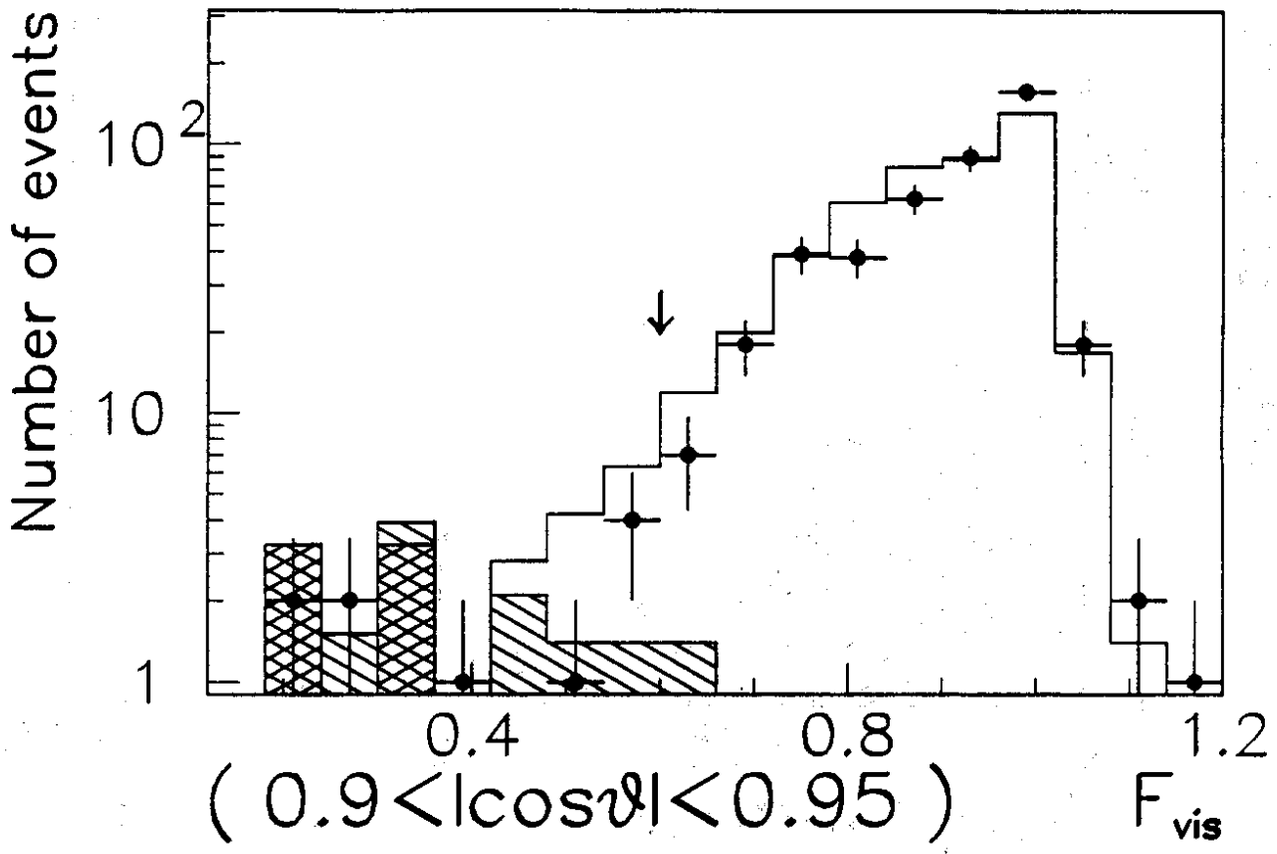
Number of events
10 2
10
1
0.4
0.8
1.2
(0.9<|cosϑ|<0.95)
F vis

Figure 13

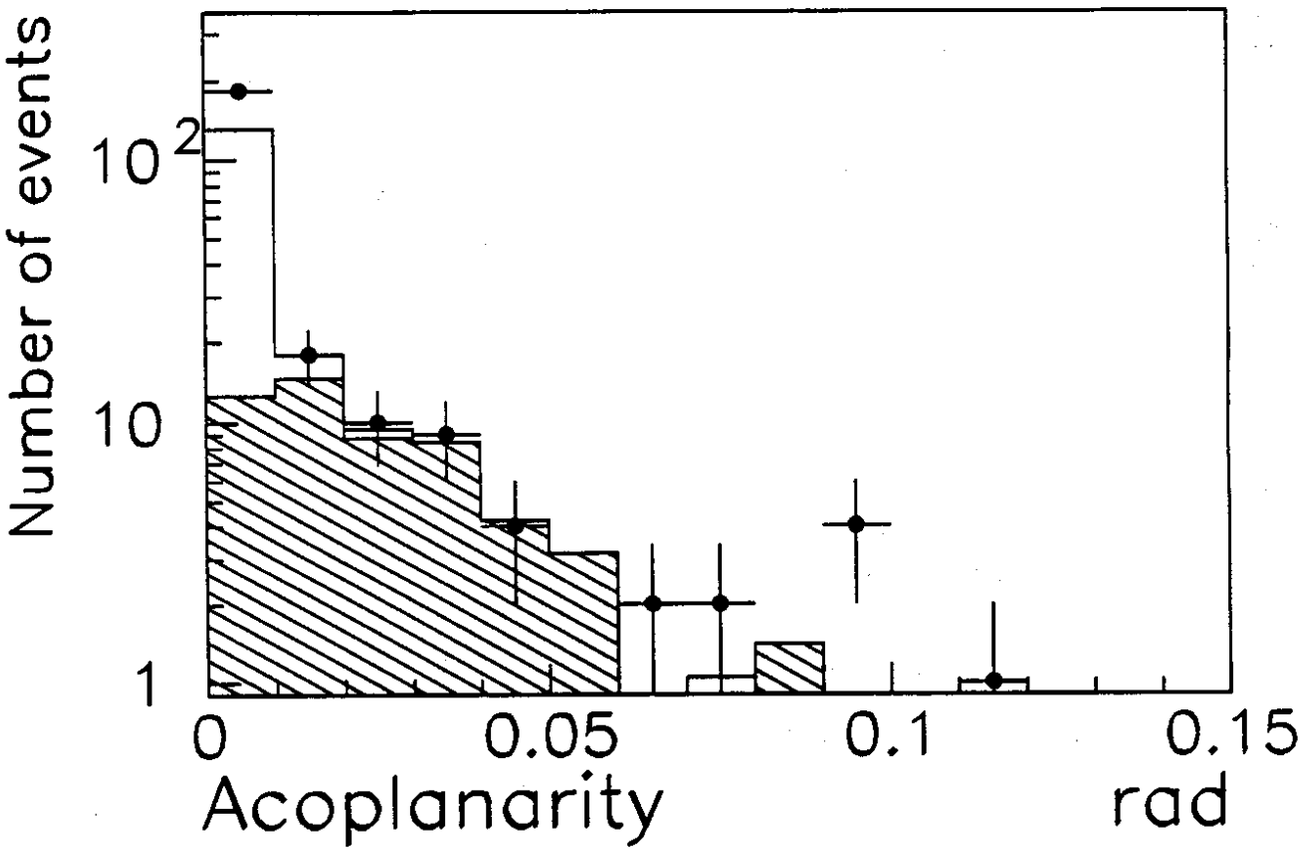

Figure 14 a, b

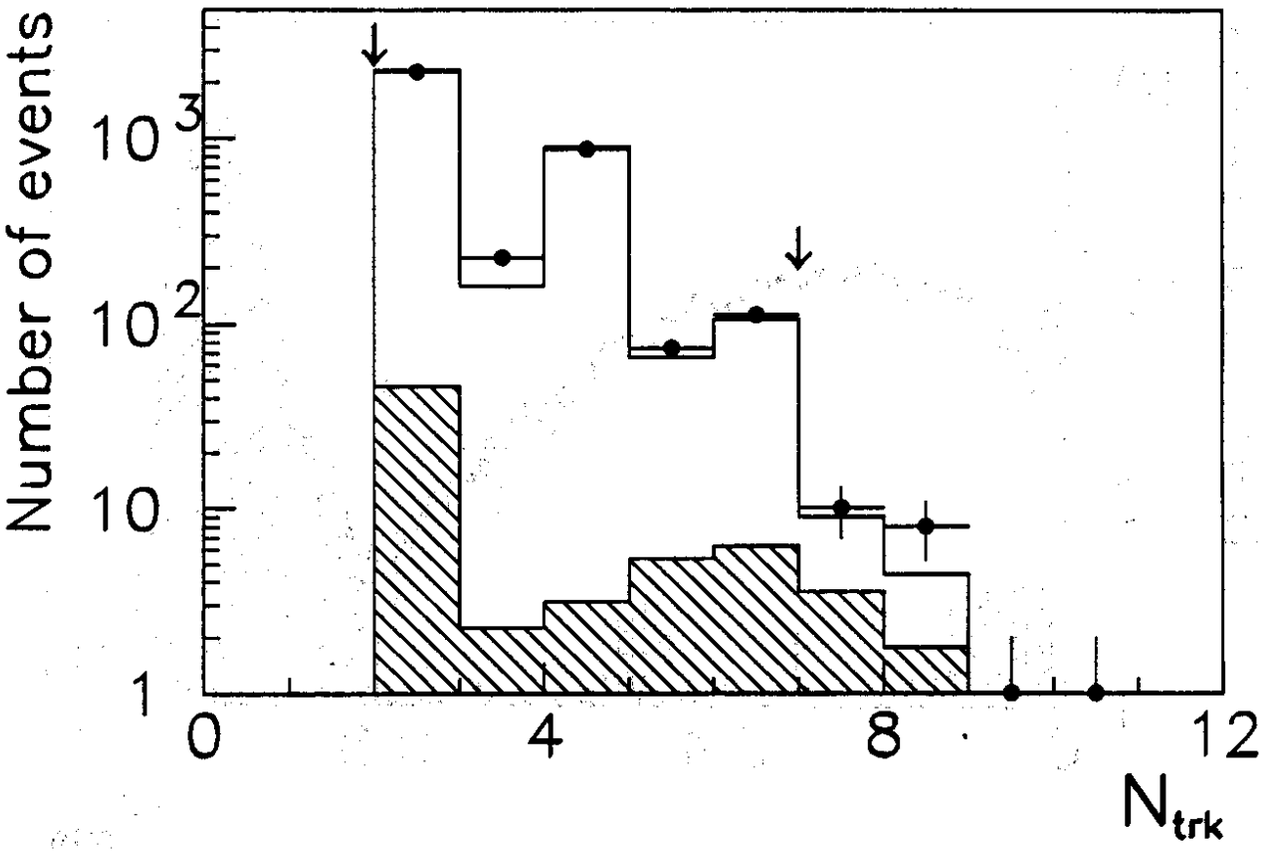
Number of events
10 3
10 2
10
1
0
4
8
12
N trk

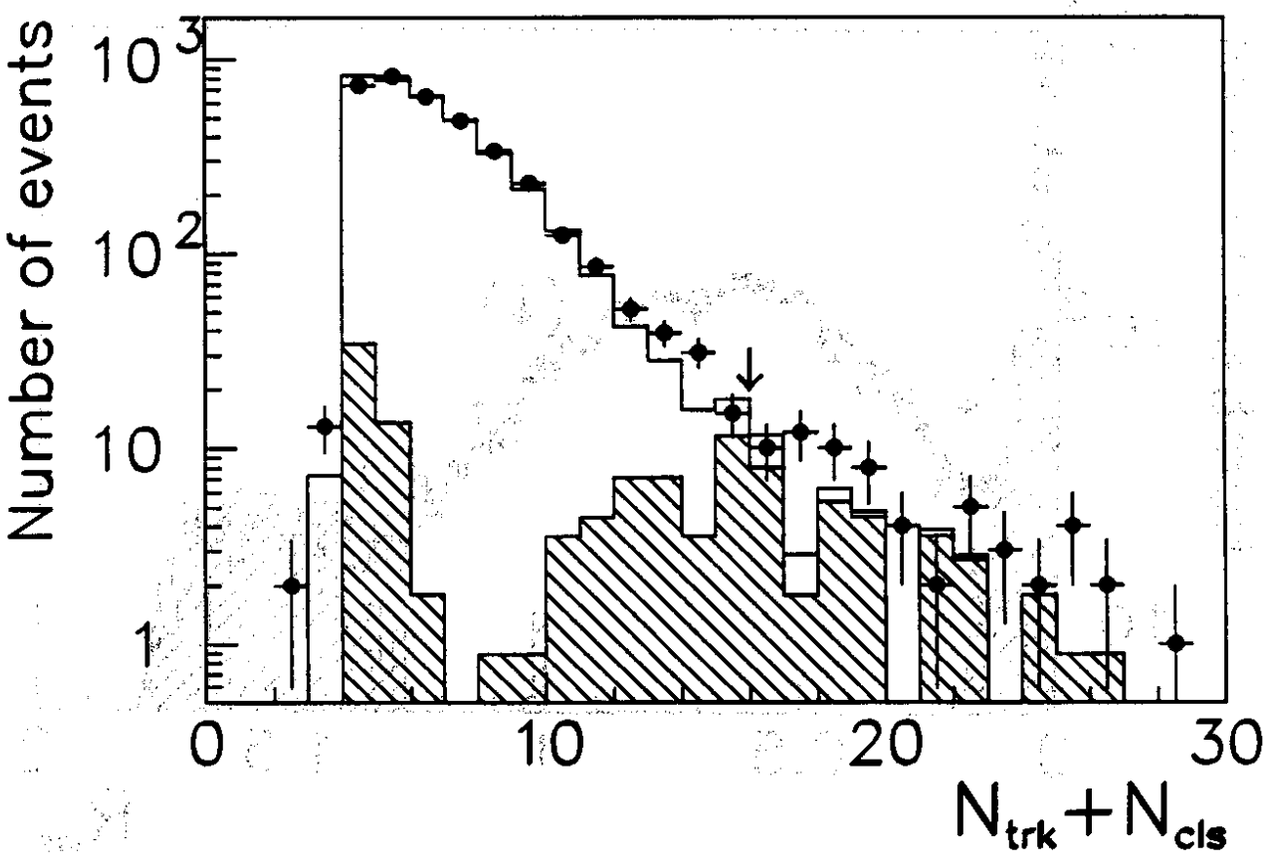
Number of events
10 3
10 2
10
1
0
10
20
30
N trk + N cls

Figure 14 c, d

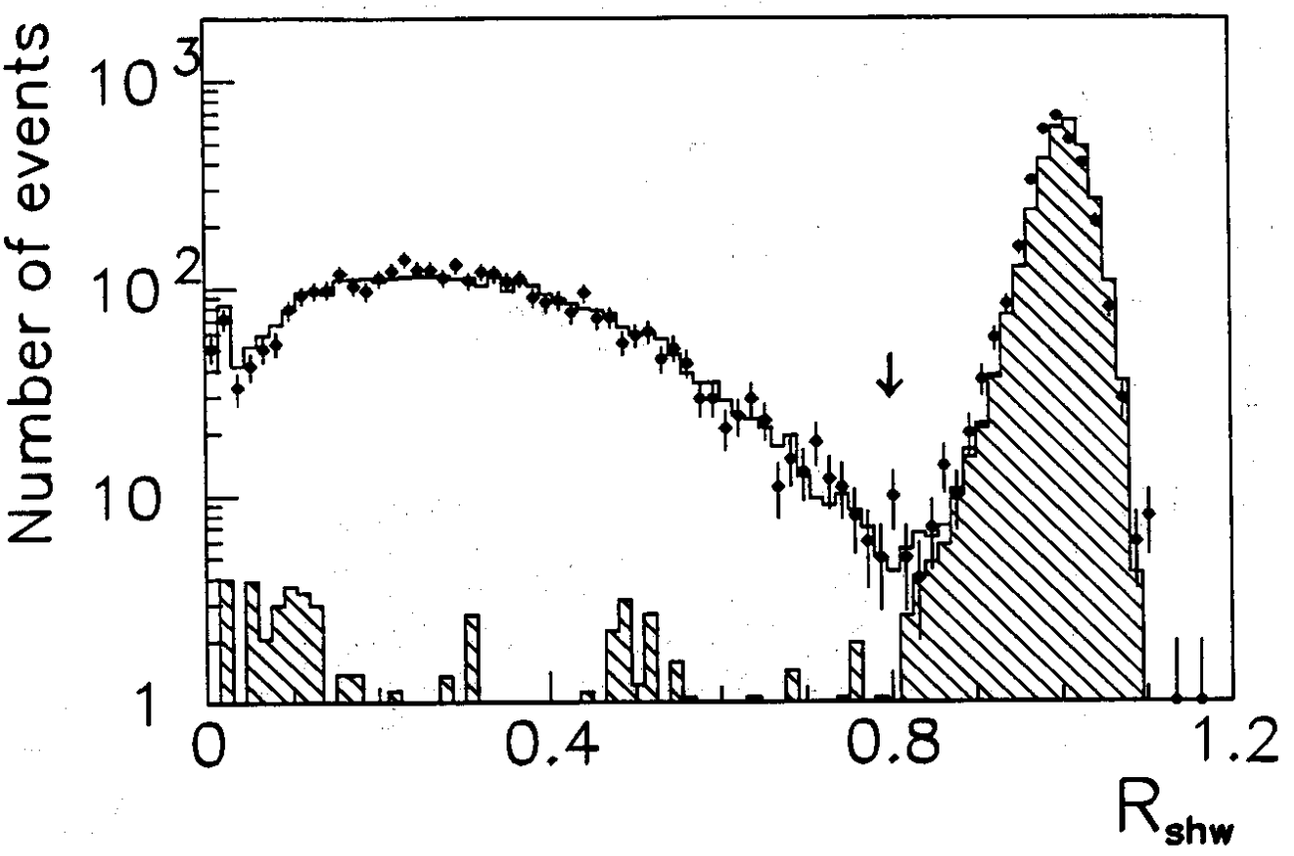
Number of events
10 3
10 2
10
1
0
0.4
0.8
1.2
R shw

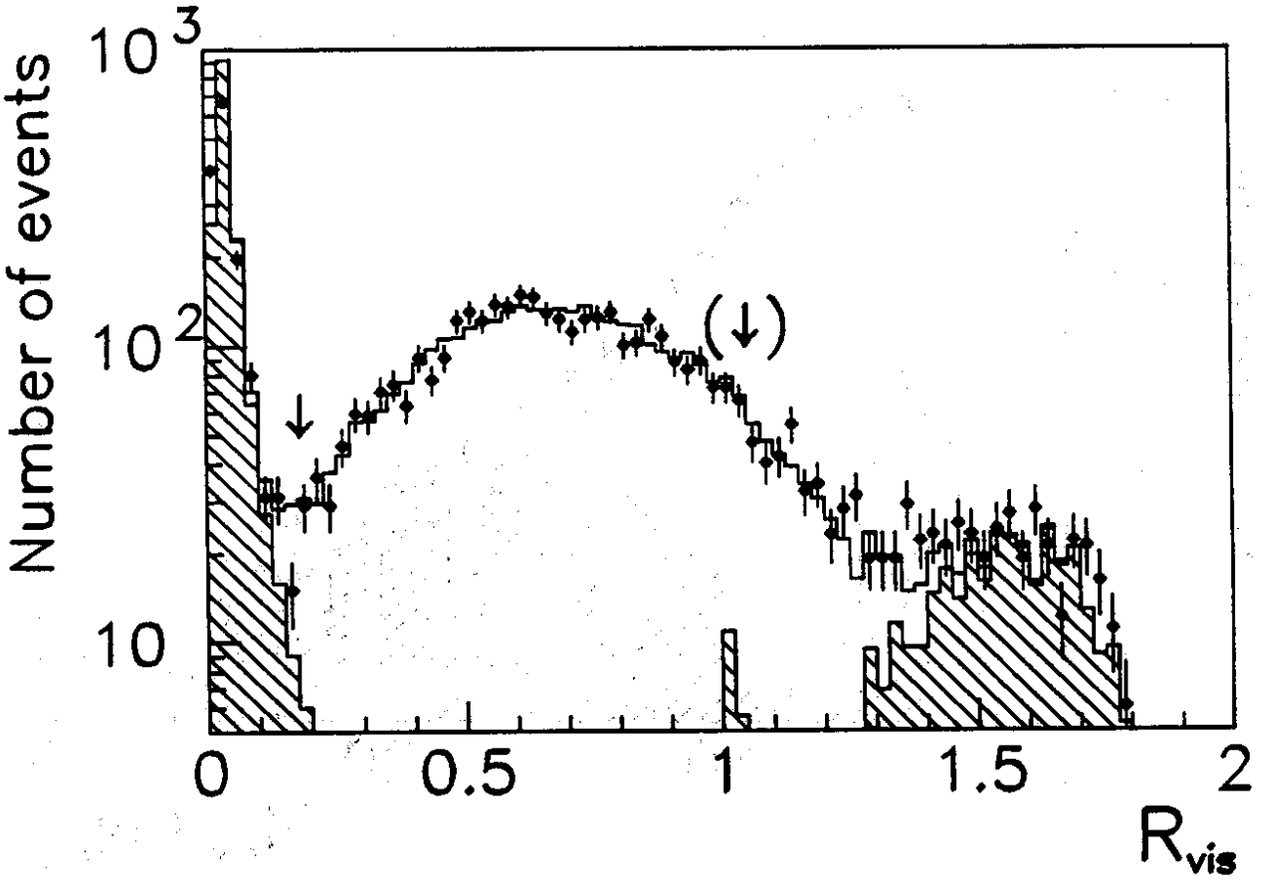
Number of events
10 3
10 2
10
(↓)
0
0.5
1
1.5
2
R vis

Figure 14 e, f

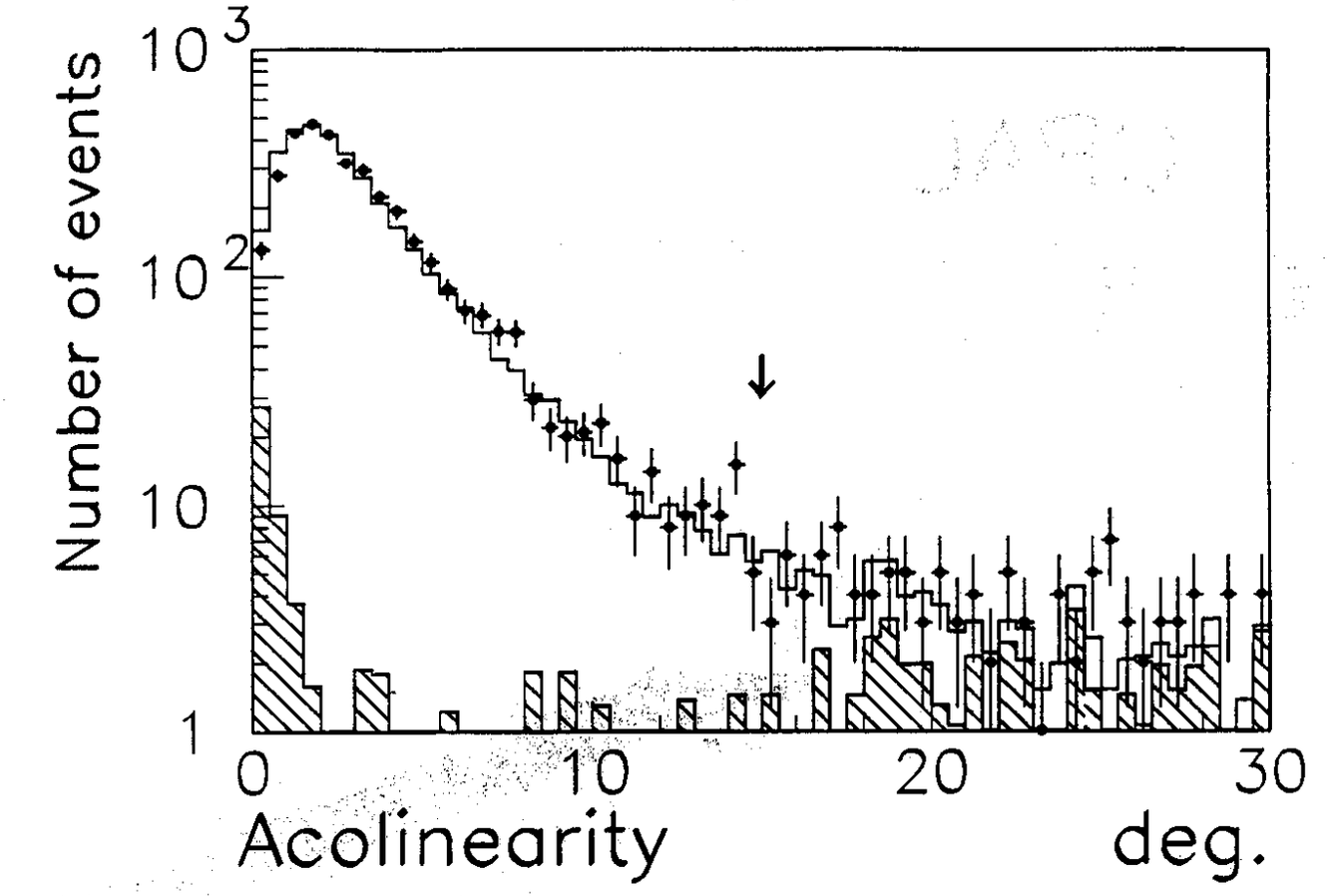
Number of events
10 3
10 2
10
1
0
10
20
30
Acolinearity
deg.

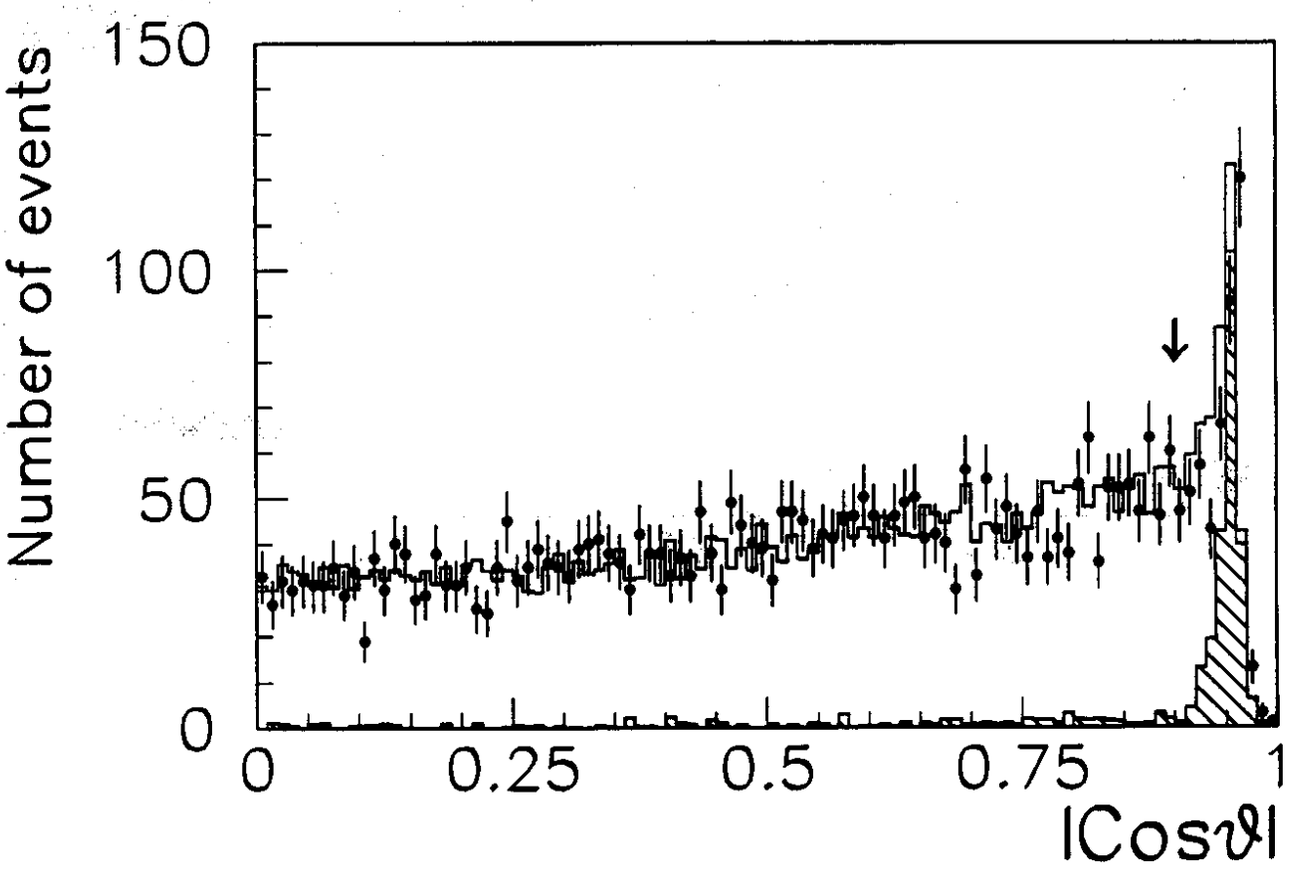
Number of events
150
100
50
0
0
0.25
0.5
0.75
1
|Cosϑ|

Figure 15

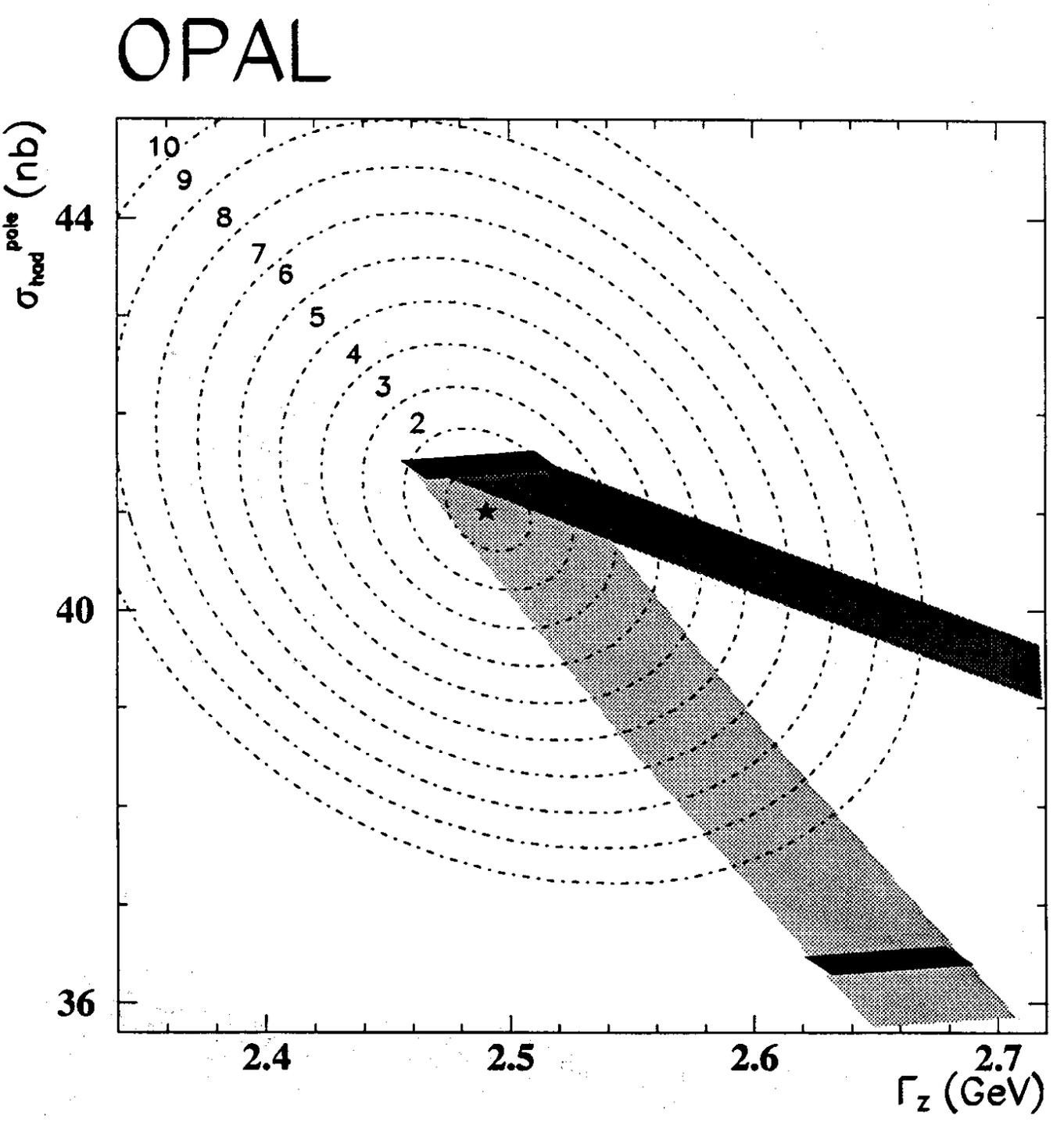
OPAL
σ_{had}^{pole} (nb)
44
40
36
10
9
8
7
6
5
4
3
2
2.4
2.5
2.6
2.7
Γ_Z (GeV)

Figure 16

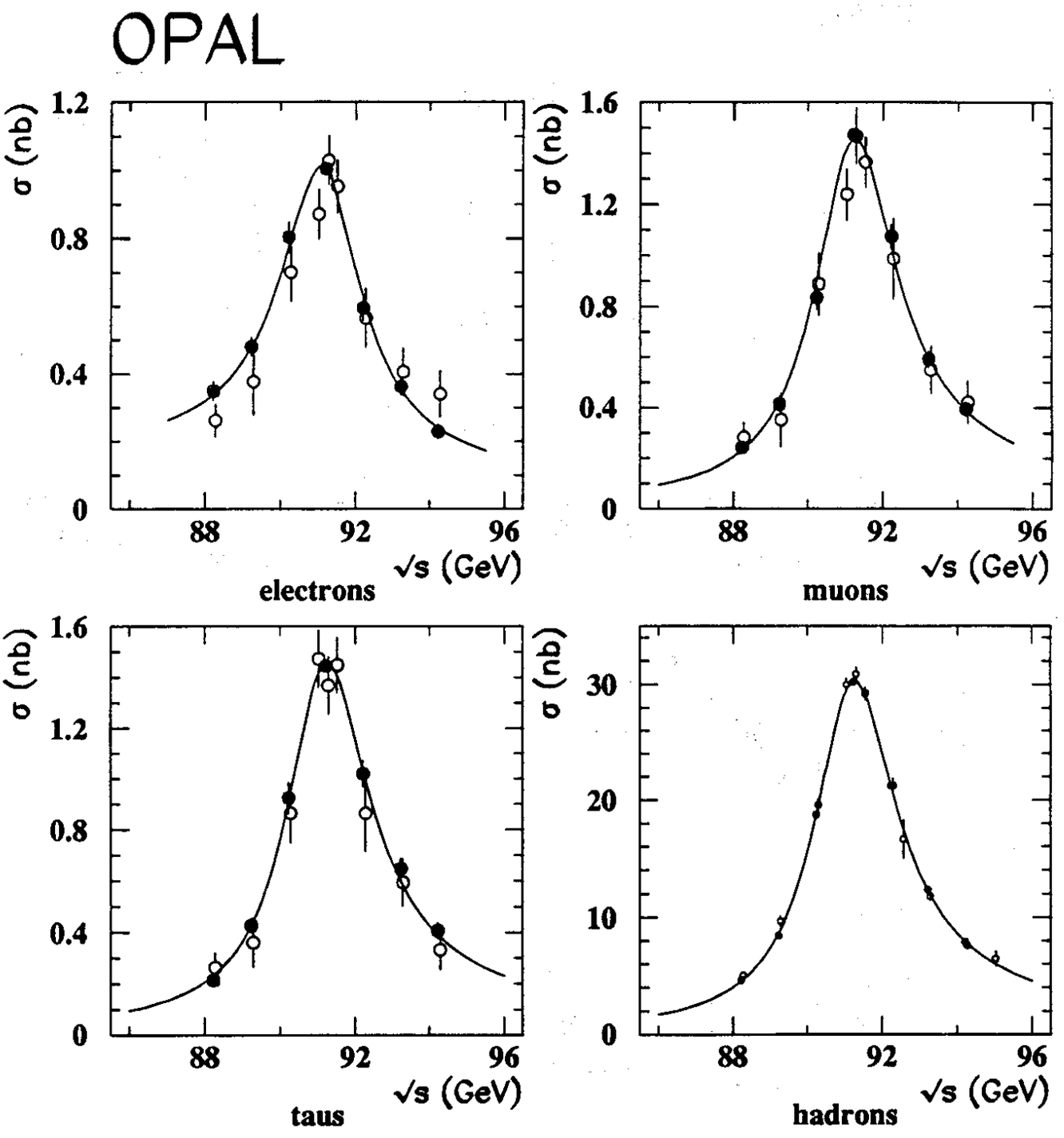
OPAL
σ (nb)
1.2
0.8
0.4
0
88
92
96
√s (GeV)
electrons
σ (nb)
1.6
1.2
0.8
0.4
0
88
92
96
√s (GeV)
muons
σ (nb)
1.6
1.2
0.8
0.4
0
88
92
96
√s (GeV)
taus
σ (nb)
30
20
10
0
88
92
96
√s (GeV)
hadrons

Figure 17

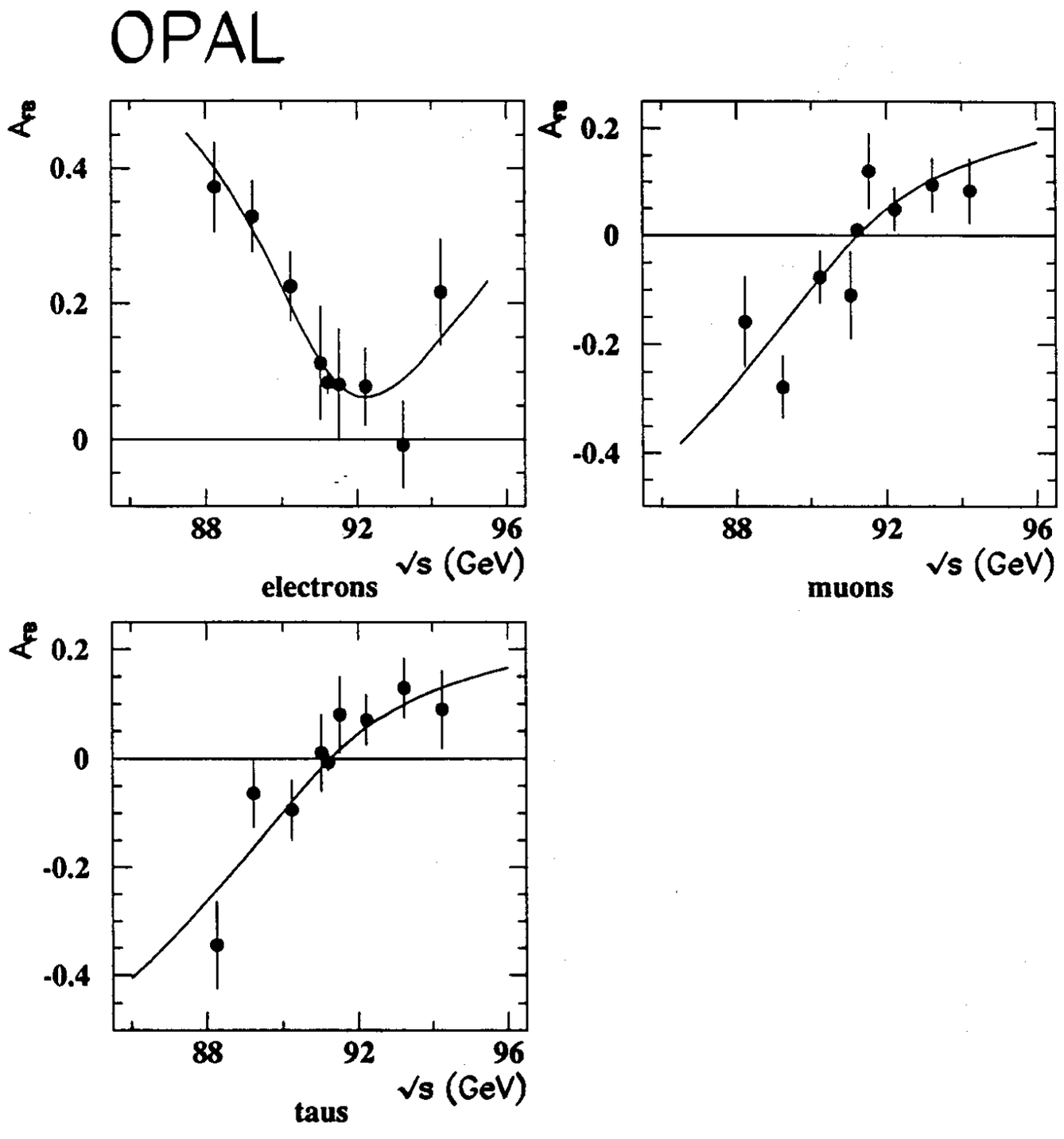
OPAL
A_{FB}
0.4
0.2
0
88
92
96
√s (GeV)
electrons
A_{FB}
0.2
0
-0.2
-0.4
88
92
96
√s (GeV)
muons
A_{FB}
0.2
0
-0.2
-0.4
88
92
96
√s (GeV)
taus

Figure 18 a

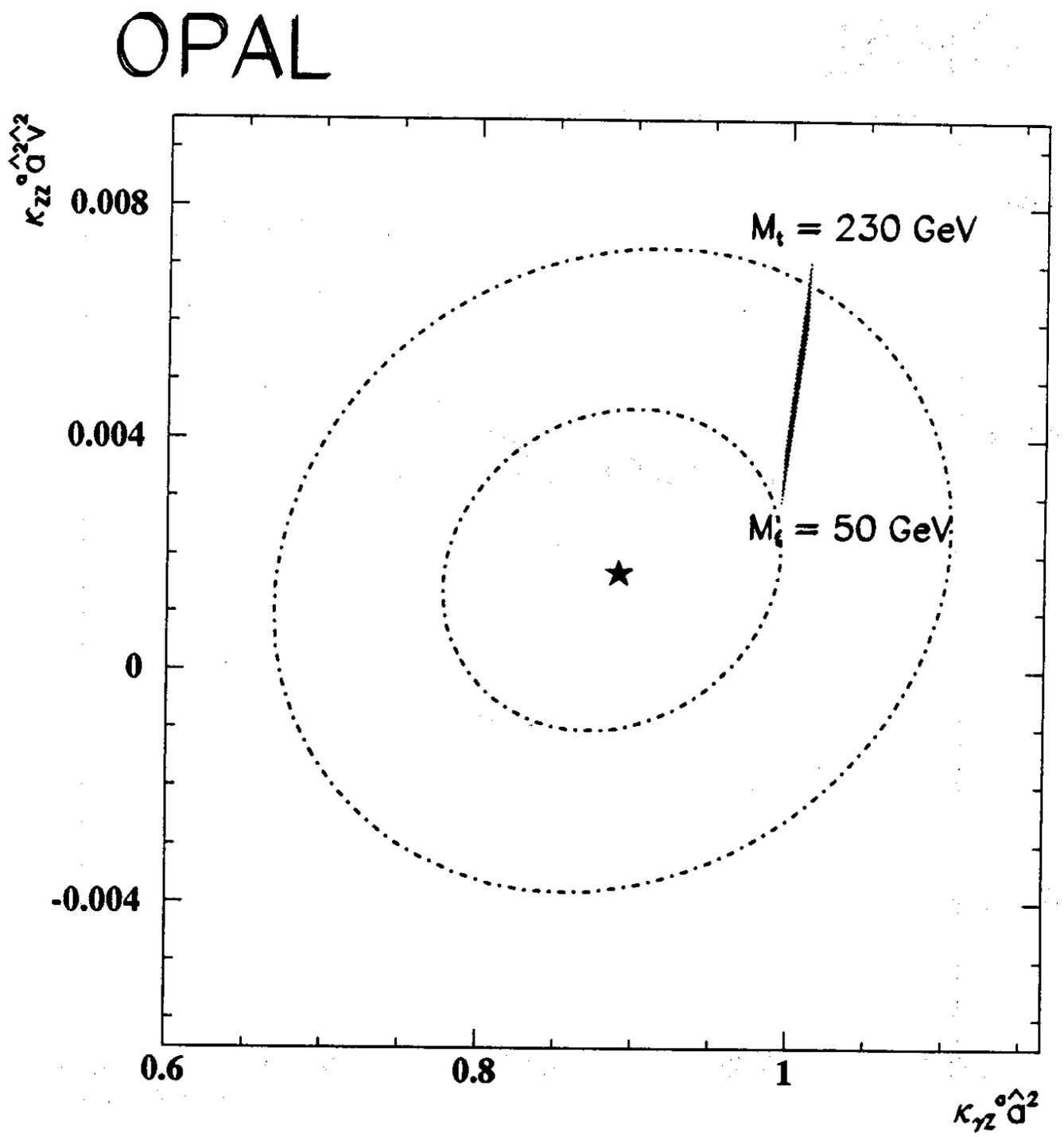
OPAL
$\kappa_{ZZ}\hat{\alpha}^2\hat{V}^2$
0.008
0.004
0
-0.004
M_t = 230 GeV
M_t = 50 GeV
0.6
0.8
1
$\kappa_{\gamma Z}\hat{\alpha}^2$

Figure 18 b

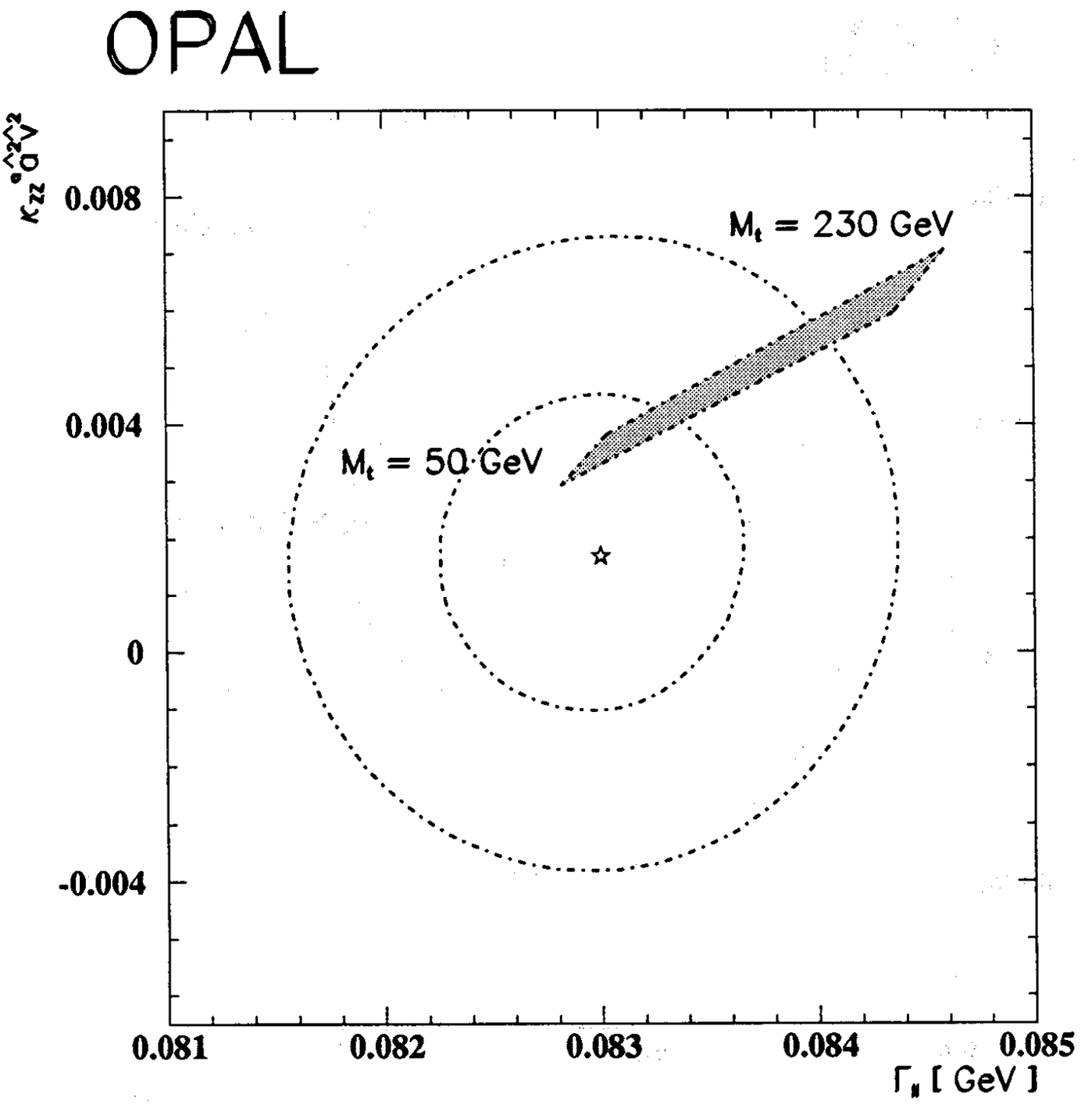
OPAL
$\kappa_{ZZ} \cdot \hat{Q}^2 \hat{V}^2$
0.008
0.004
0
-0.004
M_t = 230 GeV
M_t = 50 GeV
0.081
0.082
0.083
0.084
0.085
Γ_W [GeV]

Figure 18 c

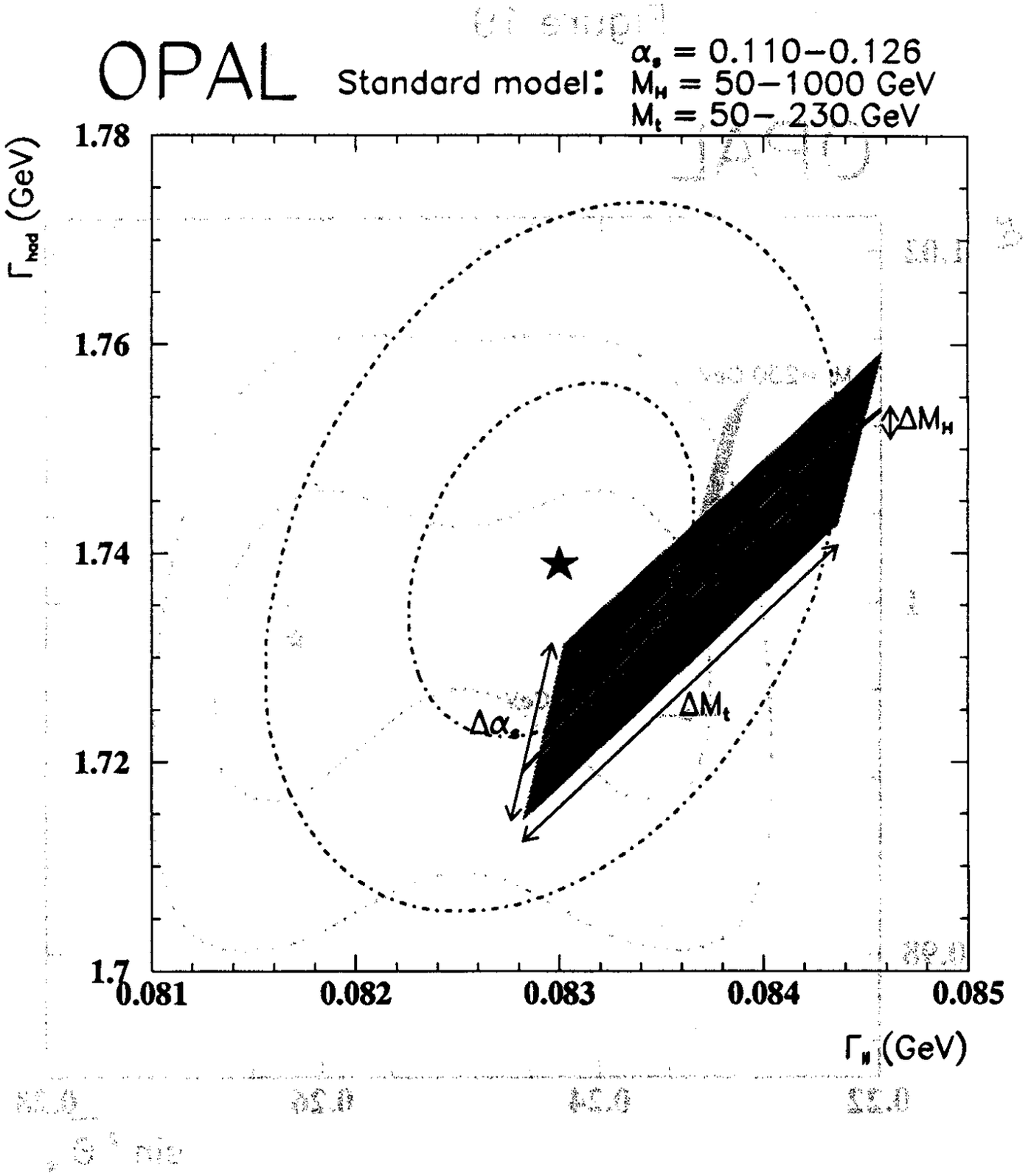
OPAL
Standard model:
α_s = 0.110–0.126
M_H = 50–1000 GeV
M_t = 50– 230 GeV
Γ_{had} (GeV)
1.78
1.76
1.74
1.72
1.7
0.081
0.082
0.083
0.084
0.085
Γ_{ll} (GeV)
ΔM_H
ΔM_t
$\Delta\alpha_s$

Figure 19

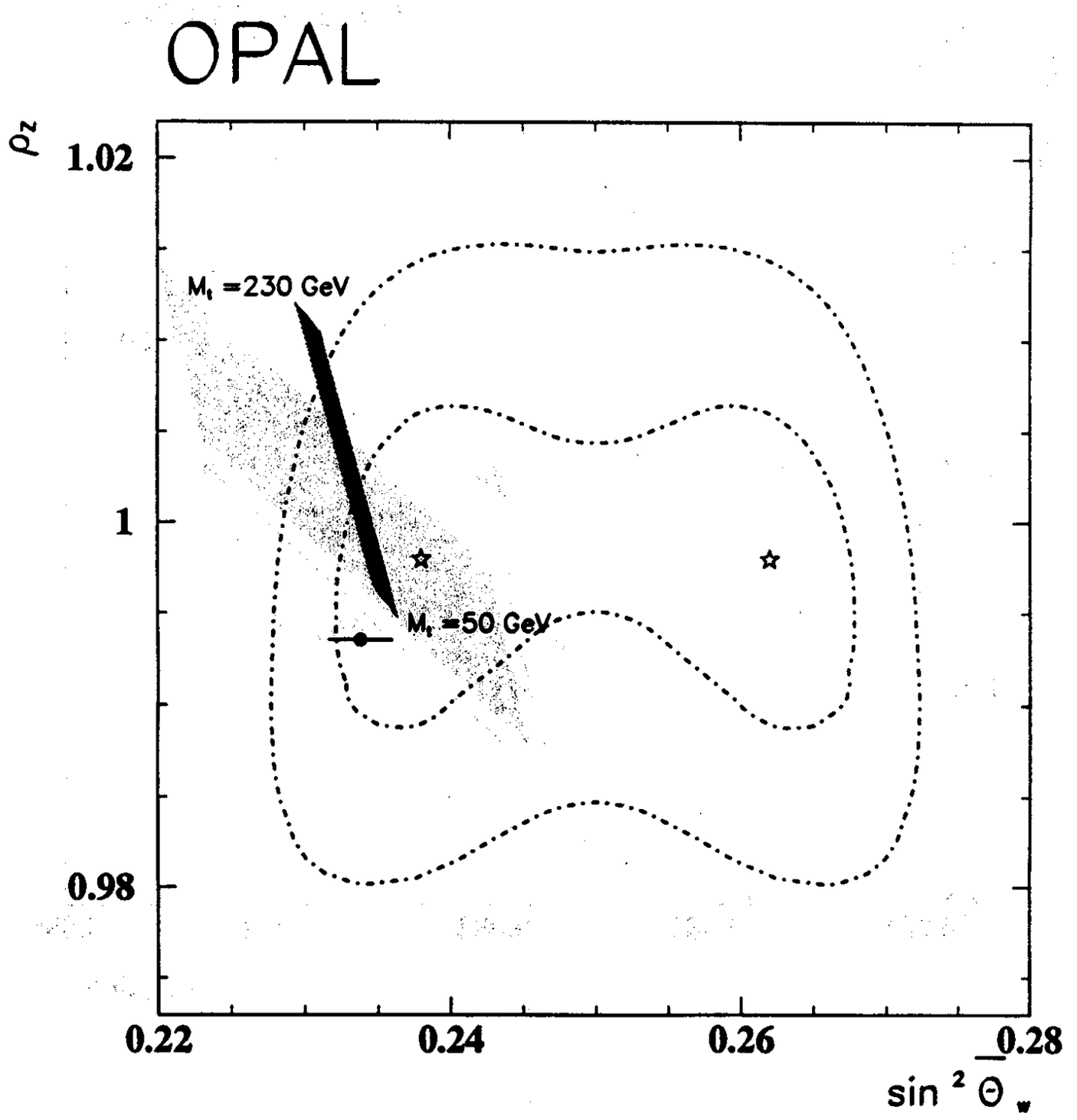
OPAL
ρ_z
1.02
1
0.98
M_t =230 GeV
M_t =50 GeV
0.22
0.24
0.26
0.28
$\sin^2\Theta_w$

Figure 20

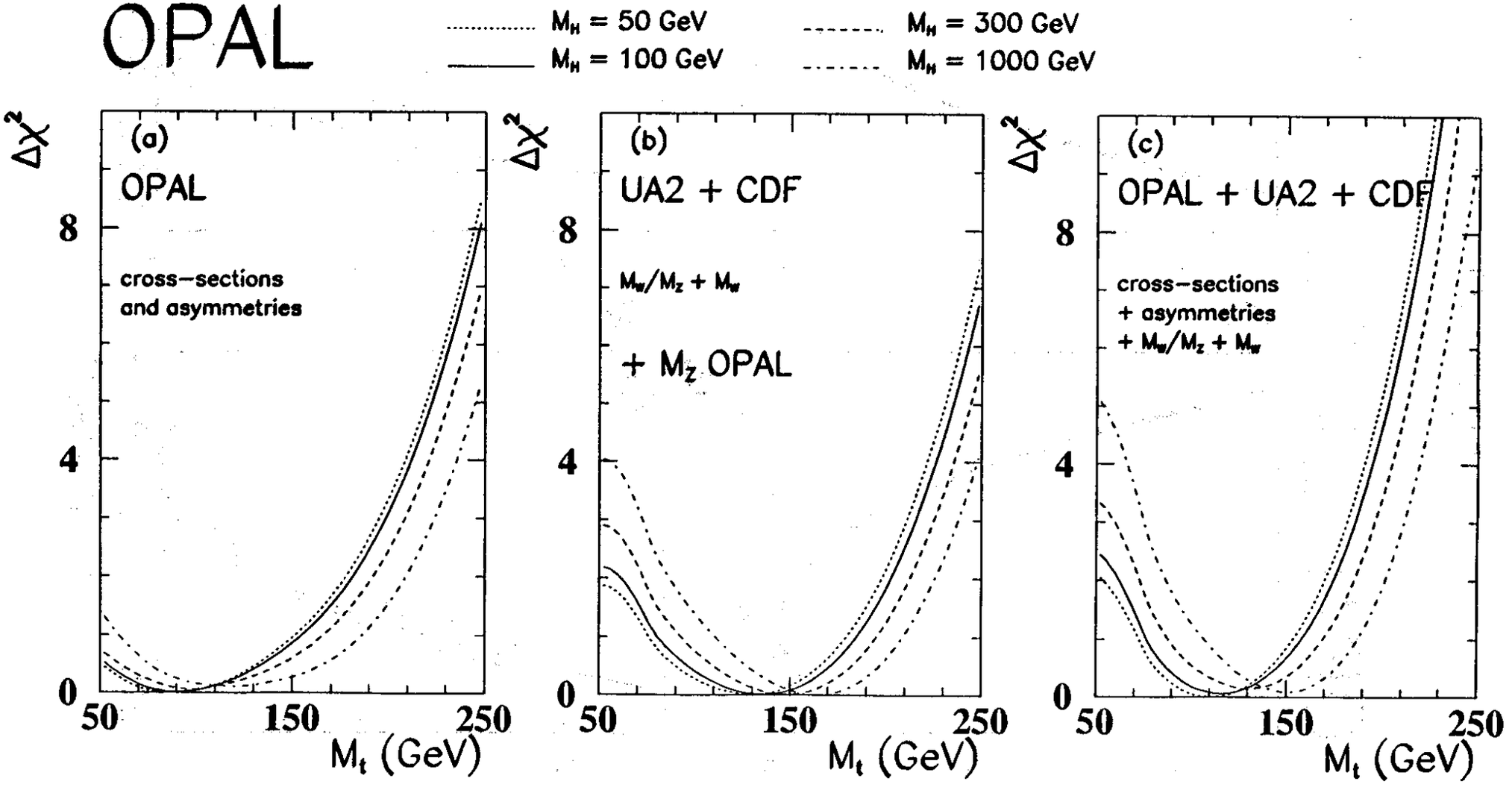
OPAL
M_H = 50 GeV
M_H = 100 GeV
M_H = 300 GeV
M_H = 1000 GeV
(a)
OPAL
cross–sections
and asymmetries
(b)
UA2 + CDF
M_W/M_Z + M_W
+ M_Z OPAL
(c)
OPAL + UA2 + CDF
cross–sections
+ asymmetries
+ M_W/M_Z + M_W
$\Delta\chi^2$
0
4
8
50
150
250
M_t (GeV)

Figure 21

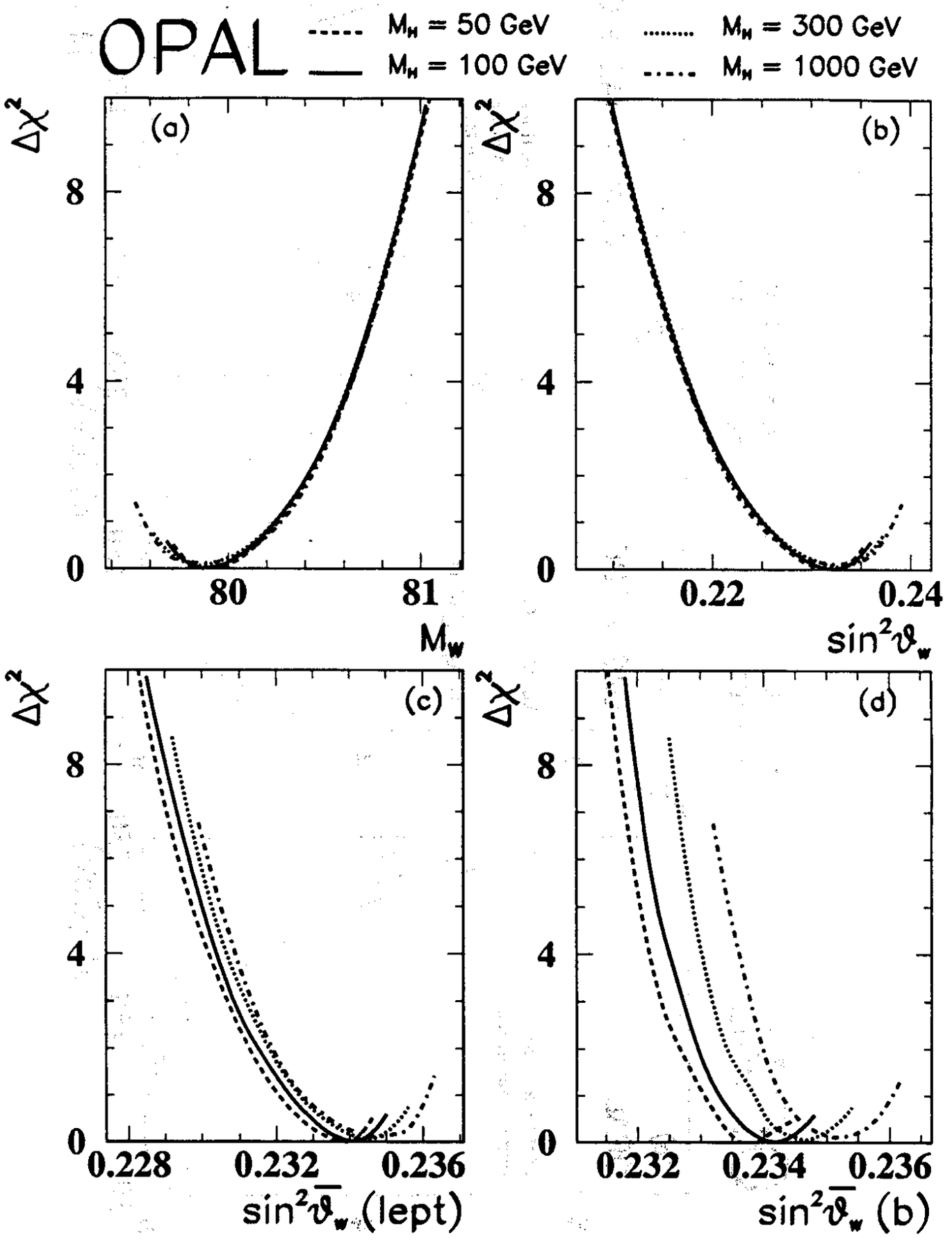
OPAL
M_H = 50 GeV
M_H = 100 GeV
M_H = 300 GeV
M_H = 1000 GeV
(a)
(b)
(c)
(d)
$\Delta\chi^2$
M_W
$\sin^2\vartheta_w$
$\sin^2\bar{\vartheta}_w$ (lept)
$\sin^2\bar{\vartheta}_w$ (b)
0
4
8
80
81
0.22
0.24
0.228
0.232
0.236
0.234

Figure 22

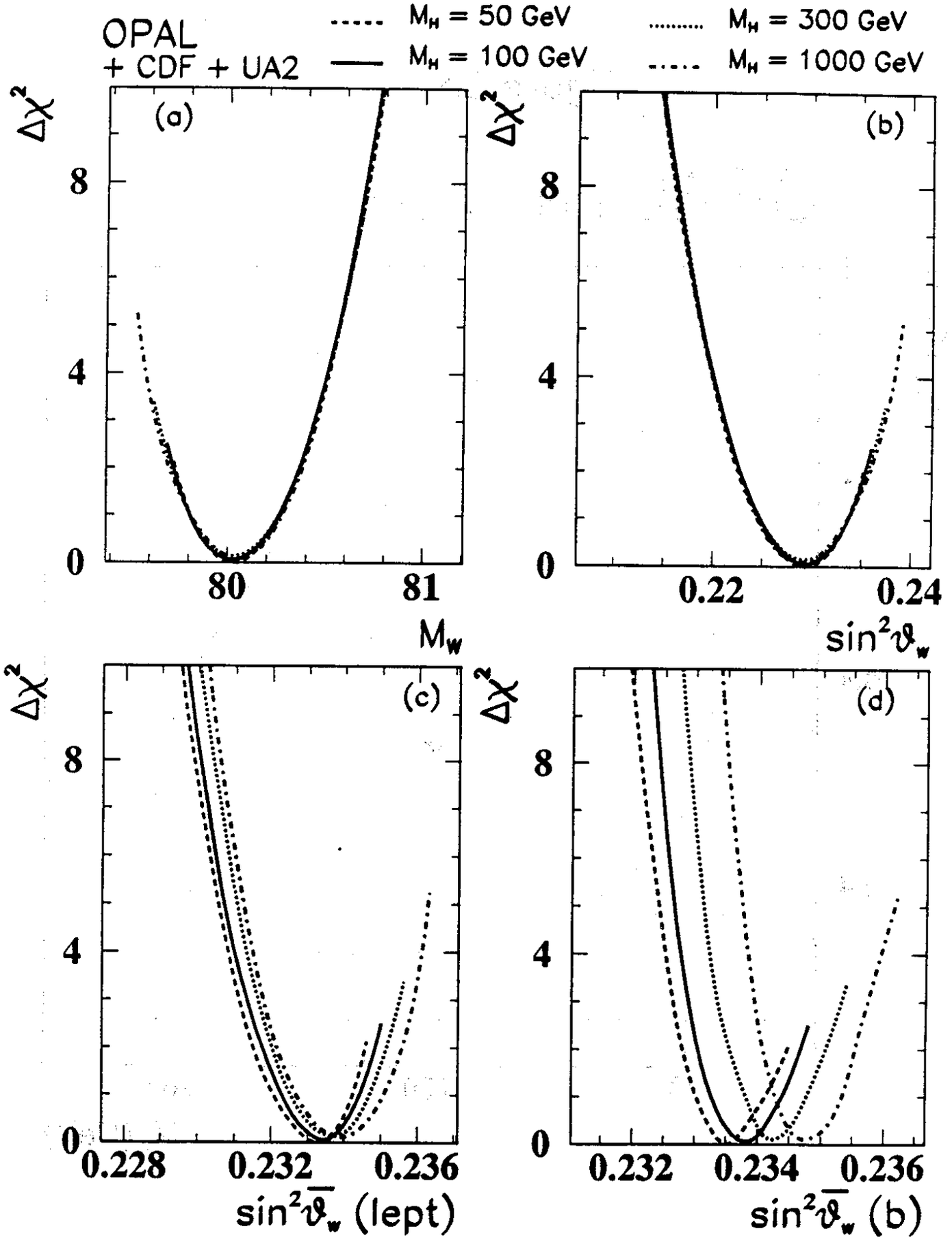
OPAL
+ CDF + UA2
M_H = 50 GeV
M_H = 100 GeV
M_H = 300 GeV
M_H = 1000 GeV
(a)
(b)
(c)
(d)
$\Delta\chi^2$
M_W
$\sin^2\vartheta_w$
$\sin^2\bar{\vartheta}_w$ (lept)
$\sin^2\bar{\vartheta}_w$ (b)
0
4
8
80
81
0.22
0.24
0.228
0.232
0.236
0.234

Figure 23

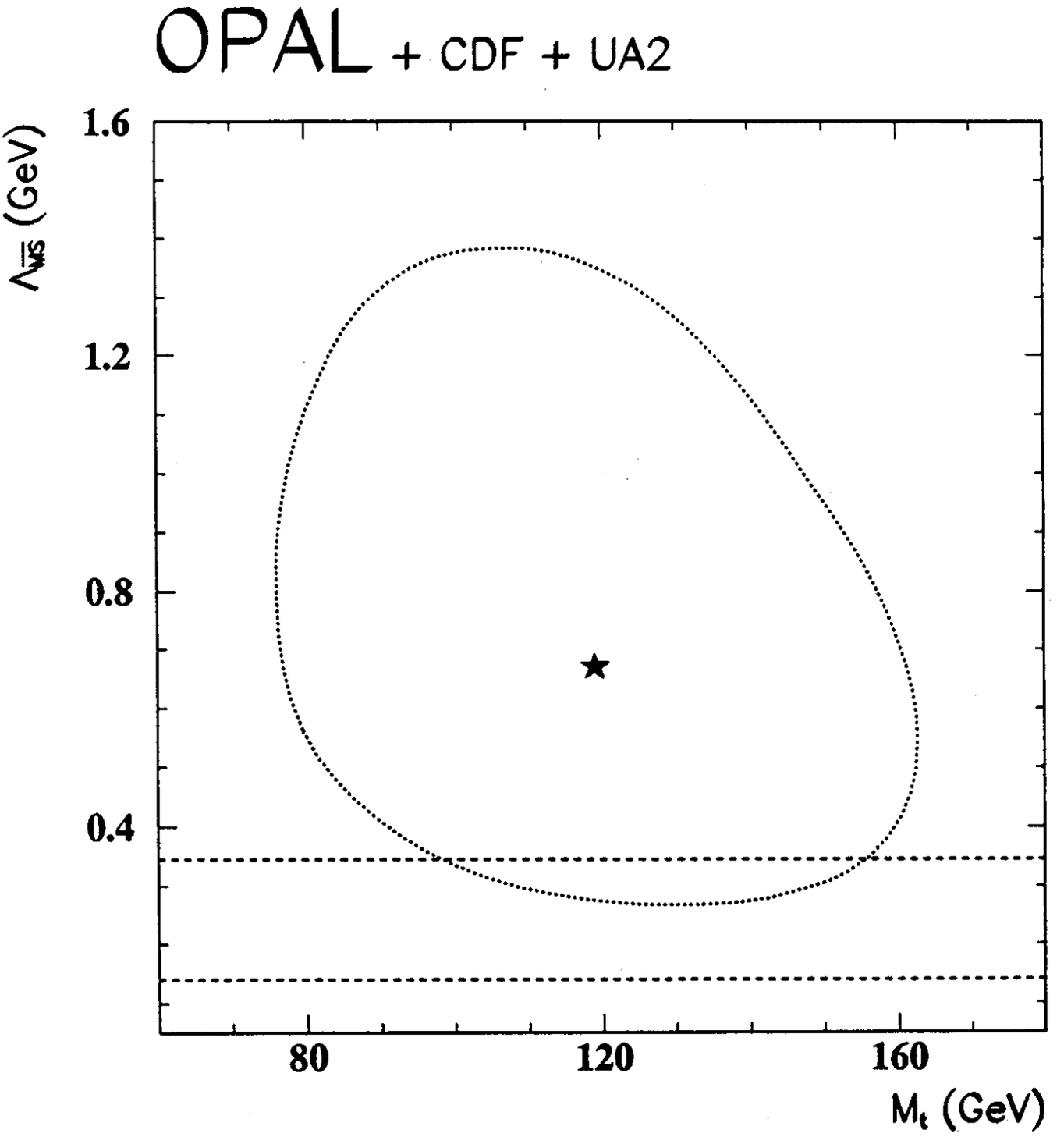

Imprimé au CERN. Prix : 2.60 Fr.